



UNIVERSITAT DE
BARCELONA

Interactions of electrons with matter

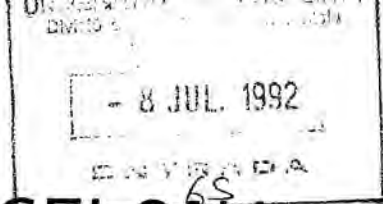
José María Fernández Varea



Aquesta tesi doctoral està subjecta a la llicència **Reconeixement- NoComercial – SenseObraDerivada 4.0. Espanya de Creative Commons.**

Esta tesis doctoral está sujeta a la licencia **Reconocimiento - NoComercial – SinObraDerivada 4.0. España de Creative Commons.**

This doctoral thesis is licensed under the **Creative Commons Attribution-NonCommercial-NoDerivs 4.0. Spain License.**



UNIVERSIDAD DE BARCELONA

Facultad de Física

Interactions of Electrons with Matter

Memoria presentada en la Facultad de
Física de la Universidad de Barcelona por

José María Fernández Varea

para optar al grado de Doctor en Física.

Barcelona, Julio de 1992



FRANCESC SALVAT GAVALDA, Professor titular de Física Atòmica i Nuclear de la Universitat de Barcelona,

FA CONSTAR que el present treball, "INTERACTIONS OF ELECTRONS WITH MATTER", dipositat per en José María Fernández Varea, llicenciat en Ciències Físiques per la Universitat de Barcelona, ha estat realitzat sota la meua direcció, en el Departament d'Estructura i Constituents de la Matèria de la Facultat de Física de la Universitat de Barcelona i que constitueix la seva Tesi per a optar al títol de Doctor en Ciències Físiques.

I, per a que consti, d'acord amb la legislació vigent, firma aquest certificat a Barcelona, a 7 de Juliol de 1992.

Francesc Salvat Gavaldà

Contents

Preface	v
1 Elastic scattering	1
1.1 Introduction	1
1.2 Partial wave cross sections	2
1.2.1 Partial Wave Analysis	3
1.2.2 Numerical phase shifts	4
1.2.3 WKB phase shifts	6
1.2.4 Born phase shifts	6
1.2.5 Simplified calculation method	9
1.3 Screened Mott cross section	15
1.4 Improved high-energy formulas	17
1.4.1 Nuclear size effects	22
1.5 Concluding remarks	24
2 Multiple scattering	27
2.1 Introduction	27
2.2 Multiple scattering theories	30
2.2.1 Single scattering differential cross sections	31
2.2.2 The theories of Goudsmit and Saunderson and Lewis	34
2.2.3 The Wentzel model	38

2.2.4	The Molière theory	42
2.3	A new simulation algorithm	52
2.4	Simulating with a Wentzel model	60
2.5	Conclusions	66
3	Optical-data models	67
3.1	Introduction	67
3.2	Born approximation	69
3.3	Free-electron gas	72
3.4	Optical oscillator strength	75
3.4.1	The Local Plasma Approximation	77
3.5	Optical-data models	80
3.5.1	The statistical model	80
3.5.2	Ashley's model	80
3.5.3	Penn's model	81
3.5.4	Shell model	81
3.5.5	A comparison of optical-data models	81
3.6	A new optical-data model	85
3.6.1	Exchange correction	85
3.6.2	One-electron cross sections	87
3.6.3	Analytical formulas for λ and S	88
3.7	Calculation results	89
3.8	Conclusions	97
4	Energy loss of fast electrons	99
4.1	Introduction	99
4.2	Collision losses	101
4.2.1	Schematic Bethe surface	102

4.2.2	Density effect	106
4.3	Radiative losses	115
4.3.1	Bethe-Heitler DCS	115
4.4	Random sampling algorithms	127
4.4.1	Energy loss in electron hard collisions	127
4.4.2	Energy loss in positron hard collisions	129
4.4.3	Energy loss in hard photon bremsstrahlung emission	129
4.5	Soft energy loss events	131
4.6	Conclusions	134
Conclusions		137
A Legendre functions of the second kind		139
B Random sampling of angular reflections in artificial soft collisions		141
C Folding Theorem		143
D Useful kinematic relations		147
References		149

Preface

The interaction of electrons with matter has been a subject of intense work since the beginning of the century. Although we know that the interaction is purely electromagnetic, its theoretical description is complicated by two different reasons. On the one hand, the number of particles that participate in the interaction may be very large. Even when the target is a single hydrogen atom, the collision is a three body problem for which only approximate solutions of the wave equation are known. Therefore, the interaction can only be treated by using approximate many body methods. In particular, scattering of fast electrons by single atoms can be reasonably understood on the basis of independent particle models. On the other hand, when the medium where the projectile moves extends over a large volume, the projectile may interact repeatedly with the medium. As a consequence, the proper tools to deal with problems involving electron penetration in matter are multiple scattering theories and/or Monte Carlo simulation.

The gross features of the interaction of electrons with kinetic energies above a few hundred eV with single atoms are quite well understood and can be described by using standard methods. The static field approximation, i.e. partial wave calculations with a scattering field determined from the atomic electron density, gives an accurate description of elastic scattering. This kind of calculations, however, demands a considerable amount of numerical work that increases with the kinetic energy of the projectile. Partial wave differential cross sections have been published only for kinetic energies up to some 500 keV. Inelastic scattering can be described by using the plane-wave Born approximation suitably corrected for exchange effects. Apart from kinematical factors, the Born differential cross section is proportional to the generalized oscillator strength. This quantity is known in analytical form for the hydrogen atom, but it is difficult to compute for more complex atoms. The scattering of electrons by molecules can be analyzed with similar, but more involved, methods.

The interaction of electrons with solids, and other extended media, is far more complicated. First, the periodicity of the solid distorts the outer orbitals of the atoms, an effect which can only be approximately quantified through involved band-structure calculations. Second, the low-energy part of the excitation spectrum is strongly influenced by the structure of the solid in such a complicate way that a theoretical description of electron inelastic scattering from first principles is practically unfeasible. Finally, multiple scattering effects can only be accounted for by solving the Boltzmann transport equation, or by means of Monte Carlo simulation. Detailed Monte Carlo simulation yields to the exact solution of the transport equation (except for statistical uncertainties that are inherent of the this method) for arbitrary geometries. However, detailed simulation is only feasible for electrons with kinetic energies less than ~ 100 keV. For higher energies condensed simulation methods based on approximate multiple scattering theories must be used. The condensed simulation codes presently available incorporate multiple scattering theories which are only roughly approximate and, in many situations, do not allow the simulation of actual experiments with enough detail and accuracy.

The aim of this thesis is to provide a consistent basis for the development of Monte Carlo simulation algorithms more accurate than the ones presently available. Actually, a high-energy simulation code based on relevant parts of this thesis is already operable; and a program to simulate electron transport at intermediate and low energies (say below 100 keV) is currently being developed from the theory presented in this work. The reliability of the simulation results obtained with these codes will offer the ultimate demonstration of the correctness and effectiveness of the approaches described here.

The thesis is structured in four chapters. In each chapter we concentrate on a particular aspect of the electron-matter interaction. Owing to the distinct nature of the considered topics, we have tried to make each chapter self-contained. In particular we have used notations according to the standard literature in each field.

Chapter 1 is devoted to the evaluation of reliable single elastic scattering cross sections for high energies. A numerical method which allows the calculation of partial wave cross sections for projectiles with kinetic energies up to ~ 20 MeV is briefly described. Extensive calculations with this method have been performed and the results are used to set up a new semi-analytical formula which yields reliable cross sections for electrons and positrons with kinetic energy larger than about Z keV.

Multiple elastic scattering is considered in detail in chapter 2. We offer a simple derivation of the popular theory of Molière which puts into evidence its physical content and limitations. A new simulation algorithm, which is valid for any single scattering model and is free from the main limitations of the currently used algorithms, is described. Finally, this algorithm is combined with a simple analytical cross section to produce a new simulation method which gives 1) angular distributions as accurate as those obtained from the theory of Molière, and 2) spatial distributions practically identical to those that would be obtained from the exact solution of the transport equation.

Chapter 3 is devoted to the inelastic scattering of low-energy electrons in solids. Our treatment is based on the Born-Ochkur approximation, which is well known in atomic collision theory. The main difficulty here is to determine the generalized oscillator strength of the solid. We adopt a generalized oscillator strength model based on experimental optical data which correctly reproduces the excitation spectrum of the solid.

In chapter 4 we consider the energy loss of high-energy electrons and positrons in matter. Inelastic interactions are described by using the Born approximation on the basis of a simple generalized oscillator strength model. Our approach also accounts for the so-called shell corrections and Sternheimer's density effect correction. Bremsstrahlung emission is described by a modified Bethe-Heitler formula which includes screening effects, the Coulomb correction and a low-energy correction. From the resulting differential cross sections, the random sampling of the energy loss and the scattering angle in each inelastic or radiative event can be performed analytically.

Chapter 1

Elastic scattering

1.1 Introduction

Monte Carlo simulation of high-energy electron and positron transport needs reliable transport cross sections for elastic scattering that, preferably, should be obtainable from a numerically simple and computationally fast algorithm. Although much work has been devoted to the problem of elastic scattering by single atoms, such a general algorithm remains to be found [SB82].

The evaluation of accurate elastic differential cross sections (DCS) and transport cross sections requires exact phase shift calculations for the solution of the Dirac equation for the electron or positron in the screened nuclear field [RM75,RL84,Sa91]. However, this kind of calculation demands a formidable amount of numerical work when the kinetic energy of the electron exceeds a few hundred keV. The numerical effort to obtain the DCS can be reduced at the expense of using approximate scattering fields that allow the evaluation of the majority of phase shifts by means of methods which demand much less work than the direct solution of the radial Dirac equation. Using this kind of strategy, we have been able to carry out partial wave calculations for energies up to ~ 20 MeV. Although these partial-wave methods yield reliable numerical DCSs, they are still too much complicated to be useful in high-energy Monte Carlo simulations, where calculation simplicity is as important as reliability. It is, therefore, necessary to seek simpler approximate methods to obtain the DCS for energies larger than a few hundred keV.

In this chapter, we present a conveniently simple numerical method to compute the

elastic scattering data needed for simulating the multiple scattering of electrons and positrons. Our starting point is the exact Mott DCS for an unscreened point nucleus [MM65,DS56,Sh56,VP74] which, for high enough energies, reproduces the large-angle behaviour of the actual DCS. Screening effects are introduced by means of the Born approximation, i.e. through a screening factor $[1 - F_e(q)]^2$, where $F_e(q)$ is the atomic form factor [MM65]. To improve the accuracy of this “screened Mott” DCS we introduce an empirical correction which modifies it at small angles so as to reproduce the first transport cross section obtained from partial wave calculations. Finally, nuclear size effects, which influence the multiple scattering distributions of electrons and positrons with kinetic energies larger than ~ 10 MeV, are introduced through the Born approximation assuming a simple nuclear charge distribution [He56]. The DCS so obtained is accurate except for very small scattering angles, which have no effect on the multiple scattering distributions.

1.2 Partial wave cross sections

The general theory of high-energy electron scattering has been reviewed by Walker [Wa71]. For kinetic energies larger than a few keV, exchange and charge cloud polarization corrections are negligible and the cross section can be computed by using the static field approximation [MM65,Wa71]. In this approximation, the DCS is obtained by solving the partial wave expanded Dirac equation for the motion of the electron or positron in the field of the nucleus screened by the atomic electrons.

In this section we use atomic Hartree units (i.e. the reduced Planck constant \hbar , the electron mass m and the electron charge e are taken as unity) unless otherwise specified. Assuming a point nucleus, the scattering field is given by

$$V(r) = z \left[\frac{Z}{r} - \int \frac{\rho_e(r')}{|r - r'|} d^3r' \right] \equiv \frac{zZ}{r} \phi(r), \quad (1.1)$$

where z (-1 for electrons, $+1$ for positrons) is the charge of the projectile and $\rho_e(r)$ is the density of atomic electrons, which is assumed to be spherically symmetric. The right-hand side of eq. (1.1) defines the screening function $\phi(r)$. The electron density and the screening function are related through Poisson’s equation:

$$\frac{Z}{r} \frac{d^2 \phi(r)}{dr^2} = 4\pi \rho_e(r). \quad (1.2)$$

The most accurate screening functions available to date are those obtained from self-consistent Hartree-Fock computations. These numerical screening functions can be closely approximated by means of the following analytical expression

$$\phi(r) = \sum_{i=1}^3 A_i \exp(-\alpha_i r), \quad \sum A_i = 1. \quad (1.3)$$

This analytical form has been extensively used in the past with parameters determined by fitting different approximate atomic potentials (see e.g. refs. [Mo47,BS63,SM87a]). In the calculations described here we use the expression (1.3) with the parameters obtained by Salvat et al. [SM87a] from a fit of the Dirac-Hartree-Fock-Slater (DHFS) field. This set of parameters was determined so as to exactly reproduce the radial expected values $\langle r^n \rangle$ obtained from the DHFS atomic density for $n = -1$ to 4. This fitting procedure makes sure that the atomic form factors computed from the numerical self-consistent electron density and from the screening function eq. (1.3) coincide for small momentum transfers. As a consequence, the Born DCSs computed from the analytical screening function and from the numerical DHFS field are practically identical (see ref. [SM87a]). Thus, the screened fields considered here are of the form

$$V(r) = \frac{zZ}{r} \sum_{i=1}^3 A_i \exp(-\alpha_i r). \quad (1.4)$$

1.2.1 Partial Wave Analysis

The DCS per unit solid angle for scattering of unpolarized electrons or positrons, $d\sigma/d\Omega$, is given by

$$\frac{d\sigma}{d\Omega} = |f(\theta)|^2 + |g(\theta)|^2, \quad (1.5)$$

where the direct and spin-flip scattering amplitudes $f(\theta)$ and $g(\theta)$ are defined by [Be63,Sh56]

$$f(\theta) = \sum_{\ell=0}^{\infty} F_{\ell} P_{\ell}(\cos \theta), \quad (1.6)$$

$$g(\theta) = \sum_{\ell=0}^{\infty} G_{\ell} P_{\ell}^1(\cos \theta). \quad (1.7)$$

θ is the scattering angle, $P_{\ell}(\cos \theta)$ are the Legendre polynomials and $P_{\ell}^1(\cos \theta)$ are the associated Legendre functions respectively,

$$F_{\ell} = \frac{1}{2ik} \{(\ell + 1) [\exp(2i\delta_{\ell+}) - 1] + \ell [\exp(2i\delta_{\ell-}) - 1]\}, \quad (1.8)$$

$$G_{\ell} = \frac{1}{2ik} \{\exp(2i\delta_{\ell-}) - \exp(2i\delta_{\ell+})\}, \quad (1.9)$$

and $\delta_{\ell-}$, $\delta_{\ell+}$ are the phase shifts. k stands for the momentum of the projectile which is related to its kinetic energy E through

$$k = \frac{(E^2 - c^4)^{1/2}}{c}. \quad (1.10)$$

For each value of the orbital angular momentum ℓ (except $\ell=0$) there are two phase shifts corresponding to the two possible values of the total angular momentum $j = \ell \pm 1/2$. We follow Walker [Wa71] in using the notation $\delta_{\ell a}$, with $a \equiv 2(j - \ell)$, for the phase shifts. These are determined from the solution of the radial Dirac equations [Wa71]

$$\frac{dP_\kappa}{dr} = -\frac{\kappa}{r}P_\kappa - \frac{E - V(r) + 2c^2}{c}Q_\kappa, \quad (1.11)$$

$$\frac{dQ_\kappa}{dr} = \frac{E - V(r)}{c}P_\kappa + \frac{\kappa}{r}Q_\kappa, \quad (1.12)$$

where $\kappa \equiv -a(j + 1/2)$ is the relativistic angular momentum quantum number. These equations are solved subject to the boundary conditions

$$P_\kappa(0) = Q_\kappa(0) = 0. \quad (1.13)$$

The phase shift $\delta_{\ell a}$ is determined from the asymptotic behaviour of the radial function $P_\kappa(r)$ for large r ,

$$P_\kappa(r) \rightarrow r [j_\ell(kr) \cos(\delta_{\ell a}) - n_\ell(kr) \sin(\delta_{\ell a})], \quad (1.14)$$

where j_ℓ and n_ℓ are spherical Bessel and Neumann functions respectively.

1.2.2 Numerical phase shifts

In the present calculations, the numerical phase shifts are calculated by solving the radial wave equations using the RADWEQ package [SM91]. The function $rV(r)$ is replaced by the natural cubic spline which interpolates the values of this function for a given grid of points dense enough to ensure that interpolation errors have a negligible effect on the computed phase shifts. These are determined by using Bühring's power series method [Bu65]. This method of solution has two important advantages in comparison with the more conventional numerical procedures such as the Numerov, Runge-Kutta or Milne methods (see e.g. ref. [Fr77]) usually adopted to solve the radial equations. Firstly, truncation errors are completely avoided and, therefore, the radial

functions are only affected by unavoidable round-off errors. Secondly, the spacing of the grid of points where $rV(r)$ is tabulated has no effect on the accuracy of the numerical procedure (provided the interpolating spline does approach the actual field). The more conventional numerical methods require the use of grids dense enough to keep the effect of truncation errors below some reasonable limit and, therefore, the density of the grid must be increased for increasing energies to maintain the truncation error constant. The only disadvantage of the Bühring method is its higher cost in computer time.

For high-energy projectiles, the scattering amplitudes peak sharply at $\theta = 0$ and, as a consequence, a very large number of terms in the Legendre series (1.6) and (1.7) have to be summed before attaining convergence. When the number of computed phase shifts is not as large as required, the magnitude of truncation errors can be systematically diminished (at least for not too low scattering angles) by using the "reduced series" method of Yennie, Ravenhall and Wilson [YR54] to speed up the convergence of the Legendre series.

The reduced series method is based on the fact that, if the scattering amplitude $f(\theta)$ is strongly peaked at $\theta=0$, the function $(1 - \cos \theta)f(\theta)$ is smoother than $f(\theta)$, and hence its Legendre expansion may be more rapidly convergent. Explicitly, to sum up a series of the form given by eq. (1.6) which is weakly convergent (i.e. F_ℓ decreases slowly with ℓ for large ℓ) we consider the transformed series

$$\hat{f}(\theta) = (1 - \cos \theta)^n f(\theta) = \sum_{\ell=0}^{\infty} \mathcal{F}_\ell^n P_\ell(\cos \theta) \quad (1.15)$$

and compute $f(\theta)$ as $(1 - \cos \theta)^{-n} \hat{f}(\theta)$. The coefficients \mathcal{F}_ℓ^n are given by

$$\mathcal{F}_\ell^n = \mathcal{F}_\ell^{n-1} - \frac{\ell+1}{2\ell+3} \mathcal{F}_{\ell+1}^{n-1} - \frac{\ell}{2\ell-1} \mathcal{F}_{\ell-1}^{n-1} \quad (1.16)$$

and, for large ℓ , they decrease more rapidly with ℓ than the coefficients F_ℓ ($\equiv \mathcal{F}_\ell^0$) of the original series. It is easy to verify that if $\mathcal{F}_\ell^n \sim \mathcal{O}(\ell^b)$, then $\mathcal{F}_\ell^{n+1} \sim \mathcal{O}(\ell^{b-2})$. In the case of a series in associated Legendre functions such as $g(\theta)$ in eq. (1.7), the transformed series is

$$\hat{g}(\theta) = (1 - \cos \theta)^n g(\theta) = \sum_{\ell=0}^{\infty} \mathcal{G}_\ell^n P_\ell^1(\cos \theta) \quad (1.17)$$

with

$$\mathcal{G}_\ell^n = \mathcal{G}_\ell^{n-1} - \frac{\ell+2}{2\ell+3} \mathcal{G}_{\ell+1}^{n-1} - \frac{\ell-1}{2\ell-1} \mathcal{G}_{\ell-1}^{n-1}. \quad (1.18)$$

For large ℓ , \mathcal{G}_ℓ^n decreases more rapidly with ℓ than the coefficients G_ℓ ($\equiv \mathcal{G}_\ell^0$). Again, if $\mathcal{G}_\ell^n \sim \mathcal{O}(\ell^b)$, then $\mathcal{G}_\ell^{n+1} \sim \mathcal{O}(\ell^{b-2})$. Evidently, these summation methods cannot be used when $\theta \sim 0$.

1.2.3 WKB phase shifts

The Dirac eqs. (1.11) and (1.12) may be reduced to radial Schrödinger form by introducing the substitution

$$P_\kappa(r) = \eta^{1/2}(r)\mathcal{P}(r), \quad (1.19)$$

with $\eta(r) \equiv (E - V(r) + 2c^2)/c$, and eliminating the small radial function $Q_\kappa(r)$. The resulting equation is [MM65, Wa71]

$$\frac{d^2\mathcal{P}(r)}{dr^2} + \left[k^2 - \frac{\ell(\ell+1)}{r^2} - 2\mathcal{V}_\kappa(r) \right] \mathcal{P}(r) = 0 \quad (1.20)$$

where the effective Dirac potential

$$\mathcal{V}_\kappa(r) = \left(1 + \frac{E}{c^2}\right) V - \frac{1}{2} \frac{V^2}{c^2} + \frac{\kappa}{2r} \frac{\eta'}{\eta} + \frac{3}{8} \left(\frac{\eta'}{\eta}\right)^2 - \frac{1}{4} \frac{\eta''}{\eta} \quad (1.21)$$

depends on the energy and spin. For large r values η becomes a constant, i.e. \mathcal{P} becomes proportional to P_κ , and therefore the phase shifts may be computed by solving the Schrödinger eq. (1.20) as in the non-relativistic case. In particular, the WKB approximation with Langer correction yields [MM65]

$$\delta_{\ell a}^{(\text{WKB})} = \frac{1}{2} \left(\ell + \frac{1}{2}\right) \pi - kr_0 + \int_{r_0}^{\infty} \left[F_{\ell a}^{1/2}(r) - k \right] dr, \quad (1.22)$$

where

$$F_{\ell a}(r) \equiv k^2 - \frac{(\ell + 1/2)^2}{r^2} - 2\mathcal{V}_\kappa(r) \quad (1.23)$$

and r_0 is the (only) positive zero of $F_{\ell a}(r)$, i.e. the classical turning point for the radial motion in the field $\mathcal{V}_\kappa(r)$.

In the evaluation of WKB phase shifts for the analytical field eq. (1.4), we use a 20-point Gauss quadrature formula [AS74] complemented with a bipartition algorithm to allow for error control. The WKB phase shifts are obtained with a relative error smaller than 10^{-6} .

1.2.4 Born phase shifts

The relativistic form of the first Born approximation for the scattering amplitudes is [MM65]

$$f^{(\text{B})}(\theta) = \left[\gamma - \frac{\gamma-1}{2}(1 - \cos \theta) \right] f_0^{(\text{B})}(\theta), \quad (1.24)$$

$$g^{(\text{B})}(\theta) = \frac{\gamma-1}{2} \sin \theta f_0^{(\text{B})}(\theta), \quad (1.25)$$

where $\gamma \equiv 1 + E/c^2$.

$$f_0^{(B)}(\theta) = -2 \int_0^\infty \frac{\sin(qr)}{qr} V(r) r^2 dr \quad (1.26)$$

is the non-relativistic Born scattering amplitude, and $q = 2k \sin(\theta/2)$ is the momentum transfer.

Parzen [Pa50] obtained the following formulas for the relativistic Born phase shifts:

$$\delta_{\ell+}^{(B)} = \frac{\gamma+1}{2} \Delta_\ell^{(B)} + \frac{\gamma-1}{2} \Delta_{\ell+1}^{(B)}, \quad (1.27)$$

$$\delta_{\ell-}^{(B)} = \frac{\gamma+1}{2} \Delta_\ell^{(B)} + \frac{\gamma-1}{2} \Delta_{\ell-1}^{(B)}, \quad (1.28)$$

where

$$\Delta_\ell^{(B)} = -2k \int_0^\infty V(r) [j_\ell(kr)]^2 r^2 dr \quad (1.29)$$

are the non-relativistic Born phase shifts. It may be shown that

$$f^{(B)}(\theta) = \sum_{\ell=0}^{\infty} F_\ell^{(B)} P_\ell(\cos \theta), \quad (1.30)$$

$$g^{(B)}(\theta) = \sum_{\ell=0}^{\infty} G_\ell^{(B)} P_\ell^1(\cos \theta) \quad (1.31)$$

with

$$F_\ell^{(B)} = \frac{1}{k} [(\ell+1)\delta_{\ell+}^{(B)} + \ell\delta_{\ell-}^{(B)}], \quad (1.32)$$

$$G_\ell^{(B)} = \frac{1}{k} [\delta_{\ell-}^{(B)} - \delta_{\ell+}^{(B)}]. \quad (1.33)$$

For the particular case of the analytical field eq. (1.4) we have [SM87b]

$$f_0^{(B)}(\theta) = -2zZ \sum_{i=1}^3 \frac{A_i}{\alpha_i^2 + q^2} \quad (1.34)$$

and

$$\Delta_\ell^{(B)} = \frac{zZ}{k} \sum_{i=1}^3 A_i Q_\ell(1 + \alpha_i^2/2k^2), \quad (1.35)$$

where Q_ℓ are the Legendre functions of the second kind. The quantities $\Delta_\ell^{(B)}$ may be easily computed by using the recurrence relations satisfied by the Legendre functions [AS74] as described in appendix A.

WKB and Born phase shifts for 204 keV electrons scattered by mercury atoms are given in table 1.1. Inspection of these results indicates that the WKB approximation

is suitable for computing all phase shifts except those of lower orders which take the larger values. On the other hand, the relative differences between the numerical and Born phase shifts clearly decrease for increasing orders, becoming smaller than 0.1% for $\ell=100$ at the considered energy.

Table 1.1. Phase shifts for 204 keV electron scattering from Hg atoms.

ℓ	— Spin up —			— Spin down —		
	Numerical	WKB	Born	Numerical	WKB	Born
0	4.415(-1)	3.649(+0)	3.233(+0)	0.000(+0)	0.000(+0)	0.000(+0)
1	-5.095(-1)	2.648(+0)	2.466(+0)	-1.134(-1)	3.019(+0)	2.642(+0)
2	-9.552(-1)	2.190(+0)	2.080(+0)	-8.047(-1)	2.335(+0)	2.176(+0)
3	-1.240(+0)	1.902(+0)	1.825(+0)	-1.151(+0)	1.990(+0)	1.891(+0)
4	-1.446(+0)	1.695(+0)	1.638(+0)	-1.384(+0)	1.757(+0)	1.687(+0)
5	1.536(+0)	1.535(+0)	1.490(+0)	-1.558(+0)	1.582(+0)	1.529(+0)
6	1.407(+0)	1.406(+0)	1.370(+0)	1.445(+0)	1.444(+0)	1.402(+0)
7	1.300(+0)	1.299(+0)	1.269(+0)	1.331(+0)	1.330(+0)	1.297(+0)
8	1.209(+0)	1.208(+0)	1.183(+0)	1.235(+0)	1.234(+0)	1.206(+0)
9	1.130(+0)	1.129(+0)	1.108(+0)	1.153(+0)	1.152(+0)	1.128(+0)
10	1.061(+0)	1.060(+0)	1.042(+0)	1.081(+0)	1.080(+0)	1.060(+0)
12	9.444(-1)	9.439(-1)	9.297(-1)	9.601(-1)	9.596(-1)	9.443(-1)
14	8.496(-1)	8.493(-1)	8.380(-1)	8.625(-1)	8.621(-1)	8.501(-1)
16	7.705(-1)	7.702(-1)	7.611(-1)	7.813(-1)	7.810(-1)	7.713(-1)
18	7.032(-1)	7.029(-1)	6.954(-1)	7.124(-1)	7.121(-1)	7.042(-1)
20	6.449(-1)	6.447(-1)	6.384(-1)	6.529(-1)	6.527(-1)	6.461(-1)
30	4.403(-1)	4.402(-1)	4.373(-1)	4.448(-1)	4.447(-1)	4.417(-1)
40	3.171(-1)	3.170(-1)	3.155(-1)	3.199(-1)	3.198(-1)	3.183(-1)
50	2.360(-1)	2.360(-1)	2.351(-1)	2.379(-1)	2.379(-1)	2.370(-1)
70	1.400(-1)	1.400(-1)	1.397(-1)	1.410(-1)	1.410(-1)	1.407(-1)
100	7.195(-2)	7.194(-2)	7.186(-2)	7.237(-2)	7.236(-2)	7.228(-2)
200	1.328(-2)		1.328(-2)	1.334(-2)		1.334(-2)
500	2.648(-4)		2.647(-4)	2.657(-4)		2.657(-4)
1000	6.177(-7)		6.199(-7)	6.198(-7)		6.220(-7)

1.2.5 Simplified calculation method

The numerical work to evaluate the phase shifts for the analytical field eq. (1.4) can now be considerably reduced. In fact, the numerical solution of the corresponding radial equations is only required to determine the first phase shifts since those of intermediate and large orders can be obtained accurately from the WKB or the Born approximations. The simplified algorithm to compute the phase shifts proceeds as follows:

1. First, Born phase shifts, eqs. (1.27) and (1.28), are evaluated for all orders up to a value of $\ell = L$ large enough to guarantee the convergence of the series (1.6) and (1.7).
2. Numerical and WKB phase shifts, eq. (1.22), are then computed for increasing orders; the relative difference between these phase shifts decreases with the order and for a certain order $\ell = L_1$ it becomes smaller than a given value ϵ ($=5 \times 10^{-4}$ in the present calculations). The evaluation of numerical shifts is then discontinued.
3. For $\ell > L_1$, the phase shifts $\delta_{\ell\alpha}$ are approximated by the WKB phase shifts which are computed up to an order $\ell = L_2$ for which the relative differences between the WKB and Born phase shifts become smaller than ϵ .
4. For $\ell > L_2$, $\delta_{\ell\alpha}$ is approximated by the Born phase shift.

The accuracy of this scheme is mainly limited by ϵ . Of course, the value of ϵ has to be at least larger than the relative uncertainty due to round-off errors in the numerical phase shift; otherwise, the computation of exact shifts could never stop. For scattering of 204 keV electrons by mercury atoms, the orders at which the numerical and WKB computation stop are $L_1 = 8$ and $L_2 = 140$ respectively.

The Born approximation may also be used to speed up the convergence of the partial wave series (1.6) and (1.7). To this end, we write eqs. (1.6) and (1.7) in the form

$$f(\theta) = f^{(B)}(\theta) + \sum_{\ell=0}^{\infty} [F_{\ell} - F_{\ell}^{(B)}] P_{\ell}(\cos \theta), \quad (1.36)$$

$$g(\theta) = g^{(B)}(\theta) + \sum_{\ell=0}^{\infty} [G_{\ell} - G_{\ell}^{(B)}] P_{\ell}^1(\cos \theta), \quad (1.37)$$

where we have added the corresponding Born scattering amplitudes (1.24) and (1.25) and subtracted their partial wave expansions (1.30) and (1.31) on the right-hand side of

eqs. (1.6) and (1.7). As $\delta_{\ell a}^{(B)} \rightarrow \delta_{\ell a}$ for large ℓ values, the real parts of the series (1.36) and (1.37) will be more rapidly convergent than the original series (1.6) and (1.7). The use of the series (1.36) and (1.37), together with the reduced series method for scattering angles larger than $\sim 1^\circ$, leads to a considerable reduction of the numerical work.

The total elastic cross section σ and the first transport cross section (or momentum transfer cross section) σ_1 are given by

$$\sigma = 2\pi \int_0^\pi \frac{d\sigma}{d\Omega} \sin\theta \, d\theta \quad (1.38)$$

and

$$\sigma_1 = 2\pi \int_0^\pi (1 - \cos\theta) \frac{d\sigma}{d\Omega} \sin\theta \, d\theta. \quad (1.39)$$

Introducing the scattering amplitudes eqs. (1.36) and (1.37), and using the orthogonality of the Legendre polynomials, these integrals may be transformed into the following series

$$\sigma = \sigma^{(B)} + 4\pi \sum_{\ell=0}^{\infty} \frac{1}{2\ell+1} \left\{ |F_\ell|^2 - (F_\ell^{(B)})^2 + \ell(\ell+1) \left[|G_\ell|^2 - (G_\ell^{(B)})^2 \right] \right\} \quad (1.40)$$

and

$$\begin{aligned} \sigma_1 = & \sigma_1^{(B)} + \sigma - \sigma^{(B)} + \sum_{\ell=0}^{\infty} \frac{\ell+1}{(2\ell+1)(2\ell+3)} \\ & \times \left\{ F_\ell^* F_{\ell+1} + F_\ell F_{\ell+1}^* - 2F_\ell^{(B)} F_{\ell+1}^{(B)} \right. \\ & \left. + \ell(\ell+2) \left[G_\ell^* G_{\ell+1} + G_\ell G_{\ell+1}^* - 2G_\ell^{(B)} G_{\ell+1}^{(B)} \right] \right\}, \quad (1.41) \end{aligned}$$

where $\sigma^{(B)}$ and $\sigma_1^{(B)}$ are the total cross section and transport cross section obtained from the first Born approximation. The analysis of the convergence of the Legendre series (1.36) and (1.37) yields an estimate of the number of terms that have to be included in the series (1.40) and (1.41) to ensure its convergence.

Our computer code generates up to 4000 Born phase shifts, which ensure the convergence of the series (1.36) and (1.37) (usually with more than four significant digits) for energies up to ~ 20 MeV for all the elements. For larger energies, the convergence of the Legendre series is so slow that more than 4000 terms are required. With so many terms, the accumulation of truncation errors might become appreciable and, therefore, we have limited the partial wave calculations to $E \leq 20$ MeV. For higher energies, approximate methods remain essential.

For intermediate energies, where other calculations and experiments have been reported, our partial-wave DCSs are in good agreement with the most reliable calculations and experimental data available. However, our calculations extend up to much higher energies than the previous ones and this demands a careful check of their global accuracy. Such a check can be easily done for high energies and large scattering angles, where screening effects are expected to be small. Then, differences between the partial wave DCS and the screened Mott DCS, see eq. (1.60) below, should reduce for increasing energies. Actually, for energies above 1 MeV and angles larger than $\sim 10^\circ$, our DCS and the screened Mott DCS practically coincide. Owing to the slow convergence of the partial wave series for forward scattering, numerical uncertainties tend to concentrate at small scattering angles. For these angles, the eikonal approximation is known to give very accurate estimates of the DCSs [ZO64] (since spin effects are negligible there). For forward scattering, we have found that the differences between our partial wave DCS and the DCS obtained from the eikonal approximation are less than 0.1%.

As regards multiple scattering simulation, the relevant quantities are the transport cross sections σ_ℓ defined by [GS40a,Le50]

$$\sigma_\ell = 2\pi \int_0^\pi [1 - P_\ell(\cos \theta)] \frac{d\sigma}{d\Omega} \sin \theta d\theta. \quad (1.42)$$

We will see in chapter 2 that knowledge of the first and second transport cross sections are particularly important. In particular, these two quantities suffice to determine a simulation algorithm which is more reliable than the simulation schemes based on Molière's theory. Therefore, the approximate DCSs adopted in Monte Carlo algorithms should yield the correct values of the first and second transport cross sections to ensure good simulation results.

Partial wave calculations have been performed for electrons and positrons with kinetic energy from 1 keV to 20 MeV, and 20 elements covering the periodic system. For each of these elements, the DCS and the corresponding first and second transport cross sections have been obtained for 41 values of the energy uniformly spaced in a logarithmic scale. Selected results from these calculations are shown in figs. 1.1–1.2.

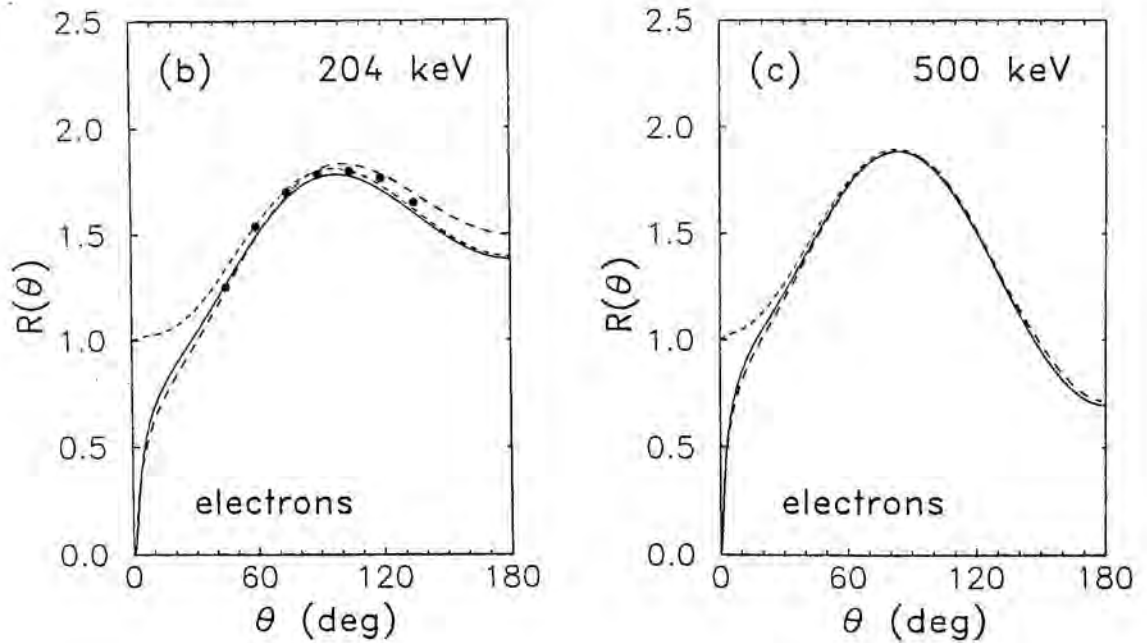


Figure 1.1. DCSs for elastic scattering of 204 and 500 keV electrons by mercury atoms as functions of the scattering angle. The plotted DCSs are the result of the present partial wave calculation (long-dashed curve), the Mott DCS for the unscreened nucleus given by eq. (1.47) (short-dashed curve) and the corrected screened Mott DCS, eq. (1.60) (continuous curve). Circles are experimental data from Kessler and Weichert [KW65].

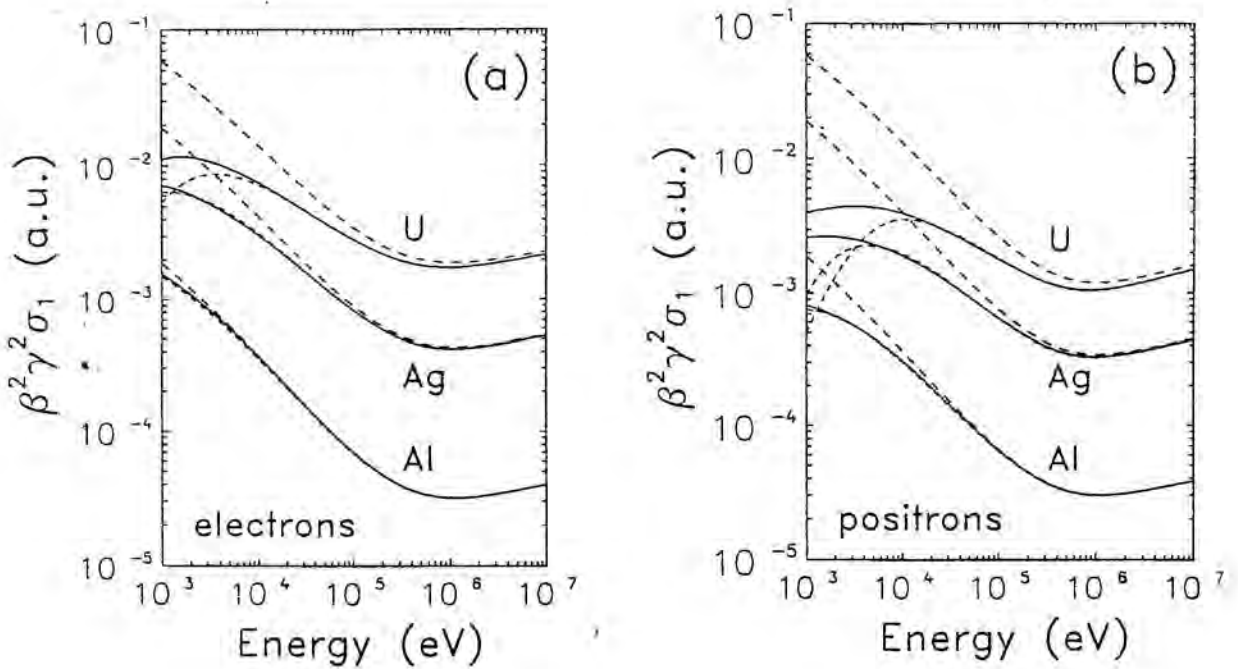


Figure 1.2. First transport cross sections for electrons (a) and positrons (b) scattered by Al, Ag and U atoms as functions of the kinetic energy of the projectile. The quantity plotted is $\beta^2 \gamma^2 \sigma_1$ in atomic units ($1 \text{ a.u.} = 2.8 \times 10^{-17} \text{ cm}^2$). The continuous curves are the results of the present partial wave calculations. The long- and short-dashed curves correspond to σ_1 computed from the screened Mott cross section, eq. (1.60), and from the corrected screened Mott DCSs, eq. (1.67), respectively. Partial wave results from ref. [RM75] are indicated by crosses.

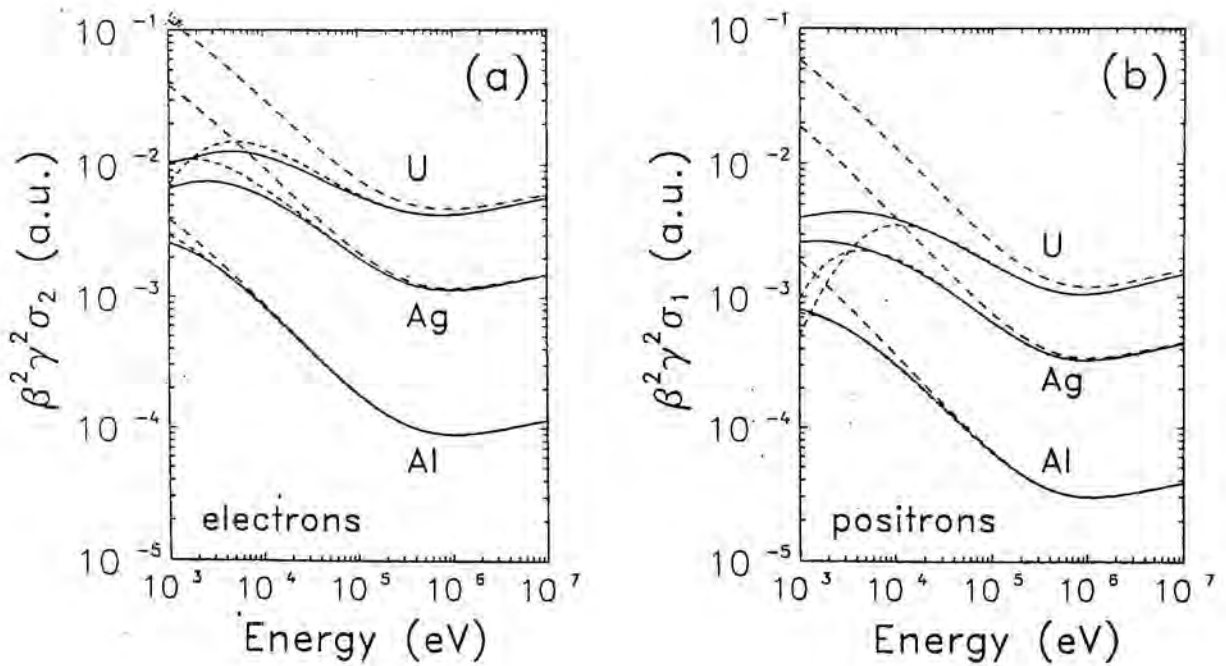


Figure 1.3. Second transport cross sections for electrons (a) and positrons (b) scattered by Al, Ag and U atoms as functions of the kinetic energy of the projectile. The quantity plotted is $\beta^2\gamma^2\sigma_2$ in atomic units. Other details are the same as in fig. 1.2.

1.3 Screened Mott cross section

The simplest method to estimate the DCS is provided by the Born approximation. The Born DCS for a spinless electron or positron with kinetic energy E is given by [MM65]

$$\frac{d\sigma_B}{d\Omega} = \frac{(2m\gamma zZe^2)^2}{q^4} [1 - F_e(q)]^2, \quad (1.43)$$

where m is the electron mass, $\gamma \equiv (1 - \beta^2)^{-1/2}$ is the energy of the projectile in units of the rest energy mc^2 , and $F_e(q)$ is the atomic form factor. The quantity q is the momentum transfer, which is related to the linear momentum $p = \gamma m\beta c$ and to the polar scattering angle θ through $q = 2p \sin(\theta/2)$. Notice that, owing to the large mass difference between the target atom and the projectile, the first can be considered as infinitely massive, i.e. the scattering angle is always referred to the laboratory frame of reference. The atomic form factor for the electron density corresponding to the screening function eq. (1.3) is [SM87a]

$$F_e(q) = \sum_{i=1}^3 A_i \frac{(\hbar\alpha_i)^2}{(\hbar\alpha_i)^2 + q^2}. \quad (1.44)$$

The first factor in eq. (1.43) is just the Rutherford DCS

$$\frac{d\sigma_R}{d\Omega} = \left(\frac{zZe^2}{mc^2} \right)^2 \frac{1 - \beta^2}{\beta^4} \frac{1}{(1 - \cos \theta)^2}, \quad (1.45)$$

i.e. the DCS for scattering of a spinless particle in the Coulomb field

$$V_C(r) = \frac{zZe^2}{r} \quad (1.46)$$

of the bare nucleus. Screening effects are accounted for by the factor $[1 - F_e(q)]^2$, which vanishes for $q=0$, thus leading to a finite DCS for forward scattering. For large momentum transfers, this factor approaches unity and the DCS reduces to the Rutherford DCS, i.e. screening effects become negligible in the limit of large momentum transfers.

Let us now consider the effect of electron spin in elastic collisions. In order to investigate this effect it is useful to start from the case of scattering by the (unscreened) Coulomb field of the nucleus, eq. (1.46). Exact relativistic phase shifts for this field are known analytically [MM65] and the DCS, hereafter referred to as the unscreened Mott DCS, may be computed with a modest amount of numerical work. We have [DS56, Sh56, VP74]

$$\frac{d\sigma_M}{d\Omega} = |f_M(\theta)|^2 + |g_M(\theta)|^2. \quad (1.47)$$

The direct and spin-flip scattering amplitudes $f_M(\theta)$ and $g_M(\theta)$ can be obtained from

$$f_M(\theta) = (\hbar/p) \left[-i\gamma^{-1}\zeta F(\theta) + G(\theta) \right], \quad (1.48)$$

$$g_M(\theta) = (\hbar/p) \left[i\gamma^{-1}\zeta(1 + \cos\theta)F(\theta) + (1 - \cos\theta)G(\theta) \right] / \sin\theta, \quad (1.49)$$

where $\zeta \equiv -\chi/\beta$ with $\chi \equiv \alpha zZ$ and α the fine-structure constant. The complex functions $F(\theta)$ and $G(\theta)$ are defined by

$$F(\theta) = F_0(\theta) + F_1(\theta) \quad (1.50)$$

$$G(\theta) = G_0(\theta) + G_1(\theta) \quad (1.51)$$

$$F_0(\theta) = \frac{i}{2} \frac{\Gamma(1 - i\zeta)}{\Gamma(1 + i\zeta)} \exp[2i\zeta \ln(\sin(\theta/2))] \quad (1.52)$$

$$F_1(\theta) = \frac{i}{2} \sum_{\ell=0}^{\infty} (-1)^\ell [\ell D_\ell + (\ell + 1)D_{\ell+1}] P_\ell(\cos\theta) \quad (1.53)$$

$$G_0(\theta) = -i\zeta F_0(\theta) \cot^2(\theta/2) \quad (1.54)$$

$$G_1(\theta) = \frac{i}{2} \sum_{\ell=0}^{\infty} (-1)^\ell [\ell^2 D_\ell - (\ell + 1)^2 D_{\ell+1}] P_\ell(\cos\theta) \quad (1.55)$$

with

$$D_\ell = \frac{\exp(-i\pi\ell)}{\ell + i\zeta} \frac{\Gamma(\ell - i\zeta)}{\Gamma(\ell + i\zeta)} - \frac{\exp(-i\pi\rho_\ell)}{\rho_\ell + i\zeta} \frac{\Gamma(\rho_\ell - i\zeta)}{\Gamma(\rho_\ell + i\zeta)}, \quad (1.56)$$

where Γ is the complex gamma function and $\rho_\ell \equiv (\ell^2 - \chi^2)^{1/2}$. The Mott DCS, eq. (1.47), can be given in terms of the functions $F(\theta)$ and $G(\theta)$ as [Sh56]

$$\frac{d\sigma_M}{d\Omega} = (\hbar/p)^2 \left[\frac{\zeta^2 \gamma^{-2} |F(\theta)|^2}{\sin^2(\theta/2)} + \frac{|G(\theta)|^2}{\cos^2(\theta/2)} \right]. \quad (1.57)$$

It is customary to write the exact Mott DCS in the form

$$\frac{d\sigma_M}{d\Omega} = \frac{d\sigma_R}{d\Omega} R(\theta). \quad (1.58)$$

The ratio $R(\theta)$ of the Mott DCS, eq. (1.47), to the Rutherford DCS, eq. (1.45), gives a direct measure of the effect of spin on the DCS. The computation of $R(\theta)$ is performed by using the numerical procedure described by Sherman [Sh56] (see also ref. [VP74]). For small scattering angles ($\theta < 10^\circ$), where the series (1.53) and (1.55) are slowly convergent, we use the asymptotic formula attributed to Bartlett and Watson [MO64]

$$R(\theta) = 1 + \pi\beta^2\zeta \operatorname{Re} \left[\frac{\Gamma(\frac{1}{2} - i\zeta)}{\Gamma(\frac{1}{2} + i\zeta)} \frac{\Gamma(1 + i\zeta)}{\Gamma(1 - i\zeta)} \right] \sin(\theta/2). \quad (1.59)$$

For $\theta > 10^\circ$, these series are summed up by using the reduced series method of Yennie, Ravenhall and Wilson [YR54,Sh56]: instead of summing the original series $F_1(\theta)$ and $G_1(\theta)$, we sum the transformed series $(1 - \cos \theta)^2 F_1(\theta)$ and $(1 - \cos \theta)^2 G_1(\theta)$ which are much more rapidly convergent. We consider a maximum of 200 terms in the series; the accuracy of the resulting $R(\theta)$ values is usually better than 0.01%.

We note that the spin correction $R(\theta)$ approaches unity for small scattering angles, as clearly seen from eq. (1.59); it differs from this value only for high energies and not too low scattering angles, whereas the screening effects are unimportant under these conditions, i.e. $[1 - F_e(q)]^2 \sim 1$. Thus, it is sensible to approximate the exact DCS for the screened field in the form [Be63,ZO64]

$$\frac{d\sigma}{d\Omega} = \frac{d\sigma_R}{d\Omega} R(\theta) [1 - F_e(q)]^2, \quad (1.60)$$

where the second and third terms account for spin and screening effects respectively. Hereafter, the DCS eq. (1.60) will be referred to as the “screened” Mott DCS.

A comparison of the first transport cross section σ_1 obtained from the screened Mott DCS eq. (1.60) with our partial wave results shows that the formula (1.60) is quite accurate for energies above 1 keV and low atomic numbers, say $Z < 10$. For higher atomic numbers the deficiencies of the Born approximation, which has been used to introduce screening effects in eq. (1.60), become prominent. In particular, the first transport cross section obtained from the screened Mott DCS are too large. Our goal here is to empirically improve the screened Mott DCS, eq. (1.60), so as to reproduce the correct (partial wave) first transport cross sections, at least for moderately high energies.

1.4 Improved high-energy formulas

Several “improved formulas” are based on the introduction of a “screening angle” as proposed by Molière [Mo47]. As these formulas are frequently adopted in Monte Carlo simulations, we feel convenient to discuss here their validity on the basis of our partial wave results. Molière [Mo47] started from the DCS obtained by using the eikonal approximation and an screening function of the form (1.3) with parameters determined from the Thomas-Fermi field. Moreover he neglected spin effects so that, within his approach, the DCSs for electrons and positrons are identical and for large momentum transfers they go over into the Rutherford DCS. In order to make possible further

analytical calculations, Molière considered an analytical DCS which in our notation reads (cf. eq. (1.43))

$$\frac{d\sigma}{d\Omega} = \frac{d\sigma_R}{d\Omega} [1 - F_W(q)]^2 \quad (1.61)$$

with the form factor obtained from the Wentzel [We27] model

$$F_W(q) = \frac{(\hbar\alpha_W)^2}{(\hbar\alpha_W)^2 + q^2} \quad (1.62)$$

that corresponds to the exponential screening function $\phi(r) = \exp(-\alpha_W r)$, where $\alpha_W = 1.13Z^{1/3}a_0^{-1}$ is the inverse of the Thomas-Fermi radius. The DCS eq. (1.61) for large scattering angles, and not too low energies, is essentially identical to the eikonal DCS since the screening effects are then small ($q \ll \alpha_W$). Differences between these two DCSs for small momentum transfers are governed by the value of α_W , which may be considered as an energy-dependent adjustable parameter. As regards multiple scattering theory, this parameter should be determined in such a way that the approximate DCS leads to the same value of the first transport cross section as the accurate (eikonal) DCS. From a numerical fit of essentially the first transport cross section computed from the eikonal approximation, Molière concluded that the screening parameter may be approximated as

$$\alpha_M = t_M \alpha_W \quad (1.63)$$

with

$$t_M = [1.13 + 3.76(\alpha Z/\beta)^2]^{1/2}. \quad (1.64)$$

Introducing this corrected screening parameter into eqs. (1.62) and (1.61) we obtain

$$\frac{d\sigma_{\text{Molière}}}{d\Omega} = \frac{d\sigma_R}{d\Omega} \left[\frac{q^2}{(\hbar t_M \alpha_W)^2 + q^2} \right]^2. \quad (1.65)$$

It has been repeatedly claimed that multiple scattering distributions are completely determined by the value of the first transport cross section [Mo48,Be53,SB82,IS89]. However, stated in this way, this assertion is false. To be true it must be complemented with the requirement that the single scattering DCS has the correct behaviour for large scattering angles where the form factor $F_e(q)$ is small (see chapter 2). For not too large energies, that is when finite nuclear size effects are negligible, the correct large-angle behaviour is given by the unscreened Mott DCS, eq. (1.47). This means that Molière's DCS is subject to criticism since, for large scattering angles, it goes over into the Rutherford rather than the Mott DCS. This drawback was remedied by Berger [Be63] who combined Molière's approximation for screening with the (unscreened) Mott DCS

thus obtaining a DCS with the proper large-angle behaviour. Berger's cross section reads

$$\frac{d\sigma_{\text{Berger}}}{d\Omega} = \frac{d\sigma_{\text{R}}}{d\Omega} R(\theta) \left[\frac{q^2}{(\hbar t_{\text{M}} \alpha_{\text{W}})^2 + q^2} \right]^2 \quad (1.66)$$

which is certainly more accurate than Molière's DCS. However, both approaches share two important limitations, namely, 1) the Wentzel form factor is too simple to accurately represent a real atom, and 2) screening effects are introduced from the eikonal approximation, which is a small-angle high-energy approximation [Sc68], rather than from an accurate partial wave calculation, which was unfeasible at that time. Notice that although eq. (1.66) gives different DCSs for electrons and positrons, the screening correction factor, i.e. t_{M}^{-1} , is the same for the two kinds of particles.

To overcome the first limitation, we will use the analytical atomic form factors given by eq. (1.44) with parameters determined from the DHFS density [SM87a], which are accurate enough for our purposes. As already mentioned, the screened Mott DCS, eq. (1.60), for large momentum transfers such that $F_e(q) \ll 1$ (i.e. large scattering angles, and not too low energies) is essentially correct. This is evidenced in fig.1.1, where this DCS is compared with the partial wave DCS. Thus, the screened Mott DCS, eq. (1.60), differs from the "exact" DCS only for small and intermediate momentum transfers and can be improved by means of an empirical correction similar to the one used by Berger, namely of the form

$$\frac{d\sigma}{d\Omega} = \frac{d\sigma_{\text{R}}}{d\Omega} R(\theta) \left[1 - F_e(t^{-1}q) \right]^2, \quad (1.67)$$

where $t(Z, E)$ is a function of the atomic number and the energy. This quantity is determined by fitting the first transport cross section obtained from our partial wave calculations, thus overcoming the second of the aforesaid limitations. We point out that the scattering field used in our partial wave calculations and the form factor adopted in eq. (1.67) correspond to *strictly* the same atomic density. As a consequence, our t correction will *exclusively* account for the inaccuracies of introducing screening effects through the Born factor $[1 - F_e(q)]^2$. This is not so in Molière's treatment where t_{M} accounts for these inaccuracies *and* for the changes introduced by the replacement of the Thomas-Fermi form factor by the Wentzel form factor. It is worth noting that this correction improves the DCS for the scattering angles which effectively contribute to σ_1 , but it does not suffice to reproduce the PWA-DCS for very small angles. Fortunately, the details of the DCS at these small angles do not have any influence on the multiple scattering distributions.

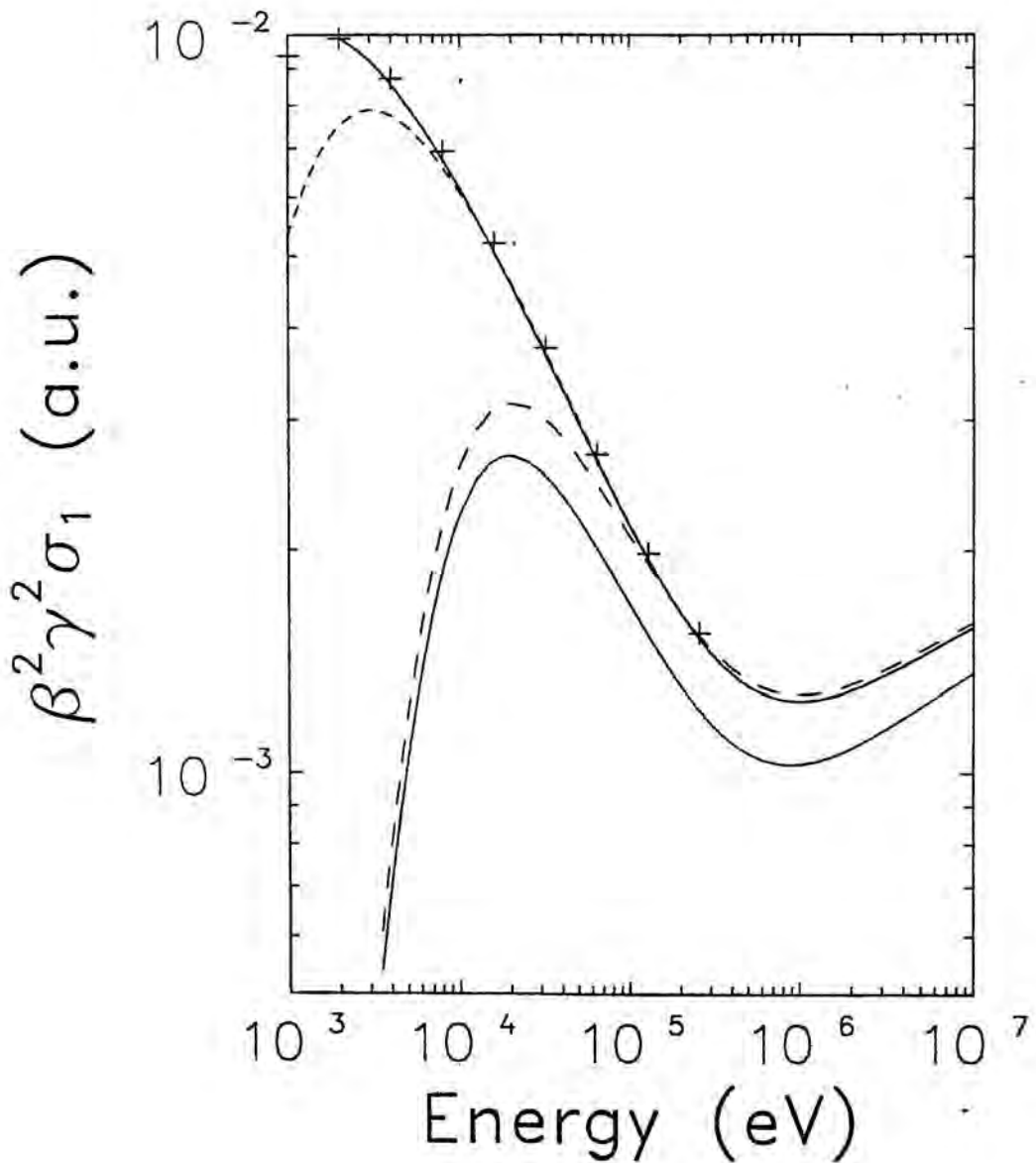


Figure 1.4. First transport cross section for electron scattering by gold atoms as a function of the kinetic energy. The quantity plotted is $\beta^2 \gamma^2 \sigma_1$ in atomic units. Curves are the result from our partial wave calculations (continuous), from the corrected screened Mott formula, eq. (1.67) (dot-dashed), from the Molière DCS, eq. (1.65) (short-dashed), from the Berger DCS, eq. (1.66) (long dashed).

It turns out that the correcting factor $t(Z, E)$ varies smoothly with atomic number and energy, and then it is amenable to be approximated by an analytical expression. For energies above $\sim Z$ keV, the formulas

$$t^{(-)}(Z, E) = 1 + 1.053(\alpha Z)^{1.971} + [0.00569 + 0.995(\alpha Z)^{1.778}] \left(\frac{1}{\beta} - 1\right)^{0.750} \quad (1.68)$$

for electrons, and

$$t^{(+)}(Z, E) = 0.988 + 0.914(\alpha Z)^{1.670} + 2.191(\alpha Z)^{1.399} \left(\frac{1}{\beta} - 1\right)^{1.167} \quad (1.69)$$

for positrons, when used in eq. (1.67), reproduce the numerical values of the first transport cross section obtained from the partial-wave calculation to within less than 1%. For energies less than Z keV the accuracy of the formula (1.67) progressively deteriorates. However, this formula still yields results substantially more accurate than those from the screened Mott formula (1.60) if the t factor is evaluated according to eqs. (1.68) and (1.69) but using the value of β corresponding to a kinetic energy $E_c = 0.25Z$ keV when E is less than E_c . The results presented below have been obtained with this prescription.

We would like to stress the fact that the t corrections for electrons and positrons are different; this is in contrast with the approaches of Berger [Be63] and Molière [Mo47]. Our screening correction is also superior to the one derived by Nigam et al. [NS59] which shares the limitations of the second Born approximation on which it was based. Moreover, the accuracy of our approach improves when the energy increases since then screening effects concentrate nearer the forward direction.

Fig. 1.2 shows σ_1 as a function of energy for electrons and positrons scattered by Al ($Z = 13$), Ag ($Z = 47$) and U ($Z = 92$) atoms as computed from eqs. (1.60), (1.67) and from our partial wave calculations. Values from the tables in ref. [RM75] are also included for comparison purposes. The improvement due to the introduction of the screening correction factor t , eqs. (1.68) and (1.69), is seen to be remarkable for intermediate energies and essential for high atomic numbers. As shown in fig. 1.2, our empirical DCS, eq. (1.67), gives also good estimates of the second transport cross section σ_2 for energies above its limit of validity ($E > Z$ keV).

1.4.1 Nuclear size effects

At high kinetic energies (say above ~ 10 MeV), we should also consider the effect of the finite size of the nucleus, which may influence the multiple scattering distributions [Sc63] (but is usually neglected in Monte Carlo simulations of electron and positron transport). An accurate treatment which simultaneously includes screening, spin and finite nuclear size effects is not feasible. Again, we resort to the Born approximation [MM65] and notice that, within this approximation, the ratio of the DCSs for a finite nucleus and a point nucleus of the same charge equals the squared form factor of the finite nucleus. Thus, we set

$$\frac{d\sigma}{d\Omega} = \frac{d\sigma_R}{d\Omega} R(\theta) [1 - F_e(t^{-1}q)]^2 |F_n(q)|^2, \quad (1.70)$$

where $F_n(q)$ is the form factor of the nuclear charge distribution $\rho_n(r)$ which reduces to unity for a point nucleus. To obtain a simple analytical expression for the nuclear form factor, we adopt Helm's uniform-uniform folded charge distribution [He56]:

$$\rho_n(r) = \int \rho_0(r') \rho_1(r - r') dr', \quad (1.71)$$

where ρ_0 and ρ_1 are uniform distributions (normalized to unity) over spheres of radii

$$R_0 = 1.2 \times 10^{-13} A^{1/3} \text{ cm}, \quad R_1 = 2.0 \times 10^{-13} \text{ cm}, \quad (1.72)$$

where A is the mass number of the considered nucleus. This charge distribution decreases smoothly at the surface of the nucleus and, for spherical nuclei, yields results more realistic than the cruder uniform spherical distribution. The corresponding form factor is

$$F_n(q) = F(R_0, q) F(R_1, q), \quad (1.73)$$

where

$$F(R, q) = \frac{3}{(qR/\hbar)^3} [\sin(qR/\hbar) - (qR/\hbar) \cos(qR/\hbar)] \quad (1.74)$$

is the form factor for a uniformly charged sphere. It is well known that the form factor (1.74) introduces spurious zeros in the DCS which, nevertheless, coincide quite accurately with the inflexion points of the experimental DCS for spherical nuclei (see fig. 1.5).

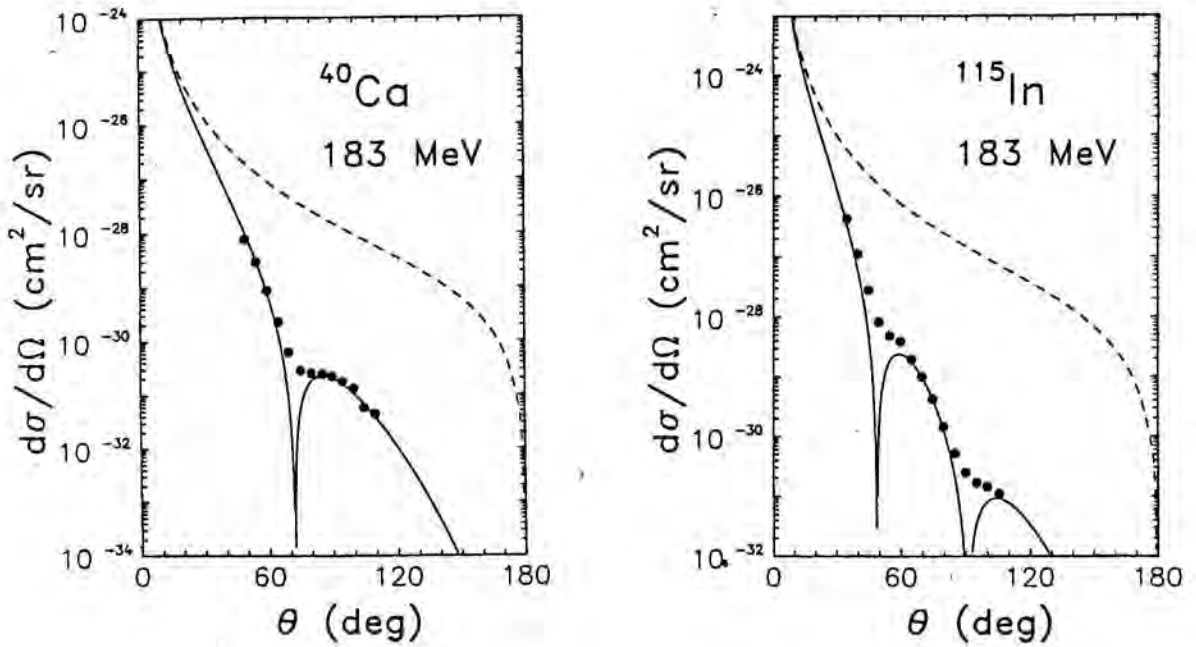


Figure 1.5. DCSs for 183 MeV electrons scattered by ^{40}Ca ($Z=20$) and ^{115}In ($Z=49$) atoms. The continuous and dashed curves are corrected screened Mott DCSs with and without finite nuclear size correction, eqs. (1.70) and (1.67), respectively. Experimental data are from Hahn et al. [HR56].

The global effect of the finite size of the nucleus is a reduction of the DCS for large scattering angles, which sharpens the multiple scattering distributions. To give an idea of the magnitude of this effect, first transport cross sections for electrons and various elements and energies computed including this effect and neglecting it are compared in table 1.2. From these results we conclude that the neglect of the nuclear size effect gives σ_1 values which are a few percent too high and, consequently (see chapter 2) it gives multiple scattering angular distributions which are too wide in approximately the same proportion.

Table 1.2. First transport cross sections for electrons scattered by Al, Ag and U atoms computed from eqs. (1.67) and (1.70) respectively, i.e. neglecting and including finite nuclear size correction.

Element, Z	E (MeV)	λ_1	$\lambda_1^{(M)}$
Al, 13	1	4.098(-6)	4.098(-6)
	10	9.475(-8)	9.459(-8)
	100	1.383(-9)	1.285(-9)
Ag, 47	1	5.396(-5)	5.395(-5)
	10	1.254(-6)	1.247(-6)
	100	1.825(-8)	1.548(-8)
U, 92	1	2.250(-4)	2.249(-4)
	10	5.190(-6)	5.106(-6)
	100	7.416(-8)	5.286(-8)

1.5 Concluding remarks

We have derived a relatively simple formula, eq. (1.67), which offers a reliable description of elastic scattering of electrons and positrons with kinetic energies larger than $\sim Z$ keV by neutral atoms. The main advantage of the present approach is that the first transport cross section, and the large-angle behaviour of the DCS, obtained from partial wave calculations are correctly reproduced with only a modest amount of numerical work. This feature guarantees that the present DCSs will give accurate results when used in high-energy Monte Carlo simulations.

The most accurate multiple scattering theory [GS40a,Le50] involve the transport cross sections σ_t , whereas the simpler Molière [Mo48] theory only involves σ_1 . The numerical evaluation of the integrals (1.38) and (1.39) can be easily done with the aid of an adaptive integration routine able to deal with strongly peaked functions. In the present calculations, we have used a 20-point Gauss quadrature method complemented with a bipartition algorithm which allows error control. The evaluation of σ_1 and σ_2 takes only a fraction of a second, even with a personal computer. Thus the present method can be readily used to improve the Molière [Mo48] multiple scattering theory by simply modifying the parameters in this theory so as to reproduce the first and second transport cross section obtained with the present method (see chapter 2).

It is worth pointing out that the actual DCS for intermediate and high atomic numbers develops diffraction peaks at low energies [MM65,SM87b] so that it cannot be reproduced by an expression such as our eq. (1.67) which, even for small energies, is a monotonously decreasing function of the scattering angle. In any case, for energies less than $\sim Z$ keV one should exclusively use accurate partial wave DCSs which can be either directly computed [Sa91] or interpolated from available tabulations [RM75,RL84].

Chapter 2

Multiple scattering

2.1 Introduction

Monte Carlo simulation is being used as an efficient method to solve electron (and positron) transport problems [Be63,NH85,RK76]. The existing simulation algorithms can be classified in two different kinds, namely detailed simulations and “condensed” simulations. Detailed simulations, where all the collisions experienced by an electron are simulated in chronological succession, are feasible when the average number of collisions per track is not too large (say up to a few hundreds). Apart from the inherent statistical uncertainties, detailed simulation is exact, i.e. it yields the same results as the rigorous solution of the transport equation. Experimental situations amenable to detailed simulation are those involving either electron sources with low initial kinetic energies (say up to about 100 keV) or special geometries such as electron beams impinging on thin foils. For larger initial energies, and thick geometries, the average number of collisions experienced by an electron until it is effectively stopped becomes very large, and the detailed simulation becomes very inefficient. The high energy simulation codes currently available have recourse to approximate multiple scattering theories, which allow the simulation of the global effect of the collisions that occur in a track segment of a given length. Each track is simulated as a moderately small number of connected “steps” of a specified length that is much larger than the mean free path between real collisions, so that a large number of collisions takes place along each step. The step length is either internally determined by the simulation code or specified by the user. The net displacement, energy loss and change of direction of the electron after travel-

ing a certain step are evaluated from the multiple scattering theories. The accuracy of these condensed simulation methods is thus limited by the approximations introduced in the adopted multiple scattering theories.

Angular deflections of the electron tracks are mainly due to elastic scattering with nuclei screened by the surrounding electron cloud. As regards Monte Carlo simulation, elastic scattering and energy loss processes can be considered separately. This is strictly correct for detailed simulation, and it is approximately valid for condensed simulations provided we consider only short steps such that the fractional energy loss in each step is small in front of the kinetic energy at the beginning of the step. Owing to this fact, elastic angular deflections in condensed Monte Carlo simulations can be described by using a multiple scattering theory that neglects the energy loss in each single step, i.e. a purely elastic multiple scattering theory. For the sake of simplicity, we shall limit our considerations to this kind of theories. Corrections to account for the energy loss along each step can be introduced by using the continuous slowing down approximation as described by Lewis [Le50] and Berger [Be63].

The usual practice in condensed Monte Carlo simulations is to use the theories due to Molière [Mo48,Be53], Goudsmit and Saunderson [GS40a,GS40b] and Lewis [Le50]. The first two of these theories give only the angular distribution after a given path length without any information about the spatial distribution. The approach of Lewis [Le50] allows also the calculation of the first moments of the spatial distribution. The main uncertainties in condensed simulations originate from the lack of detailed knowledge on the probability distribution of the spatial displacement. Each simulation code incorporates a well-defined algorithm to determine the spatial displacement of the electron at the end of each step. These algorithms are not exact and, therefore, simulated spatial distributions, and other related quantities, are influenced by the value of the selected step length in a quite unpredictable way. The reliability of the simulation results must be therefore checked through a detailed study of their dependence on the selected step length. Generally, it happens that when reducing the step length the results converge to the correct value but the computation time increases rapidly (roughly in proportion to the inverse of the step length).

Bielażew and Rogers [BR86] have developed the algorithm PRESTA, based on the multiple scattering theory of Molière, which approximately accounts for the differences between the actual longitudinal displacement and the true path length of a step. It also accounts for the lateral displacement in the step and includes a boundary crossing

strategy, which ensures that electron tracks are properly simulated in the vicinity of interfaces. The work of these authors represents an effective improvement of the previous condensed simulation procedures. In particular, the dependence of the simulation results on the adopted step length is largely reduced. However, the use of the Molière theory is open to question [AM91] and, moreover, only the mean values of the longitudinal and transverse displacements in each step are considered, i.e. straggling in the spatial displacement after each step is neglected.

The aim of the present work is to review briefly the most habitual multiple scattering theories, to discuss their reliability when used in condensed simulations and to present a new simulation algorithm that overcomes most of the limitations of the currently available high-energy Monte Carlo codes. Our simulation method takes advantage of the fact that most of the collisions experienced by a high energy electron along a given path length are “soft”, i.e. they produce very small angular deflections. The global effect of these soft collisions can be described by using a “continuous scattering approximation”, in the same spirit as the habitual continuous slowing down approximation for inelastic scattering. The moderately small number of “hard” collisions, with large scattering angles, can then be simulated in a detailed way. This procedure, which can be applied to any single scattering law, does not require any preselected step length, yields the correct spatial distributions and does not pose any problem with boundary crossing. Furthermore, when using a single scattering differential cross section of the Wentzel type [We27] (i.e. with the same analytical form as the one underlying Molière’s theory), our simulation algorithm can be formulated through a few very simple analytical expressions.

The chapter is structured as follows. In section 2.2 relevant multiple scattering theories are briefly reviewed. We offer a simple derivation of the Molière theory that serves to point out its physical content and limitations. The new simulation algorithm is described in section 2.3. In the next section, this algorithm is applied to the Wentzel cross section [We27] to yield a simulation procedure that, in spite of its simplicity, is more accurate than the currently available algorithms based on Molière’s theory. Useful mathematical information is given in the appendices.

2.2 Multiple scattering theories

We consider electrons (or positrons) with kinetic energy E moving in a hypothetical infinite homogeneous medium, with N scattering centers per unit volume, in which they experience only elastic collisions. We assume that the single scattering differential cross section (DCS) per unit solid angle $d\sigma(\chi)/d\Omega$ depends only on the polar scattering angle χ , i.e. it is axially symmetric about the incident direction. This assumption is satisfied as long as the scattering centers are spherically symmetrical atoms or randomly oriented molecules [MM65]. Moreover, interference effects resulting from coherent scattering by several centers are assumed to be negligible. As a consequence, the theory is applicable only to amorphous materials and, with some care, to polycrystalline solids. For the sake of simplicity, we limit our considerations to single-element materials; the generalization to compounds is straightforward. Notice that the number of scattering centers per unit volume is given by $N = N_A \rho / A_w$ where N_A is Avogadro's number, ρ is the mass density of the material and A_w is the atomic weight.

A class of Monte Carlo simulation codes uses the multiple scattering theory of Molière [Mo48]—see also refs. [Be53] and [Sc63]. This theory is based on certain assumptions about the single scattering DCS and incorporate mathematical approximations that render the final distribution fully analytical. The particular DCS underlying Molière's theory is based on the eikonal approximation [Mo47,Sc68], which is a high-energy small-angle approximation and neglects spin effects. Nigam et al. [NS59] reformulated the theory on the basis of the DCS obtained from the second Born approximation and a scattering field of Wentzel type [We27], i.e. an exponentially screened Coulomb field. It is well known that the second Born approximation fails for intermediate and high atomic numbers [Sa91], even for an unscreened Coulomb field [MO64]. Moreover, the actual screened field may depart appreciably from the Wentzel one (and also from the Thomas-Fermi field adopted by Molière).

More accurate simulation procedures are based on the multiple scattering theory of Goudsmit and Saunderson [GS40a] and Lewis [Le50], which allows the calculation of the exact angular distribution due to multiple elastic scattering after a given path length by means of an expansion in Legendre polynomials. This theory does not assume any particular form of the single scattering DCS and is essentially exact, i.e. errors in the computed multiple scattering distributions can always be traced back to inaccuracies in the adopted DCS.

2.2.1 Single scattering differential cross sections

The most reliable DCSs available to date are obtained from relativistic (Dirac) partial wave analysis using a realistic scattering field [RM75,Sa91], which can be obtained from self-consistent Hartree-Fock atomic calculations. Detailed simulations based on these differential cross sections have been shown to yield results in good agreement with experimental data for kinetic energies up to ~ 100 keV [RK76]. Partial wave calculations for screened fields are feasible for energies up to ~ 20 MeV [Sa91]. For higher energies, the Mott differential cross section for a point unscreened nucleus [MM65], suitably corrected to account for screening effects and for nuclear size effects [Be63,FM92], is accurate enough for simulation purposes.

The DCSs used in the present work, have been calculated by using the procedure described in ref. [Sa91]. The adopted scattering field is the analytical approximation (sum of three Yukawa terms) to the self-consistent Dirac-Hartree-Slater field of ref. [SM87a], where parameters for elements with atomic number Z from 1 to 92 are given. This analytical field is accurate enough for simulation purposes and allows the use of the WKB and Born approximations to compute the majority of phase shifts. Only phase shifts of partial waves with low angular momentum need to be computed from the numerical solution of the Dirac radial wave equation [SM91]. This procedure allows the calculation of reliable DCSs for electrons and positrons with kinetic energies from ~ 1 keV up to ~ 20 MeV. Hereafter, the DCSs computed in this way will be referred to as PWA-DCSs.

The mean free path λ between elastic collisions and the single scattering angular distribution $f_1(\chi)$ are given by

$$\lambda = \frac{1}{N\sigma}, \quad f_1(\chi) = \frac{1}{\sigma} \frac{d\sigma(\chi)}{d\Omega} \quad (2.1)$$

where

$$\sigma = 2\pi \int_0^\pi \frac{d\sigma(\chi)}{d\Omega} \sin \chi \, d\chi \quad (2.2)$$

is the total cross section. Notice that the probability of having a polar scattering angle between χ and $\chi+d\chi$ in a single collision is given by $2\pi f_1(\chi) \sin \chi d\chi$. For our purposes, it is useful to write $f_1(\chi)$ in the form of a Legendre series:

$$f_1(\chi) = \sum_{\ell=0}^{\infty} \frac{2\ell+1}{4\pi} F_\ell P_\ell(\cos \chi) \quad (2.3)$$

where P_ℓ are the Legendre polynomials and

$$F_\ell = 2\pi \int_{-1}^1 f_1(\chi) P_\ell(\cos \chi) d(\cos \chi) = \langle P_\ell(\cos \chi) \rangle. \quad (2.4)$$

The quantities

$$G_\ell \equiv 1 - F_\ell \quad (2.5)$$

will be referred to as the transport coefficients. Notice that $F_0 = 1$ and $G_0 = 0$. Moreover, the value of F_ℓ decreases with ℓ due to the faster oscillations of $P_\ell(\cos \chi)$ and, hence, G_ℓ tends to unity when ℓ goes to infinity.

The elastic scattering within a given medium is completely characterized by the transport mean free paths λ_ℓ defined by

$$\lambda_\ell^{-1} \equiv \frac{G_\ell}{\lambda} = N2\pi \int_{-1}^1 [1 - P_\ell(\cos \chi)] \frac{d\sigma(\chi)}{d\Omega} d(\cos \chi). \quad (2.6)$$

In particular, we have

$$\lambda_1^{-1} = \frac{1}{\lambda} \int_{-1}^1 (1 - \cos \chi) \frac{d\sigma(\chi)}{d\Omega} d(\cos \chi) = \frac{1 - \langle \cos \chi \rangle}{\lambda}, \quad (2.7)$$

and

$$\lambda_2^{-1} = \frac{1}{\lambda} \int_{-1}^1 \frac{3}{2} (1 - \cos^2 \chi) \frac{d\sigma(\chi)}{d\Omega} d(\cos \chi) = \frac{3}{2} \frac{1 - \langle \cos^2 \chi \rangle}{\lambda}. \quad (2.8)$$

The quantity “ $1 - \cos \chi$ ” can be adopted as a measure of the angular deflection in single elastic collisions. It is then apparent that the inverse of the first transport mean free path gives the average angular deflection per unit path length. By analogy with the “stopping power”, which is defined as the mean energy loss per unit path length, λ_1^{-1} is sometimes called the “scattering power” [CR83].

Figure 2.1. Elastic mean free path, λ , and first and second transport mean free paths, λ_1 and λ_2 , for electrons scattered by Al and Au atoms as functions of the kinetic energy of the projectile, computed with the PWA-DCSs described in the text. The symbols + and \times indicate partial wave results from ref. [RM75].

The mean free path and the first and second transport mean free paths computed from the PWA-DCSs are given in fig. 2.1 for Al and Au, as representatives of low and high atomic number elements. The values obtained from the total and transport cross sections computed by Riley et al. [RM75] for $E \leq 256$ keV, using a different scattering field, are also included for comparison purposes.

2.2.2 The theories of Goudsmit and Saunderson and Lewis

Assume that an electron starts off from a certain position, which we select as the origin of our reference frame, moving in the direction of the z -axis. Let $f(\mathbf{r}, \hat{\mathbf{d}}; s)$ denote the probability density of finding the electron at the position $\mathbf{r} = (x, y, z)$, moving in the direction given by the unit vector $\hat{\mathbf{d}}$ after having travelled a path length s . The diffusion equation for this problem is [Le50]

$$\frac{\partial f}{\partial s} + \hat{\mathbf{d}} \cdot \nabla f = N \int [f(\mathbf{r}, \hat{\mathbf{d}}'; s) - f(\mathbf{r}, \hat{\mathbf{d}}; s)] \frac{d\sigma(\chi)}{d\Omega} d\Omega \quad (2.9)$$

where $\chi \equiv \cos^{-1}(\hat{\mathbf{d}} \cdot \hat{\mathbf{d}}')$ is the scattering angle corresponding to the angular deflection $\hat{\mathbf{d}}' \rightarrow \hat{\mathbf{d}}$. This equation has to be solved under the boundary condition $f(\mathbf{r}, \hat{\mathbf{d}}; 0) = (1/\pi)\delta(\mathbf{r})\delta(1 - \cos\theta)$, where θ is the polar angle of the direction $\hat{\mathbf{d}}$. By expanding $f(\mathbf{r}, \hat{\mathbf{d}}; s)$ in spherical harmonics, Lewis [Le50] obtained general expressions for the angular distribution, and for the first moments of the spatial distribution after a given path length s . The angular distribution is given by

$$F_{GS}(\theta; s) \equiv \int f(\mathbf{r}, \hat{\mathbf{d}}; s) d\mathbf{r} = \sum_{\ell=0}^{\infty} \frac{2\ell+1}{4\pi} \exp(-s/\lambda_{\ell}) P_{\ell}(\cos\theta) \quad (2.10)$$

where λ_{ℓ} is the ℓ -th transport mean free path defined by eq. (2.6). It is worth noticing that $F_{GS}(\theta; s)d\Omega$ gives the probability of having a final direction in the solid angle element $d\Omega$ around a direction defined by the polar angle θ . Evidently, the distribution (2.10) is symmetrical about the z -axis, i.e. independent of the azimuthal angle of the final direction.

The result given by eq. (2.10) coincides with the distribution obtained by Goudsmit and Saunderson [GS40a] in a more intuitive way, which we sketch here to make clearer its physical meaning. Using the Legendre expansion given by eq. (2.3 and a persistence property of the Legendre polynomials (see ref. [MM65], p. 470), the angular distribution after exactly n collisions is found to be

$$f_n(\theta) = \sum_{\ell=0}^{\infty} \frac{2\ell+1}{4\pi} (F_{\ell})^n P_{\ell}(\cos\theta). \quad (2.11)$$

The probability distribution of the number n of collisions after a path length s is poissonian with mean s/λ , i.e.

$$P(n) = \exp(-s/\lambda) \frac{(s/\lambda)^n}{n!}. \quad (2.12)$$

Therefore, the angular distribution after a path length s can be obtained as

$$F_{GS}(\theta; s) = \sum_{n=0}^{\infty} P(n) f_n(\theta) = \sum_{\ell=0}^{\infty} \frac{2\ell+1}{4\pi} \left[\exp(-s/\lambda) \sum_{n=0}^{\infty} \frac{(s/\lambda)^n}{n!} (F_{\ell})^n \right] P_{\ell}(\cos \theta), \quad (2.13)$$

which coincides with expression (2.10).

From the orthogonality of the Legendre polynomials, it follows that

$$\langle P_{\ell}(\cos \theta) \rangle_{GS} \equiv 2\pi \int_{-1}^1 P_{\ell}(\cos \theta) F_{GS}(\theta; s) d(\cos \theta) = \exp(-s/\lambda_{\ell}). \quad (2.14)$$

In particular we have

$$\langle \cos \theta \rangle_{GS} = \exp(-s/\lambda_1) \quad (2.15)$$

and

$$\langle \cos^2 \theta \rangle_{GS} = \frac{1}{3} [1 + 2 \exp(-s/\lambda_2)]. \quad (2.16)$$

The theory of Lewis [Le50] is superior to that of Goudsmit and Saunderson [GS40a], since it yields also analytical formulae for the first moments of the spatial distribution and the correlation function of z and $\cos \theta$. Neglecting energy loss, the results explicitly given in Lewis' paper simplify to

$$\langle z \rangle \equiv 2\pi \int z f(\mathbf{r}, \hat{\mathbf{d}}, s) d(\cos \theta) d\mathbf{r} = \lambda_1 [1 - \exp(-s/\lambda_1)], \quad (2.17)$$

$$\begin{aligned} \langle x^2 + y^2 \rangle &\equiv 2\pi \int (x^2 + y^2) f(\mathbf{r}, \hat{\mathbf{d}}, s) d(\cos \theta) d\mathbf{r} \\ &= \frac{4}{3} \int_0^s dt \exp(-t/\lambda_1) \int_0^t [1 - \exp(-u/\lambda_2)] \exp(-u/\lambda_1) du, \end{aligned} \quad (2.18)$$

$$\begin{aligned} \langle z \cos \theta \rangle &\equiv 2\pi \int z \cos \theta f(\mathbf{r}, \hat{\mathbf{d}}, s) d(\cos \theta) d\mathbf{r} \\ &= \exp(-s/\lambda_1) \int_0^s [1 + 2 \exp(-t/\lambda_2)] \exp(-t/\lambda_1) dt. \end{aligned} \quad (2.19)$$

The quantities (2.15)–(2.19) are completely determined by the values of λ_1 and λ_2 .

The Goudsmit and Saunderson expansion (2.10) and the results (2.15)–(2.19) are exact. To compute these quantities for a given single scattering DCS, which usually is available only in numerical form, we have to evaluate the transport coefficients G_{ℓ} as

defined in eq. (2.5). Nevertheless, for not too large path lengths, the convergence of the series (2.10) is quite slow [Be63] and a large number of terms are needed. Due to the fast oscillations of the Legendre polynomials, the numerical calculation of the integrals in eq. (2.4) for large ℓ is a very delicate task. The usual practice to avoid this difficulty consists in replacing the exact single scattering distribution $f_1(\chi)$ by suitable analytical approximations [Be63,RM75] that allow the easy evaluation of the transport coefficients G_ℓ by means of recurrence relations. However, we have not been able to find any analytical form able to reproduce the PWA-DCS to an accuracy better than $\sim 5\%$. Therefore, we have computed the transport coefficients from the "exact" PWA-DCS by numerical integration. The integrals

$$G_\ell = 2\pi \int_{-1}^1 f_1(\chi) [1 - P_\ell(\cos \chi)] d(\cos \chi) \quad (2.20)$$

have been calculated by means of a 20-point Gauss formula complemented with an adaptive bipartition procedure that allows the control of integration errors, which have been kept below 0.001 %. In these calculations, the single scattering distribution $f_1(\chi)$ has been handled by means of spline interpolation from tabulated values in a grid dense enough to give a negligible interpolation error. Owing to the length of the calculation, only the first 300 coefficients have been computed and, consequently, we will only consider large enough path lengths s such that the Goudsmit-Saunderson series effectively converges with this number of terms.

Angular distributions of 15.7 MeV electrons transmitted through gold foils are shown in fig. 2.2. Theoretical distributions have been calculated from the Goudsmit-Saunderson theory with our PWA-DCSs. The agreement between our results and the experimental data of Hanson et al. [HL51] is seen to be satisfactory, although the theoretical distributions are slightly narrower. This is to be expected since, in the calculations, we are neglecting inelastic scattering by the atomic electrons, which tends to widen the multiple scattering angular distribution. For a high- Z element such as gold, the relative effect of inelastic collisions is small (of the order of $1/Z$ [Sc63]).

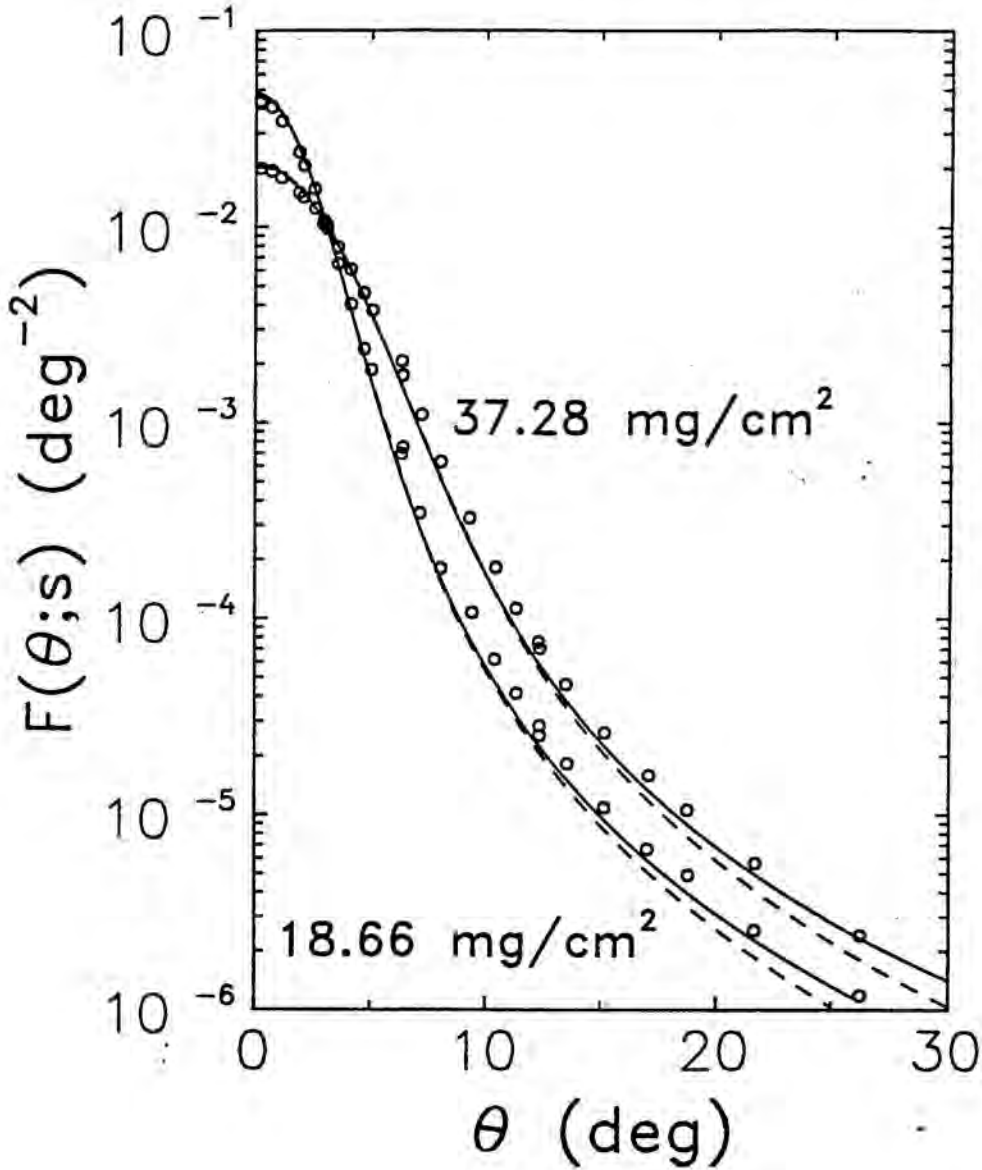


Figure 2.2. Angular distributions of 15.7 MeV electrons transmitted through gold foils of the indicated mass thicknesses. The continuous curves are Goudmit-Saunderson distributions calculated with the PWA-DCS; the dashed curves are the distributions computed from Molière's formula, eq. (2.53), with the parameters given by eqs. (2.59) and (2.60). Circles are experimental results from Hanson et al. [HL51].

2.2.3 The Wentzel model

The simple scattering model due to Wentzel [We27] has been repeatedly used in connection with multiple scattering theory [Le50]. Here we describe it briefly because it will be useful to derive the multiple scattering theory of Molière [Mo48] in a way that puts into evidence the physical content and mathematical accuracy of this theory. Moreover, the analytical simplicity of the Wentzel DCS makes it particularly suited as the basis of fast simulation procedures [LS89,LI90]. In particular, the general simulation algorithm described in section 2.3 can be formulated in a completely analytical way when a DCS of the Wentzel type is adopted (see section 2.4).

The Wentzel approach for describing elastic scattering of particles with charge $Z'e$ ($Z' = -1$ and $+1$ for electrons and positrons, respectively) by atoms of atomic number Z is based on the simplified scattering potential

$$V(r) = \frac{ZZ'e^2}{r} \exp(-r/R) \quad (2.21)$$

where the exponential factor schematizes the effect of screening. The screening radius R may be estimated from the Thomas-Fermi model of the atom, which yields

$$R \simeq 0.885 Z^{-1/3} a_0 \quad (2.22)$$

where a_0 is the Bohr radius. However, it is more expedient to determine R so as to get agreement with more accurate elastic scattering cross sections; this was the procedure adopted by Molière [Mo48] (see below). The differential cross section is obtained from the first Born approximation, which gives

$$\frac{d\sigma^{(W)}(\chi)}{d\Omega} = \frac{(ZZ'e^2)^2}{(p\beta c)^2} \frac{1}{(2A + 1 - \cos \chi)^2}, \quad (2.23)$$

where p is the momentum, β is the velocity, in units of the speed of light c , of the scattered particle and the screening parameter A is given by

$$A \equiv \frac{1}{4} (\hbar/p)^2 R^{-2}. \quad (2.24)$$

The corresponding total cross section is

$$\sigma^{(W)} = \frac{(ZZ'e^2)^2}{(p\beta c)^2} \frac{\pi}{A(1+A)} \quad (2.25)$$

and the single scattering angular distribution is

$$f_1^{(W)}(\chi) = \frac{1}{\pi} \frac{A(1+A)}{(2A + 1 - \cos \chi)^2}. \quad (2.26)$$

The transport coefficients defined in eq. (2.5) are given by—see appendix A—

$$G_\ell^{(W)} = 1 - \ell [Q_{\ell-1}(1+2A) - (1+2A)Q_\ell(1+2A)]. \quad (2.27)$$

The explicit expressions for the first two transport coefficients are

$$G_1^{(W)} = 2A \left[(1+A) \ln \left(\frac{1+A}{A} \right) - 1 \right], \quad (2.28)$$

$$G_2^{(W)} = 6A(1+A) \left[(1+2A) \ln \left(\frac{1+A}{A} \right) - 2 \right]. \quad (2.29)$$

Certainly, the Wentzel DCS, eq. (2.23), with the screening parameter A given by eq. (2.24), is not very accurate and leads to erroneous moments of the multiple scattering distributions. Improved distributions can be obtained by using a screened parameter determined in such a way that the first transport mean free path calculated from the Wentzel DCS,

$$\lambda_1^{(W)} \equiv \frac{1}{N\sigma^{(W)}G_1^{(W)}}, \quad (2.30)$$

coincides with the value λ_1 determined from the PWA-DCS. The value of the screening parameter is obtained as the root of the equation

$$\frac{1}{\lambda_1} = N \frac{(ZZ'e^2)^2}{(p\beta c)^2} 2\pi \left[\ln \left(\frac{1+A}{A} \right) - \frac{1}{1+A} \right], \quad (2.31)$$

which may be easily solved, e.g. by Newton-Raphson's method. The Goudsmit-Saunders distribution for such a corrected Wentzel model, with the proper value of λ_1 , will have its mean equal to that of the "exact" distribution (i.e. the one obtained from the PWA-DCS) but higher order moments may still be in error (cf. eq. (2.16)).

In his original paper, Molière [Mo48], and also Bethe [Be53], used a Wentzel model with an energy-dependent screening parameter that can be expressed as

$$A^{(M)} = \frac{1}{4} (\hbar/p)^2 (0.885 Z^{-1/3} a_0)^{-2} [1.13 + 3.76(\alpha Z/\beta)^2] \quad (2.32)$$

where $\alpha = 1/137$ is the fine-structure constant. This screening parameter agrees with eq. (2.24) except for the last factor, which accounts for corrections to the Born approximation. Molière derived eq. (2.32) by fitting the DCS obtained from the eikonal approximation with the Thomas-Fermi atomic field.

The eikonal approximation leads to a DCS that is very accurate for high energies

and small scattering angles [ZO64]¹ and reduces to the Rutherford DCS

$$\frac{d\sigma^{(R)}(\chi)}{d\Omega} = \frac{(ZZ'e^2)^2}{(p\beta c)^2} \frac{1}{(1 - \cos \chi)^2}, \quad (2.33)$$

for large scattering angles [Mo47] (irrespective of the adopted screening model). As the Wentzel DCS departs from the Rutherford DCS only for small χ , it is clear that, by using a convenient value of the screening parameter, we can make the Wentzel DCS almost identical with the eikonal DCS for all angles. Thus, the “optimum” screening parameter can be determined unambiguously by solving eq. (2.31) with the first transport mean free path computed from the eikonal DCS. This procedure is essentially equivalent to the one followed by Molière to derive his “screening angle”. Therefore, the screening parameter determined in this way should not differ significantly from the value given by eq. (2.32). Hereafter, the Wentzel model with Molière’s screening parameter will be referred to as the WM model.

The adequacy of the WM model to describe the actual scattering process is thus determined by the combined effect of two different approximations, namely 1) the use of the Thomas-Fermi atomic field and 2) the eikonal approximation. The statistical Thomas-Fermi field gives a reasonably good representation of the actual scattering field except for the elements of low atomic number. The deficiencies of the statistical model of the atom can be largely avoided by using a more realistic self-consistent field, for instance the analytical Dirac-Hartree-Fock-Slater field [SM87a] adopted in the calculation of our PWA-DCSs. In any case, the eikonal DCS for such a realistic field could still be closely approximated by the Wentzel DCS with a convenient value of the screening parameter. The essential limitations of the Wentzel model come from the Rutherford-like behaviour of the DCS for large scattering angles, which is correct only when spin and finite nuclear size effects are negligible. However, it happens that both types of effects modify the single scattering cross section for large angles [MM65,FM92] with the result that the eikonal DCS, obtained from a realistic scattering field, may differ considerably from the actual DCS at large angles. As a consequence, the WM model is only adequate for describing small-angle elastic collisions of high energy electrons. The practical consequences of the erroneous behaviour of the WM-DCS at large angles will be analyzed below.

¹The accuracy of the eikonal DCS for $\chi = 0$ and energies above ~ 100 keV is surprisingly good. We have found that the relative differences between the DCSs for forward scattering calculated from the eikonal approximation and from the partial wave method, with the same screened field, are less than one tenth percent

As regards Monte Carlo simulation it is important to make sure that the simulated distributions have at least the correct values of the quantities given by eqs. (2.15)–(2.19). This can be accomplished by simply using an approximate analytical DCS with the proper values of λ_1 and λ_2 , i.e. those obtained from the PWA-DCS. An obvious candidate is the Wentzel DCS, which now we write in the form

$$\frac{d\sigma^{(a)}(\chi)}{d\Omega} = \sigma^{(W)} \frac{1}{\pi} \frac{A(1+A)}{(2A+1-\cos\chi)^2}. \quad (2.34)$$

Up to this point, we have only considered the possibility of varying the value of the screening parameter since we intended to keep the (incorrect) Rutherford large angle behaviour of the Wentzel DCS. For our present purposes, we can consider A and $\sigma^{(W)}$ as adjustable parameters and determine them so that

$$\frac{1}{\lambda_1} = \frac{G_1^{(W)}}{\lambda^{(W)}} \quad \text{and} \quad \frac{1}{\lambda_2} = \frac{G_2^{(W)}}{\lambda^{(W)}} \quad (2.35)$$

where $\lambda^{(W)} \equiv 1/(N\sigma^{(W)})$. The screening parameter A is given by the root of the transcendent eq.

$$\frac{\lambda_2}{\lambda_1} = \left[(1+A) \ln \left(\frac{1+A}{A} \right) - 1 \right] \left\{ 3(1+A) \left[(1+2A) \ln \left(\frac{1+A}{A} \right) - 2 \right] \right\}^{-1} \quad (2.36)$$

and $\lambda^{(W)} = \lambda_1 G_1^{(W)}$. This Wentzel model (hereafter to be referred to as the W2 model) leads to a DCS which has the same “average” value as the PWA-DCS in the interval of angles that effectively contribute to λ_1 and λ_2 . As the integrands in eqs. (2.7) and (2.8) vanish for $\chi = 0$, the Wentzel DCS and the PWA-DCS may differ considerably for very small angles, but these differences only affect the shape of the multiple scattering distributions for short path lengths (see below). Significant differences between the Wentzel DCS and the PWA-DCS appear also at large scattering angles, but there the DCSs take values that, for high energy electrons, are exceedingly small.

In practice, when condensed Monte Carlo simulation is needed, i.e. for high-energy electrons, the screening parameter A is small. In this case, the evaluation of the transport coefficients (2.27) can be simplified by using their limiting form given in appendix A (eq. (A.10))

$$G_\ell^{(W)} = \ell(\ell+1)A \left[\ln \left(\frac{1+A}{A} \right) - 2\Phi(\ell) + 1 \right] + \mathcal{O}(\ell^4 A^2) \quad (2.37)$$

where

$$\Phi(\ell) \equiv \sum_{m=1}^{\ell} \frac{1}{m}. \quad (2.38)$$

Expression (2.37) was first derived by Goudsmit and Saunderson [GS40a], and rederived by Bethe [Be53], using tedious integration methods.

2.2.4 The Molière theory

The Molière theory [Mo48], as reformulated by Bethe [Be53], is based on the assumption of a single scattering law that has the form (2.23) for small scattering angles and goes over the Rutherford law, ec. (2.33) for large scattering angles. Indeed, the Wentzel cross section, eq. (2.23) fulfills this last assumption and, hence, it will lead to the Molière multiple scattering distribution if the screening parameter $A^{(M)}$ given by eq. (2.32) is adopted.

Assuming temporarily that a single scattering DCS of the form (34) is a good approximation, we will derive the Molière multiple scattering distribution on the basis of the results of the previous subsection. Our derivation follows the same steps as that of Bethe [Be53], but it is considerably shorter and emphasizes the fact that the Molière theory is essentially the multiple scattering theory of the Wentzel model. A single scattering DCS having a form different from the Wentzel cross section will lead to multiple scattering distributions that differ from the Molière one (see e.g. [NS59]).

We start from the approximate transport coefficients given in eq. (2.37). First we replace $\Phi(\ell)$ by the approximation [Mo48]

$$\Phi(\ell) = \gamma + \ln(\ell + 1/2) + \frac{1}{24(\ell + 1/2)^2} \quad (2.39)$$

where $\gamma = 0.5772$ is Euler's constant, and keep only the first two terms, thus obtaining the Molière approximation for the multiple scattering coefficients:

$$G_\ell^{(M)} = \ell(\ell + 1)A \left[\ln \left(\frac{1+A}{A} \right) + 1 - 2\gamma - 2\ln(\ell + 1/2) \right]. \quad (2.40)$$

In particular we have

$$G_1^{(M)} = 2A \left[\ln \left(\frac{1+A}{A} \right) - 0.965 \right], \quad (2.41)$$

$$G_2^{(M)} = 6A \left[\ln \left(\frac{1+A}{A} \right) - 1.987 \right]. \quad (2.42)$$

Comparing these results with eqs. (28) and (2.29), we see that the approximations introduced up to this point are not serious, provided $A \ll 1$. However, from eq. (2.37) it is clear that the approximation $G_\ell^{(M)}$ will fail for ℓ values such that $\ell^2 A \sim 1$. Actually, when ℓ increases from 0 to ∞ , the right hand side of eq. (2.40) first increases from 0 up to a maximum value $\sim (1+A) \exp(-2\gamma)$, which is reached when $\ell = \ell_{max} \sim (1+A^{-1})^{1/2} \exp(-\gamma)$, and for larger values of ℓ it decreases monotonously and eventually

becomes negative. As the "exact" transport coefficients $G_\ell^{(W)}$, eq. (2.27), tend to unity when ℓ goes to ∞ , it is clear that we should limit the use of the approximation given by eq. (2.40) to path lengths s that are large enough to make sure that the Goudsmit-Saunderson series, eq. (2.10), for the Wentzel model, converges with less than ℓ_{max} terms.

The remaining task is to avoid the summation of the Goudsmit-Saunderson series, eq. (2.10). This is accomplished by introducing the following approximation, due to Molière [Mo48],

$$P_\ell(\cos \theta) \simeq \left(\frac{\theta}{\sin \theta} \right)^{1/2} J_0([\ell + 1/2]\theta) \quad (2.43)$$

and replacing the summation in the Goudsmit-Saunderson series by an integral over ℓ . Assuming $s \gg \lambda$, we have

$$\begin{aligned} F_M(\theta; s) &= \frac{1}{2\pi} \left(\frac{\theta}{\sin \theta} \right)^{1/2} \int_0^\infty (\ell + 1/2) \exp[-(s/\lambda^{(W)})G_\ell^{(M)}] J_0([\ell + 1/2]\theta) d\ell \\ &= \frac{1}{2\pi} \left(\frac{\theta}{\sin \theta} \right)^{1/2} \int_0^\infty y \exp[-g(y)] J_0(y\theta) dy \end{aligned} \quad (2.44)$$

where $y = \ell + 1/2$ and

$$g(y) \equiv \frac{s}{\lambda^{(W)}} G_\ell^{(M)} = \frac{s}{\lambda^{(W)}} (y^2 - 1/4) A \left[\ln \left(\frac{1+A}{A} \right) + 1 - 2\gamma - 2 \ln y \right]. \quad (2.45)$$

Introducing the parameters

$$\chi_c^2 \equiv \frac{s}{\lambda^{(W)}} 4A, \quad b \equiv \ln \left[\frac{s}{\lambda^{(W)}} (1+A) \right] + 1 - 2\gamma \quad (2.46)$$

we can write

$$g(y) = \frac{1}{4} \chi_c^2 (y^2 - 1/4) \left[b - \ln \left(\frac{1}{4} \chi_c^2 y^2 \right) \right], \quad (2.47)$$

and, changing to the variable $u = \chi_c y$,

$$\begin{aligned} F_M(\theta; s) &= \frac{1}{2\pi} \left(\frac{\theta}{\sin \theta} \right)^{1/2} \frac{1}{\chi_c^2} \\ &\quad \times \int_0^\infty u \exp \left[- \left(\frac{u^2}{4} - \frac{\chi_c^2}{16} \right) (b - \ln(u^2/4)) \right] J_0(u\theta/\chi_c) du. \end{aligned} \quad (2.48)$$

To facilitate the evaluation of this integral, Molière set

$$b = B - \ln B, \quad \omega = uB^{1/2} = \chi_c B^{1/2} y \quad (2.49)$$

so that he could write

$$F_M(\theta; s) = \frac{1}{2\pi} \left(\frac{\theta}{\sin \theta} \right)^{1/2} \frac{1}{\chi_c^2 B} \int_0^\infty \omega \exp \left[\frac{\chi_c^2}{16} (B - \ln(\omega^2/4)) \right] \\ \times \exp \left[\frac{\omega^2}{4B} \ln(\omega^2/4) - \omega^2/4 \right] J_0 \left(\frac{\omega \theta}{\chi_c \sqrt{B}} \right) d\omega. \quad (2.50)$$

Now, we note that $e^{B/\lambda} = e^b \sim s/\lambda^{(W)}$, the average number of collisions in the path length s . In practice B takes values much larger unity (e.g. $B \approx 3.6$ for $s/\lambda^{(W)} = 10$, which is a pretty small path length) and hence, for the values of ω that effectively contribute to the integral in eq. (2.50), we can write

$$\exp \left[\frac{\omega^2}{4B} \ln(\omega^2/4) \right] \simeq 1 + \frac{1}{B} \frac{\omega^2}{4} \ln(\omega^2/4) + \frac{1}{2!} \frac{1}{B^2} \left(\frac{\omega^2}{4} \ln(\omega^2/4) \right)^2 \quad (2.51)$$

and

$$\exp \left[\frac{\chi_c^2}{16} (B - \ln(\omega^2/4)) \right] \simeq \exp(\chi_c^2 B/16). \quad (2.52)$$

With all this, we obtain

$$F_M(\theta; s) = \frac{1}{2\pi} \left(\frac{\theta}{\sin \theta} \right)^{1/2} \frac{\exp(\chi_c^2 B/16)}{\chi_c^2 B} \left[f^{(0)}(\vartheta) + \frac{1}{B} f^{(1)}(\vartheta) + \frac{1}{B^2} f^{(2)}(\vartheta) \right] \quad (2.53)$$

where

$$\vartheta \equiv \frac{\theta}{\chi_c \sqrt{B}} \quad (2.54)$$

and

$$f^{(n)}(\vartheta) \equiv \frac{1}{n!} \int_0^\infty \omega \exp(-\omega^2/4) \left(\frac{\omega^2}{4} \ln(\omega^2/4) \right)^n J_0(\vartheta \omega) d\omega. \quad (2.55)$$

This is exactly the same distribution obtained by Molière [Mo48] and Bethe [Be53]. The first term in the series (2.53) is the gaussian distribution

$$f^{(0)}(\vartheta) = 2 \exp(-\vartheta^2). \quad (2.56)$$

The functions $f^{(1)}(\vartheta)$ and $f^{(2)}(\vartheta)$ have been tabulated by Bethe [Be53]. In the numerical calculations reported below, these functions have been calculated by cubic spline interpolation from Bethe's tables [Be53] for $\vartheta < 6$. For $\vartheta \geq 6$, we use the expressions

$$f^{(1)}(\vartheta) \simeq 2\vartheta^{-4} (1 - 5\vartheta^{-2})^{-4/5} \quad (2.57)$$

$$f^{(2)}(\vartheta) \simeq 16\vartheta^{-6} (\ln \vartheta + \gamma - 3/2) (1 + 9\vartheta^{-2}) - 38\vartheta^{-8}, \quad (2.58)$$

which are accurate to within a few tenths of a percent.

With the screening parameter given by eq. (2.32), and assuming it to be much less than unity, we find

$$\chi_c^2 = sN4\pi \frac{(ZZ'e^2)^2}{(p\beta c)^2}, \quad (2.59)$$

$$b = \ln \left(sN\pi \frac{(ZZ'e^2)^2}{(p\beta c)^2 A^{(M)}} \right) + 1 - 2\gamma, \quad (2.60)$$

which coincide exactly with the parameters used by Molière in his original paper [Mo48]. Therefore, the original form of the Molière theory is nothing more than an analytical approximation to the exact Goudsmit-Saunderson distribution for the WM model.

The mathematical approximations introduced in the derivation of the Molière distribution, eq. (2.53), put certain limits on its range of validity. Firstly, the limiting form of the transport coefficients given by eq. (2.40) is valid only when the screening parameter A is small. This limits the applicability of the theory to high energies, for which the first transport mean free path is much larger than the mean free path. Secondly, we must have $b > 1$ (otherwise, the parameter B , see eq. (2.49), is not defined). This means that the path length s must be larger than about $4\lambda^{(W)}$ (see eq. (2.46)), i.e. the scattering must be at least plural. Actually, a restriction of this sort was to be expected from the very beginning since, when $s \sim \lambda^{(W)}$, the Goudsmit-Saunderson series is slowly convergent and contributions from terms with $\ell > \ell_{max}$ (see the discussion after eq. (2.42)) may not be negligible. As $G_2^{(M)}$ is not adequate for these high order terms, the whole theory fails when $s \sim \lambda^{(W)}$. Finally, the approximation given by eq. (2.43) is very accurate for small angles, it remains good for intermediate angles and breaks down for values of θ near 180 degrees where the factor $(\theta/\sin\theta)^{1/2}$ diverges. This divergence is not important when $s \ll \lambda_1^{(W)}$, since then the angular distribution is strongly peaked in the forward direction and the only effect of the divergence is a very narrow peak in the backward direction with a negligible area. Undesirable effects of this divergence become prominent when $s \simeq \lambda_1^{(W)}$. Under these circumstances, the distribution (2.53) shows a conspicuous peak in the backward direction and therefore differs appreciably from the "exact" angular distribution, which tends to the isotropic distribution when $s \gg \lambda_1$. To avoid this anomalous behaviour, we should limit to path lengths such that the gaussian part (2.56) of the Molière distribution has a width less than 1 radian [Be53] or, equivalently, such that $\chi_c^2 B \leq 1$. In conclusion, the Molière distribution eq. (2.53) gives a good approximation to the Goudsmit-Saunderson distri-

bution for the Wentzel model when the conditions

$$\lambda^{(W)} \ll \lambda_1^{(W)} \quad \text{and} \quad 4\lambda^{(W)} < s < \lambda_1^{(W)} \quad (2.61)$$

are simultaneously fulfilled. This is exemplified in fig. 2.3 where the Goudsmit-Saunders distributions for 1 MeV electrons in aluminium ($Z=13$) computed from the WM-DCS are compared with the distributions obtained from Molière's formula, eq. (2.53), for four different path lengths.

Bethe [Be53] used the angular distributions of 15.7 MeV electrons in gold measured by Hanson et al. [HL51] to illustrate the reliability of the original Molière theory (using the screening parameter given by eq. (2.32)). He found good agreement between Molière's and experimental distributions (see fig. 2.2). In spite of this agreement, the conclusion that Molière's theory provides a reliable description of multiple scattering of 15.7 MeV electrons in gold is by no means legitimate. Taking into account that the distributions measured by Hanson et al. are quite narrow, the only allowed conclusion is that the WM model gives a good description of small-angle scattering or, to put it into a more basic form, that the Thomas-Fermi field (from which the Molière screening parameter was derived) does not deviate very much from the actual field of a gold atom. Actually, there is no reason to expect such a good agreement for other elements and, more important, even when the Thomas-Fermi field is reasonably good, sizeable differences between the WM- and PWA-DCS at intermediate and large scattering angles are to be expected. Owing to these differences, the first and second transport mean free paths, λ_1 and λ_2 , obtained from the WM model and from the PWA-DCS will not coincide. These quantities are given in table 2.1 for different elements and energies. Indeed, the relative differences between first and second transport free paths for 15.7 MeV electrons in gold computed from the MW-DCS and from the PWA-DCS are 14 and 11 percent respectively.

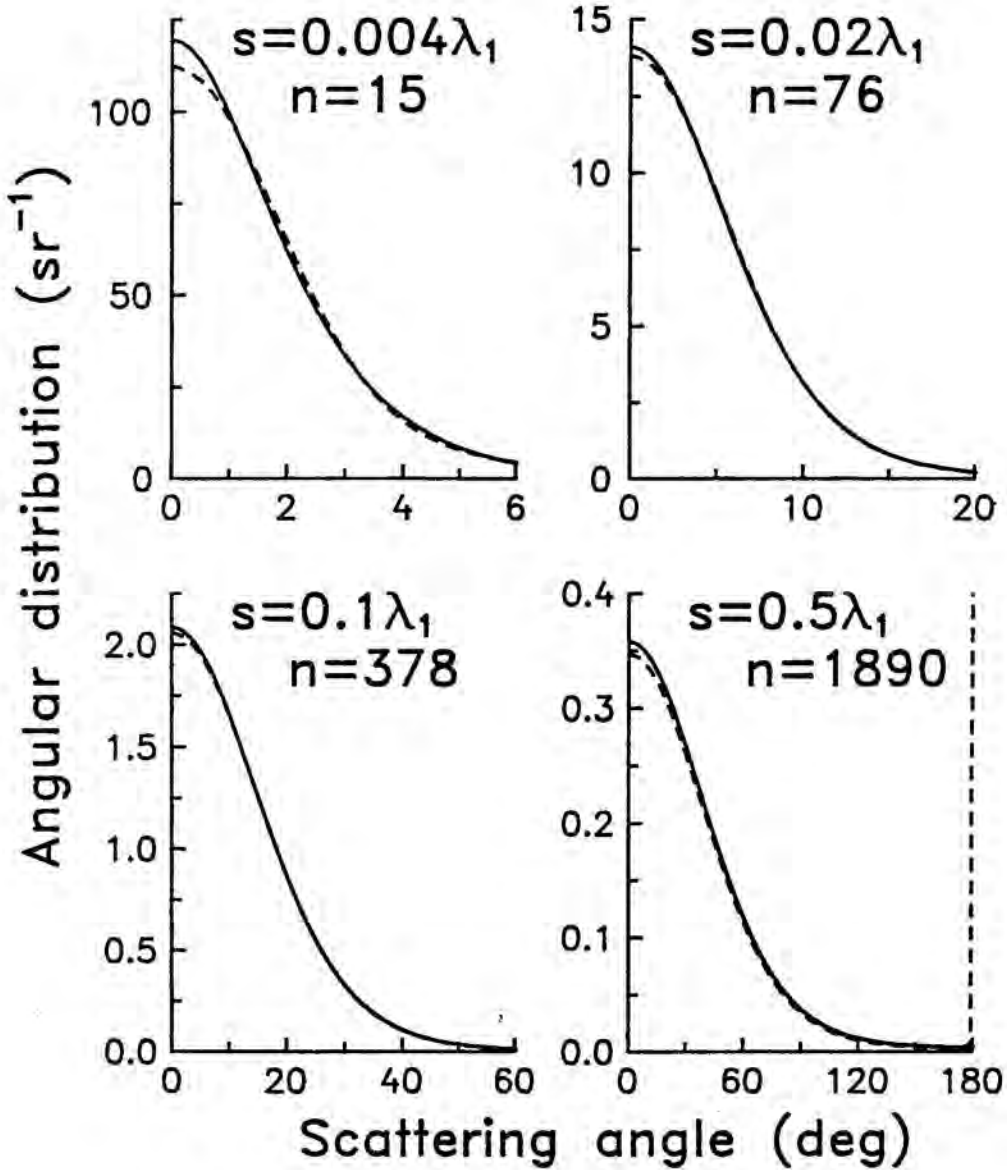


Figure 2.3. Multiple scattering distributions of 1 MeV electrons after travelling a length s (expressed in units of the first transport mean free path $\lambda_1^{(M)}$ given in table 2.1) in Al. The continuous curves are Goudsmit-Saunderson distributions for the WM-DCS ($A = A^{(W)} = 1.4 \times 10^{-5}$). The dashed curves represent the Molière distribution, eq. (2.53), for this WM-DCS, i.e. with the parameters given by eqs. (2.59) and (2.60). The average number $n = s/\lambda^{(W)}$ of collisions in each case is also indicated.

Let us analyze the reliability of the Molière theory when used as the basis of a Monte Carlo simulation code. The length of the simulated tracks may be very large (of the order of the Bethe range) so that the angular distribution at the end of the track can be quite broad. As seen before, the Goudsmit-Saunderson distribution for electrons in gold computed from our PWA-DCS is in good agreement with the experimental results of Hanson et al. and, therefore, we expect that it will be reliable also for larger path lengths and other energies. Of course, for larger path lengths, energy losses should be taken into account to get realistic calculation results. For the sake of simplicity, however, we will continue neglecting energy loss. This is justified here for we are going to consider only differences between the theoretical distributions of Goudsmit-Saunderson and Molière. Moreover, from the values in table 2.1 we see that the relative difference between the transport mean free paths obtained from the WM model and from the PWA-DCS varies very slowly with the kinetic energy and, hence, our conclusions would remain unaltered when considering that electrons slow down along their track.

Table 2.1. First transport mean free paths and screening parameters for different elements and energies. Numbers in parentheses are powers of ten that multiply the quoted values, e.g. $9.92(3) \equiv 9.92 \times 10^3$. λ_1 is the first transport mean free path computed from the PWA-DCSs. The screening parameter A of a Wentzel model which yields this first transport mean free path is given in the fifth column. The Wentzel model with Molière's screening parameter $A^{(M)}$, as given by eq. (2.33), yields the values $\lambda_1^{(M)}$ given in the fourth column, which differ markedly from λ_1 .

Element, Z	E (MeV)	λ_1	$\lambda_1^{(M)}$	λ_2	$\lambda_2^{(M)}$
Al, 13	0.1	9.92(3)	9.51(3)	3.80(3)	3.68(3)
	1.0	3.90(5)	3.59(5)	1.39(5)	1.33(5)
	10.0	1.69(7)	1.58(7)	5.88(6)	5.66(6)
Ag, 47	0.1	3.32(3)	3.74(3)	1.35(3)	1.51(3)
	1.0	1.18(5)	1.24(5)	4.36(4)	4.66(4)
	10.0	5.10(6)	5.26(6)	1.81(6)	1.90(6)
Au, 79	0.1	2.32(3)	2.97(3)	1.05(3)	1.25(3)
	1.0	7.24(4)	8.80(4)	2.83(4)	3.34(4)
	10.0	3.13(6)	3.61(6)	1.16(6)	1.31(6)
	15.7	7.04(6)	8.04(6)	2.59(6)	2.90(6)

The Goudsmit-Saunderson distributions obtained from the PWA-DCS and from the WM and W2 models for 15.7 MeV electrons in gold are shown in fig. 2.4 for four different path lengths. The distributions corresponding to the WM and W2 models do not differ appreciably from the distributions obtained using the Molière formula, eq. (2.53), with the adequate parameters; we use the Goudsmit-Saunderson distributions so as not to mask the sought differences with unnecessary mathematical approximations. It is clear from this comparison that the WM model gives quite accurate distributions for short path lengths, such that the distribution is so narrow that the erroneous Rutherford tail is not seen on a linear scale. However, when the path length is large enough for the probability of scattering through large angles to become appreciable, the inaccuracies of the WM model become apparent in the simulated distribution. In particular we see that the WM model gives too narrow multiple scattering distributions. This is so because the first transport mean free path of the WM model is larger than that of the PWA-DCS (see table 2.1), i.e. the WM model gives a multiple scattering effect that is too weak. We thus arrive at the conclusion that the Molière theory with the original parameters, eqs. (2.59) and (2.60), although apparently accurate for short path lengths (if we do not look at the distribution tail carefully), is not adequate for path lengths of the order of $0.1\lambda_1$ and larger (for which the angular distribution has a half width larger than ~ 20 deg). This has undesirable consequences on practical simulation since, although Monte Carlo algorithms based on Molière's theory use short step lengths (so that *small-angle* deflections at each step are simulated quite accurately), the accuracy of the simulated angular distribution progressively deteriorates after each step. Indeed, anomalies in the results of Monte Carlo simulations based on the Molière theory have already been pointed out by other researches. In particular this theory seems to lead to a depth-dose function for parallel electron beams that is at variance with experimental measurements [AM91].

As regards Monte Carlo simulation, instead of using the WM model, it may be more convenient to use the W2 model, which leads to the proper values of the first and second transport mean free paths (and hence of the quantities given by eqs. (2.15)–(2.19). The W2 model does not give very accurate distributions for short path lengths (although their first momenta do have the correct values), but the accuracy of the multiple scattering distributions obtained from this model improves rapidly when the path length increases (see fig. 2.4). Actually, for path lengths of the order of $0.1\lambda_1$ the Goudsmit-Saunderson multiple scattering distributions obtained from the W2 model and from

the PWA-DCS do not differ appreciably. Under many practical circumstances, e.g. in radiotherapy oriented applications, electron tracks are simulated until the electron has lost a large fraction of its initial kinetic energy. This usually implies that the average angular deflection at the end of the track is quite large, and hence the W2 model may yield very accurate simulation results.

the PWA-DCS do not differ appreciably. Under many practical circumstances, e.g. in radiotherapy oriented applications, electron tracks are simulated until the electron has lost a large fraction of its initial kinetic energy. This usually implies that the average angular deflection at the end of the track is quite large, and hence the W2 model may yield very accurate simulation results.

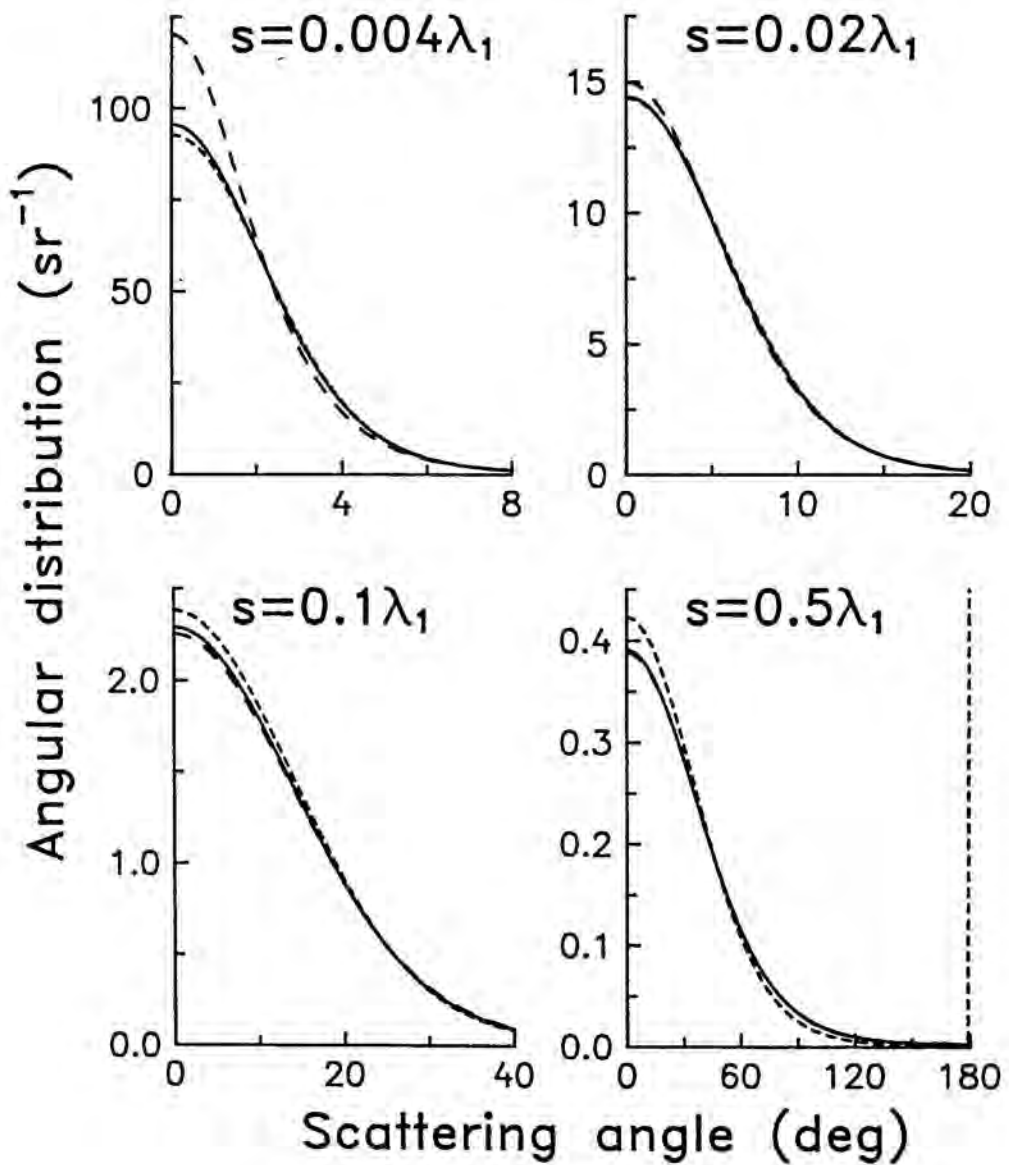


Figure 2.4. Goudsmit-Saunderson distributions of 15.7 MeV electrons after travelling different lengths in gold computed from the PWA-DCS (continuous curves), the WM-DCS (short-dashed curves) and from the W2-DCS (long-dashed curves).

2.3 A new simulation algorithm

The reliability of condensed Monte Carlo simulations based on a given multiple scattering theory is difficult to analyze since it is determined by two different factors, namely, 1) the adequacy of the adopted multiple scattering approach to describe the angular distribution after a given path length and 2) the accuracy of the algorithm used to generate the spatial displacement in each step. It is evident that, to get optimum simulation results we should use the Goudsmit-Saunderson angular distribution, with the most accurate single scattering DCS available, and, at the same time, make sure that the spatial displacements are correctly simulated. The main difficulty of using the Goudsmit-Saunderson theory is the need of storing the transport mean free paths, eq. (2.6), as functions of the energy and to sum the Legendre series, eq. (2.10), for each step length. This represents a great deal of numerical work when the step length is small. The only way of reducing the numerical effort is to use larger step lengths but this will lead to larger uncertainties in the spatial displacements. For the sake of simplicity, the actual DCS could be replaced by the simpler W2-DCS with a loss of accuracy that is tolerable for most practical purposes. To our knowledge, the only algorithm that seems to handle the spatial displacements in a stable way (i.e. independently of the step length) is the PRESTA algorithm of Bielajew and Rogers [BR86], which is based on the original Molière theory, i.e. on the WM model. It is worth pointing out that the PRESTA algorithm, apart from containing some mathematical approximations, neglects the straggling of the spatial displacement. Furthermore, its implementation in a form suitable for rapid calculation is not trivial at all.

The most reliable simulation method is detailed simulation (see e.g. refs. [RK76] and [MM90]) using the best DCSs available. In detailed simulation, each track is generated as a succession of connected straight segments or free-flights. Each free-flight ends with a collision where the particle changes its direction of flight. The change of direction is determined by the polar deflection $\cos \chi$, which is sampled from the single scattering distribution, eq. (2.3), and the azimuthal scattering angle φ , which is sampled uniformly in the interval $(0, 2\pi)$. The length t of the free-flight to the next collision is sampled from the exponential distribution

$$p(t) = \lambda^{-1} \exp(-t/\lambda), \quad (2.62)$$

which gives the probability that the particle travels a length t before colliding. The tracks so simulated can be considered as real electron tracks. The simulated spatial

displacements are “exact”, i.e. the resulting spatial distributions coincide with the ones that would be obtained from a rigorous solution of the transport equation (2.9) with the same DCSs. Moreover, in detailed simulations, the crossing of boundaries poses no particular problems [SM86].

Detailed simulation is feasible only when the mean number of collisions per track is small (say, a few hundreds at most). This occurs for electrons with low energy and for thin geometries. The number of collisions experienced by an electron before being effectively stopped increases with its initial energy, so that detailed simulation becomes unfeasible at high energies. Up to date, the only methods to simulate high energy electron transport are condensed simulation algorithms. At the energies where these algorithms are required, $\lambda_1 \gg \lambda$ so that the average angular deflection in each collision is small. In other words, the great majority of elastic collisions are “soft” collisions with very small deflections. We will take advantage of this feature to devise more accurate simulation procedures for multiple elastic scattering.

We shall consider mixed simulation procedures in which “hard” collisions, with scattering angle χ larger than a given value χ_S , are individually simulated and soft collisions (with $\chi < \chi_S$) are described by means of a multiple scattering approach. It is clear that, by selecting a conveniently large value of the cutoff angle χ_S , the number of hard collisions per electron track can be made small enough to allow their detailed simulation. As the fluctuations in the spatial displacement after a path length s are mainly due to hard collisions, this mixed procedure will yield spatial distributions that are considerably more accurate than those from a conventional condensed simulation. A similar strategy is of common use for simulating energy-loss events (see e.g. refs. [Be63] and [NH85]); it is difficult to understand why this kind of approach is not routinely applied also to elastic scattering. The only attempt in this direction was the work of Reimer and Krefting [RK76] who used detailed simulation for collisions with scattering angles larger than 10 deg. Soft collisions (with $\chi < 10$ deg) between two consecutive hard collisions were assumed to produce only a change in the direction of movement, which was evaluated according to eq. (2.15) thus neglecting the straggling of the angle deflection produced by soft collisions. Moreover, differences between the actual displacement and the longitudinal displacement in the absence of soft collisions were disregarded. Using accurate PWA-DCSs, this approach was shown to work reasonably well for electrons with kinetic energy up to ~ 100 keV [RK76]. For higher energies, however, collisions with scattering angles larger than 10 deg occur very sel-

dom, with the result that the Reimer-Krefting algorithm must be refined to be useful.

The mixed simulation algorithm proposed here is determined by the value of the mean free path between hard collisions, which is given by

$$\frac{1}{\lambda^{(h)}} = N2\pi \int_{\chi_s}^{\pi} \frac{d\sigma(\chi)}{d\Omega} \sin \chi d\chi. \quad (2.63)$$

The inverse transport mean free paths λ_ℓ^{-1} , see eq. (2.6), for the actual scattering process can be splitted into the contributions from hard and soft collisions, i.e.

$$\frac{1}{\lambda_\ell} = \frac{1}{\lambda_\ell^{(s)}} + \frac{1}{\lambda_\ell^{(h)}} \quad (2.64)$$

where

$$\frac{1}{\lambda_\ell^{(s)}} = N2\pi \int_0^{\chi_s} [1 - P_\ell(\cos \chi)] \frac{d\sigma(\chi)}{d\Omega} \sin \chi d\chi \quad (2.65a)$$

and

$$\frac{1}{\lambda_\ell^{(h)}} = N2\pi \int_{\chi_s}^{\pi} [1 - P_\ell(\cos \chi)] \frac{d\sigma(\chi)}{d\Omega} \sin \chi d\chi. \quad (2.65b)$$

To set the value of the mean free path between hard collisions we use the following prescription

$$\lambda^{(h)} = \max \{ \lambda, C_s \lambda_1 \} \quad (2.66)$$

where C_s is a small constant, say less than ~ 0.05 , which has been previously selected. For increasing energies, λ attains a constant value and λ_1 increases steadily (see fig. 2.1) so that the recipe (2.66) gives a mean free path for hard collisions that increases with the energy, i.e. hard collisions are more spaced when the scattering effect is weaker. The formula (2.66) also makes sure that $\lambda^{(h)}$ will reduce to the actual mean free path λ for low energies. In this case, soft collisions cease to occur and our mixed simulation becomes purely detailed. It is worth noticing that, when mixed simulation is effective (i.e. when $\lambda^{(h)} > \lambda$), the mean angular deflection in a path length $\lambda^{(h)}$ is—see eq. (2.15)—

$$1 - \langle \cos \theta \rangle = 1 - \exp(-\lambda^{(h)}/\lambda_1) \simeq C_s. \quad (2.67)$$

Hence, when using the prescription (2.66), the average angular deflection due to a single hard collision and to the soft collisions in the previous “step” (i.e. in the path length after the previous hard collision) equals C_s .

The probability distribution function of the step length t between two successive hard collisions is

$$p(t) = \frac{1}{\lambda^{(h)}} \exp(-t/\lambda^{(h)}). \quad (2.68)$$

The inverse transform method [Ru81] leads to the well-known sampling formula

$$t = -\lambda^{(h)} \ln(\xi). \quad (2.69)$$

Here, and in what follows, ξ stands for a pseudo-random number uniformly distributed in the interval $(0,1)$. The probability distribution of the polar deflection $\cos \chi$ in single hard collisions is

$$p^{(h)}(\chi) = c_n \frac{d\sigma(\chi)}{d\Omega} \sin \chi \Theta(\chi - \chi_s) \quad (2.70)$$

where c_n is the normalization constant and $\Theta(x)$ stands for the step function ($=0$ if $x < 0$ and $=1$ if $x > 0$). Random values of $\cos \chi$ from this probability distribution can be generated numerically by using the inverse transform method [Ru81].

Let us assume that an electron starts off from the origin of coordinates moving in the direction of the z -axis and undergoes a hard collision after travelling a path length (step) t . The exact angular distribution produced by the soft collisions along this step is

$$F_{GS}^{(s)}(\theta; t) = \sum_{\ell=0}^{\infty} \frac{2\ell+1}{4\pi} \exp(-t/\lambda_{\ell}^{(s)}) P_{\ell}(\cos \theta). \quad (2.71)$$

The average longitudinal displacement at the end of the step is given by (see eq. (17))

$$\langle z \rangle^{(s)} = \lambda_1^{(s)} \left[1 - \exp(-t/\lambda_1^{(s)}) \right] = t \left[1 - \frac{1}{2} \left(\frac{t}{\lambda_1^{(s)}} \right) + \frac{1}{6} \left(\frac{t}{\lambda_1^{(s)}} \right)^2 - \dots \right] \quad (2.72)$$

where $\lambda_1^{(s)}$ is the first transport mean free path for soft collisions, which is larger than λ_1 . As the mean free path between hard collisions is much less than $\lambda_1^{(s)}$, the value $t/\lambda_1^{(s)}$ is, on average, much less than unity. Owing to this fact, the global effect of the soft collisions in the step, i.e. the change in direction of movement *and* the spatial displacement, can be simulated by using the following simple algorithm (see fig. 2.5)

1. The electron first moves a random distance τ , which is sampled uniformly in the interval $(0,t)$, in the initial direction.
2. Then a single artificial soft collision takes place. The electron changes its direction of movement according to the multiple scattering distribution $F_{GS}^{(s)}(\theta; t)$.
3. Finally, it moves a distance $t - \tau$ in the new direction.

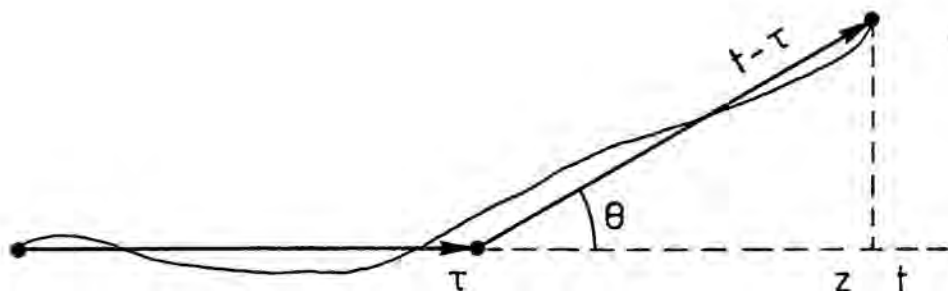


Figure 2.5. Simulation of the global effect of soft collisions between two consecutive hard collisions.

Obviously, this algorithm leads to the exact angular distribution at the end of the step. Moreover, the average longitudinal displacement at the end of the simulated step is

$$\langle z \rangle_{sim}^{(s)} = \frac{t}{2} + \frac{t}{2} \langle \cos \theta \rangle^{(s)} = t \left[1 - \frac{1}{2} \left(\frac{t}{\lambda_1^{(s)}} \right) + \frac{1}{4} \left(\frac{t}{\lambda_1^{(s)}} \right)^2 - \dots \right], \quad (2.73)$$

which agrees closely with the exact result given by eq. (2.72).

Whenever the cutoff angle χ_S is small, angular deflections due to soft collisions may be described with the well-known small angle approximation [Le50]. Notice that χ_S can be made as small as desired by selecting a small enough value of C_s . Introducing the limiting form of the Legendre polynomials

$$P_\ell(\cos \chi) \simeq 1 - \frac{1}{4} \ell(\ell+1) \chi^2 \quad (2.74)$$

into eq. (2.65a) we obtain

$$\frac{1}{\lambda_\ell^{(s)}} = N 2\pi \frac{\ell(\ell+1)}{4} \int_0^{\chi_S} \chi^2 \frac{d\sigma(\chi)}{d\Omega} \sin \chi d\chi = \frac{\ell(\ell+1)}{2} \frac{1}{\lambda_1^{(s)}} \quad (2.75)$$

i.e., the transport mean free paths $\lambda_\ell^{(s)}$ are completely determined by the single value $\lambda_1^{(s)}$. The angular distribution $F_{GS}^{(s)}$ then simplifies to

$$F_{GS}^{(s)}(\theta; t) = \sum_{\ell=0}^{\infty} \frac{2\ell+1}{4\pi} \exp \left[-\frac{\ell(\ell+1)}{2} \frac{t}{\lambda_1^{(s)}} \right] P_\ell(\cos \theta). \quad (2.76)$$

This expression may be easily evaluated by a method similar to the one adopted to derive the Molière distribution. Using the Molière approximation for the Legendre

polynomials, eq. (2.43), and replacing the sum by an integral we find

$$F_{GS}^{(s)}(\theta; t) \simeq \frac{1}{2\pi} \left(\frac{\theta}{\sin \theta} \right)^{1/2} \int_0^\infty y \exp \left[-\frac{y^2 - 1/4}{2} \frac{t}{\lambda_1^{(s)}} \right] J_0(y\theta) dy \quad (2.77)$$

where $y = \ell + 1/2$. Changing to the variable

$$\omega = \left(\frac{2t}{\lambda_1^{(s)}} \right)^{1/2} y \quad (2.78)$$

we obtain

$$F_{GS}^{(s)}(\theta; t) \simeq \frac{1}{2\pi} \left(\frac{\theta}{\sin \theta} \right)^{1/2} \exp \left[\frac{t}{8\lambda_1^{(s)}} \right] \frac{\lambda_1^{(s)}}{2t} \int_0^\infty \omega \exp(-\omega^2/4) J_0 \left(\left[\frac{\lambda_1^{(s)}}{2t} \right]^{1/2} \theta \omega \right) d\omega, \quad (2.79)$$

which can be easily integrated to give (cf. eq. (2.56))

$$F_{GS}^{(s)}(\theta; t) = \frac{1}{2\pi} \left(\frac{\theta}{\sin \theta} \right)^{1/2} \frac{\lambda_1^{(s)}}{t} \exp \left[\frac{t}{8\lambda_1^{(s)}} - \frac{\lambda_1^{(s)}}{2t} \theta^2 \right]. \quad (2.80)$$

This distribution does not differ significantly from the gaussian distribution with variance $t/\lambda_1^{(s)}$. This result is accurate whenever $t \ll \lambda_1^{(s)}$ and $\chi_S \ll 1$. It offers a simple and systematic method to generate the angular deflection in artificial soft collisions. When the result given by eq. (2.80) is applicable, the single parameter $\lambda_1^{(h)}$ completely determines the multiple scattering distribution due to soft collisions, i.e. other details of the DCS for scattering angles less than χ_S are irrelevant.

Assembling all these pieces we obtain a powerful algorithm to simulate multiple elastic scattering processes in material structures, which may consist in several regions of different compositions separated by well defined surfaces (interfaces). Artificial soft collisions are considered as actual events, although their occurrence is correlated with that of hard collisions. The path between consecutive events is a straight segment. In the description of the algorithm we use the symbol \leftarrow in expressions like " $a \leftarrow b$ " to indicate that the value b replaces the value of a . The practical implementation of the algorithm to generate random electron tracks is as follows

1. Set the initial position \mathbf{r} and direction of movement $\hat{\mathbf{d}}$ of the electron.
2. Sample the length t of the step up to the next hard collision by using the formula (2.69).

3. Let the electron advance a random distance $\tau = t\xi$ in the direction $\hat{\mathbf{d}}$: $\mathbf{r} \leftarrow \mathbf{r} + \tau\hat{\mathbf{d}}$.
4. If the track has crossed an interface, stop it at the crossing point (i.e. redefine the value of \mathbf{r} as equal to the position of this point) and go to step 2 to continue the simulation in the new material (or end the simulation of this track when pertinent conditions are satisfied).
5. Simulate the artificial soft collision. Sample the polar scattering angle θ from the exact Goudsmit-Saunderson distribution given by eq. (2.71), or from the gaussian distribution given by eq. (2.80) when the small angle approximation is applicable. Sample the azimuthal scattering angle as $\phi = 2\pi\xi$. Perform a rotation $R(\theta, \phi)$ of the vector $\hat{\mathbf{d}}$ according to the sampled polar and azimuthal angles (as described, e.g. in refs. [Be63] and [SM86]) to obtain the new direction: $\hat{\mathbf{d}} \leftarrow R(\theta, \phi)\hat{\mathbf{d}}$.
6. Let the electron advance a distance $t - \tau$ in the direction $\hat{\mathbf{d}}$: $\mathbf{r} \leftarrow \mathbf{r} + (t - \tau)\hat{\mathbf{d}}$.
7. Do as in step 4.
8. Simulate a hard collision. Sample the polar scattering angle χ from the distribution (2.70). Generate the azimuthal scattering angle as $\phi = 2\pi\xi$. Perform a rotation $R(\chi, \phi)$ of the vector $\hat{\mathbf{d}}$ to obtain the new direction: $\hat{\mathbf{d}} \leftarrow R(\chi, \phi)\hat{\mathbf{d}}$.
9. Go to step 2.

The problem of interface crossing merits additional comments. The present algorithm handles it in a very simple way that, nevertheless, gives fairly accurate results. To see this, consider that a hard collision has occurred at the position \mathbf{r} in region "1" and assume that the next hard collision occurs in region "2". The path length t between these two hard collisions is larger than the distance s from \mathbf{r} to the interface (see fig. 2.6). If the artificial soft collision occurs in region "1", the angular deflection in this collision is sampled from the distribution $F_{GS}^{(s)}(\theta; t)$. Otherwise, the electron arrives at the interface without changing its direction of movement. Assuming $t \ll \lambda_1^{(s)}$, the mean angular deflection in a soft collision is

$$1 - \langle \cos \theta \rangle^{(s)} = 1 - \exp(-t/\lambda_1^{(s)}) \simeq \frac{t}{\lambda_1^{(s)}}. \quad (2.81)$$

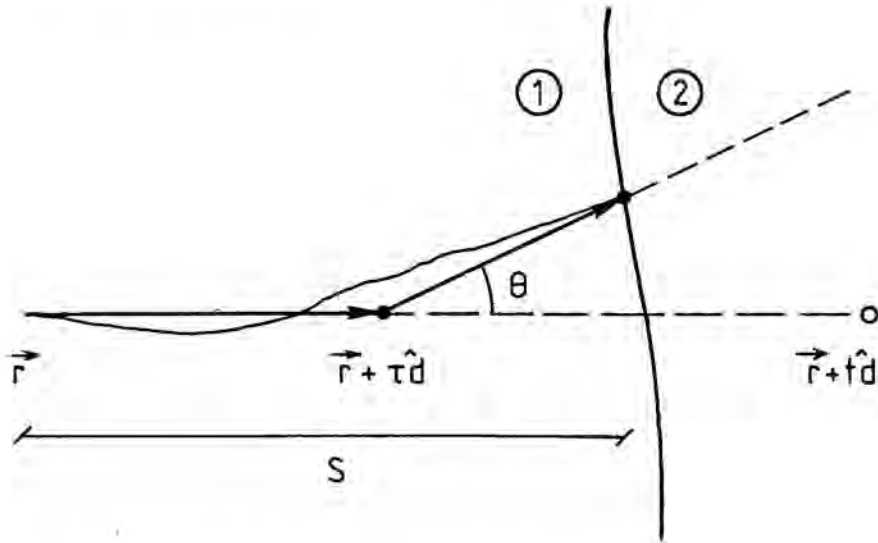


Figure 2.6. Simulation of a track near the crossing of an interface.

Moreover, when this assumption is valid, lateral displacements due to soft collisions are small and can be neglected to a first approximation. As the probability for the soft collision to occur within region "1" equals s/t , the average angular deflection of the simulated electron track when it arrives at the interface is

$$1 - \langle \cos \theta \rangle = \frac{s}{t} (1 - \langle \cos \theta \rangle^{(s)}) \simeq \frac{s}{\lambda_1^{(s)}}, \quad (2.82)$$

which practically coincides with the exact mean deviation after the path length s within region "1", as it must be. Thus, by sampling the position of the soft collision uniformly in the segment $(0, t)$ we make sure that the electron arrives at the interface with the correct average direction of movement.

In most practical cases the number of hard collisions per electron track can be made relatively large by simply using a small value of the parameter C_s —see eq. (2.66). When the number of steps is large enough, say larger than ~ 20 , it is not necessary to use the exact distribution $F_{GS}^{(s)}(\theta; t)$ to sample the angular deflection in artificial soft collisions. Instead, we may use a simpler distribution, with the same mean and variance, without appreciably distorting the simulation results. This is due to the fact that other details of the adopted distribution are washed out after a sufficiently large number of steps and will not manifest in the simulated distributions. Notice that, within the small angle approximation, it is necessary to keep only the proper value of the first moment to get the correct final distributions. However, if the cutoff angle χ_s is not small enough, the angular distribution $F_{GS}^{(s)}(\theta; t)$ may become sensitive to higher-order moments of

the soft single scattering distribution. Thus, by keeping also the proper value of the variance, we extend somewhat the range of validity of the simulation algorithm, i.e. we can speed up the simulation by using larger values of C_s (or of $\lambda^{(h)}$) and still obtain the correct distributions. A simple procedure to sample the angular deflection in soft collisions is described in the next section.

Although we are mainly concerned with elastic scattering, the present algorithm also can be adopted in practical simulations, where the slowing down of the particle along its track is taken into account. For the sake of simplicity, we assume that energy losses can be described by using the “continuous slowing down” approximation [Be63]. Let $S(E)$ denote the stopping power, i.e. the mean energy loss per unit path length. When the slowing down of the electrons is considered, our algorithm is still applicable provided the elastic cross section remains approximately constant along the step between two successive hard collisions or, equivalently, when the fractional energy loss in each step is small. As the average length of a step equals $\lambda^{(h)}$, the average fractional energy loss per step is $\lambda^{(h)}S(E)/E$, which has to be small. This condition is automatically satisfied by taking

$$\lambda^{(h)} = \max \{ \lambda, \min [C_s \lambda_1, D_s E/S(E)] \} \quad (2.83)$$

where D_s is a constant with a value of the order of 0.05 or smaller. The constants C_s and D_s determine the mean free path for hard elastic collisions; they play a role similar to that of the step length in conventional condensed simulations. When $C_s = D_s = 0$, the simulation becomes strictly detailed. By increasing the values of these constants we can speed up the simulation as much as desired. However, both of them should be kept relatively small (say, smaller than ~ 0.05) to ensure the accuracy of the simulation results. The step length of usual condensed simulations is subjected to similar restrictions.

In the following we will neglect energy losses. Further details on the implementation of the present algorithm in a Monte Carlo code, which also includes energy-loss processes, will be given in a forthcoming paper [FB92].

2.4 Simulating with a Wentzel model

The simulation method described above can be applied to any single scattering law. As realistic DCSs are only available in numerical form, practical simulations based on this

method will require extensive tabulations of the DCS as a function of the energy and the scattering angle (a problem which is also encountered in condensed simulations based on the Goudsmit-Saunders theory). Approximate analytical DCSs can, therefore, be of great value for practical purposes. The obvious candidate is a Wentzel model with properly selected parameters. The Wentzel model is illustrative since it allows a completely analytical formulation of the simulation algorithm. It is also useful to reveal some aspects of the algorithm (feasibility, stability, ...) that, even though valid for more realistic single scattering models, are difficult to put into evidence by general arguments. Moreover, several standard simulation codes [NH85, BB86] are based on the Molière's theory and, as mentioned before, have considerable difficulties to deal with spatial displacements and boundary crossing properly. Our algorithm with a Wentzel model provides a simpler and more consistent approach that is free of these difficulties.

Here, to simplify the notation, angular deflections are given in terms of the variable

$$\mu \equiv \frac{1 - \cos \chi}{2}, \quad (2.84)$$

which varies from 0 (forward scattering) to 1 (backward scattering). The Wentzel differential cross section, eq. (2.34) can be written in the form

$$\frac{d\sigma^{(W)}}{d\mu} = \sigma^{(W)} p_1(\mu) \quad (2.85)$$

where

$$p_1(\mu) = \frac{A(1+A)}{(A+\mu)^2} \quad (2.86)$$

is the probability distribution function of μ in a single collision.

The mean free path between hard collisions is determined from the adopted C_s value by using eq. (2.66), i.e. $\lambda^{(h)} = \max\{\lambda^{(W)}, C_s \lambda_1^{(W)}\}$ where $\lambda^{(W)} = 1/(N\sigma^{(W)})$ and $\lambda_1^{(W)} = \lambda^{(W)}/G_1^{(W)}$ is the first transport mean free path corresponding to the DCS given by eq. (2.85). The cutoff deflection $\mu_S = (1 - \cos \chi_S)/2$ is obtained from eq. (2.63) or, equivalently, from

$$\frac{\lambda^{(W)}}{\lambda^{(h)}} = \int_{\mu_S}^1 p_1(\mu) d\mu. \quad (2.87)$$

This equation can be easily solved to give

$$\mu_S = A \frac{\lambda^{(h)} - \lambda^{(W)}}{A\lambda^{(h)} + \lambda^{(W)}}. \quad (2.88)$$

Random sampling of the polar deflection in hard collisions can be performed by using the inverse transform method [Ru81], which leads to the sampling formula

$$\mu = \mu_S + \frac{(A + \mu_S)\xi(1 - \mu_S)}{(A + 1) - \xi(1 - \mu_S)}. \quad (2.89)$$

The first and second moments of the angular distribution due to the soft collisions along a step of length t , i.e. the moments of the distribution $F_{GS}^{(s)}(\mu; t) \equiv 4\pi F_{GS}^{(s)}(\theta; t)$, can be computed from the quantities

$$\begin{aligned} \frac{1}{\lambda_1^{(s)}} &= N2\pi \int_0^{x_s} [1 - \cos \chi] \frac{d\sigma^{(W)}(\chi)}{d\Omega} \sin \chi d\chi = \frac{2}{\lambda^{(W)}} \int_0^{\mu_s} \mu p_1(\mu) d\mu \\ &= \frac{2}{\lambda^{(W)}} A(1+A) \left[\ln \left(\frac{\mu_s + A}{A} \right) - \frac{\mu_s}{\mu_s + A} \right] \end{aligned} \quad (2.90)$$

and

$$\begin{aligned} \frac{1}{\lambda_2^{(s)}} &= N2\pi \int_0^{x_s} \frac{3}{2} [1 - \cos^2 \chi] \frac{d\sigma^{(W)}(\chi)}{d\Omega} \sin \chi d\chi = \frac{6}{\lambda^{(W)}} \int_0^{\mu_s} (\mu - \mu^2) p_1(\mu) d\mu \\ &= \frac{6}{\lambda^{(W)}} A(1+A) \left[(1+2A) \ln \left(\frac{\mu_s + A}{A} \right) - (1+2A + \mu_s) \frac{\mu_s}{\mu_s + A} \right]. \end{aligned} \quad (2.91)$$

Using eqs. (2.15) and (2.16), we find

$$\langle \mu \rangle^{(s)} = \frac{1 - \langle \cos \theta \rangle^{(s)}}{2} = \frac{1}{2} [1 - \exp(-t/\lambda_1^{(s)})] \quad (2.92)$$

and

$$\langle \mu^2 \rangle^{(s)} = \frac{1}{4} (1 - 2\langle \cos \theta \rangle^{(s)} + \langle \cos^2 \theta \rangle^{(s)}) = \langle \mu \rangle^{(s)} - \frac{1}{6} [1 - \exp(-t/\lambda_2^{(s)})]. \quad (2.93)$$

As mentioned before, to sample the polar angular deflection μ in artificial soft collisions, we can use any probability distribution $p_s(\mu)$ such that

$$\int_0^1 \mu p_s(\mu) d\mu = \langle \mu \rangle^{(s)}, \quad \text{and} \quad \int_0^1 \mu^2 p_s(\mu) d\mu = \langle \mu^2 \rangle^{(s)} \quad (2.94)$$

where $\langle \mu \rangle^{(s)}$ and $\langle \mu^2 \rangle^{(s)}$ are given by eqs. (2.92) and (2.93). Other details of the distribution $p_s(\mu)$ are irrelevant provided the number of hard collisions per track is statistically sufficient (say larger than ~ 20). In the calculations reported here we have used the distribution described in appendix B.

When the constant C_s is suitably small, the present algorithm leads to angular and spatial distributions that are virtually exact, i.e. they coincide with the distributions obtained from the exact solution of the transport equation with the same Wentzel DCS. In particular, when the WM model is adopted, the simulated angular distributions practically coincide with those that would be obtained with the original Molière theory; accurate spatial distributions, which are difficult to be properly simulated with

Molière's theory [BR86], are obtained as a fringe benefit. In any case, the simulation of each step with the present algorithm is easier than with the Molière distribution, eq. (2.53). This ensures the feasibility of practical simulations based on the Wentzel model.

It is also interesting to investigate the stability of the simulated angular and spatial distributions under variations in the constant C_s (or in the mean free path $\lambda^{(h)}$ between hard collisions). To this end, we consider the elastic scattering of 10 MeV electrons in silver ($Z=47$) using the W2 model. The parameters of this model, determined from the first and second transport mean free paths computed from the PWA-DCS given in table 2.1, are $\lambda^{(W)} = 6.87 \mu\text{g}/\text{cm}^2$ and $A = 4.2 \times 10^8$. Simulations have been performed for a path length $s = 0.1\lambda_1$ with $C_s = 0.02, 0.005$ and 0.0025 that correspond to 5, 20 and 40 hard collisions per track respectively. The average number of actual collisions along each track is $s/\lambda^{(W)} = 7.4 \times 10^4$. The simulation results presented here have been obtained from samples of 100000 tracks; the simulation of a track with 40 hard collisions takes 0.0026 seconds in an IBM 3090/600 VF computer. Angular and lateral displacement distributions are shown in figs. 2.7 and 2.8. The curves in fig. 2.7 are Goudsmit-Saunderson angular distributions calculated with the PWA- and the W2-DCS; their difference gives an indication of the adequacy of using the W2 model. It should be noted that the region where the differences seem to be important (θ less than ~ 10 deg actually corresponds to a quite small solid angle (~ 0.1 sr). The simulation algorithm does reproduce the exact angular distribution (i.e. the Gousmit-Saunderson distribution for the W2 model) when the number of hard collisions per track is about 20 or larger. Even for a value of C_s as large as 0.02 (5 hard collisions per track) the simulated distribution is still reasonably accurate. The simulated distribution of lateral displacements ($b \equiv (x^2 + y^2)^{1/2}$) is also insensitive to the value of C_s whenever the number of hard collisions per track is of the order of 20 or larger. In any case, the values of the quantities given by eqs. (2.15)–(2.19) obtained through simulation with the W2 model coincide exactly (apart from statistical uncertainties) with the values computed from the PWA-DCS.

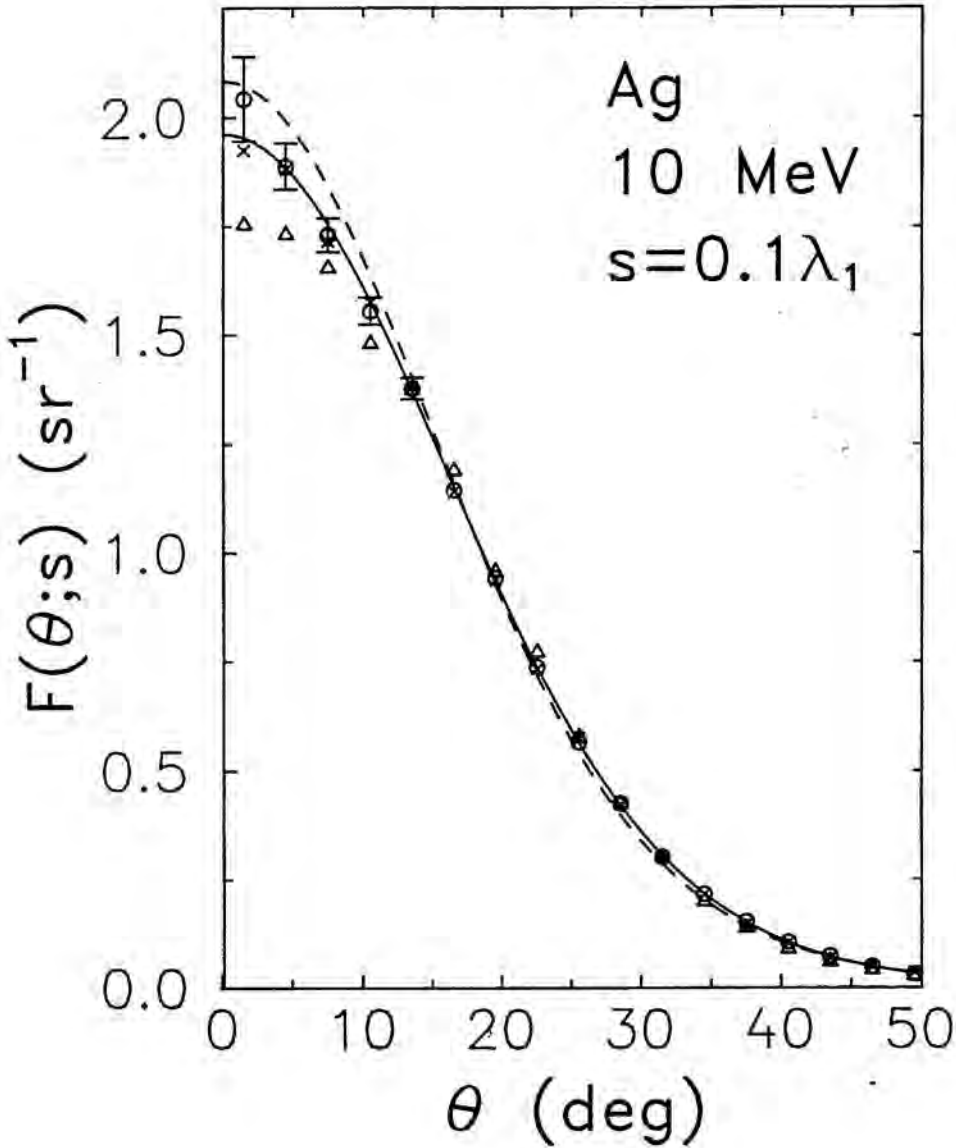


Figure 2.7. Calculated and simulated angular distributions of 10 MeV electrons in Ag after a path length $s = 0.1\lambda_1$, where λ_1 is the first transport mean free path given in table 2.1. The dashed and continuous curves are Goudsmit-Saunders distributions for the PWA- and W2-DCS respectively. Triangles, circles and crosses are results of Monte Carlo simulations with $n = 5, 20$ and 40 hard collisions per track respectively. Error bars represent statistical uncertainties (two standard deviations) in the simulation results for $n = 20$ (the other simulations have similar uncertainties).

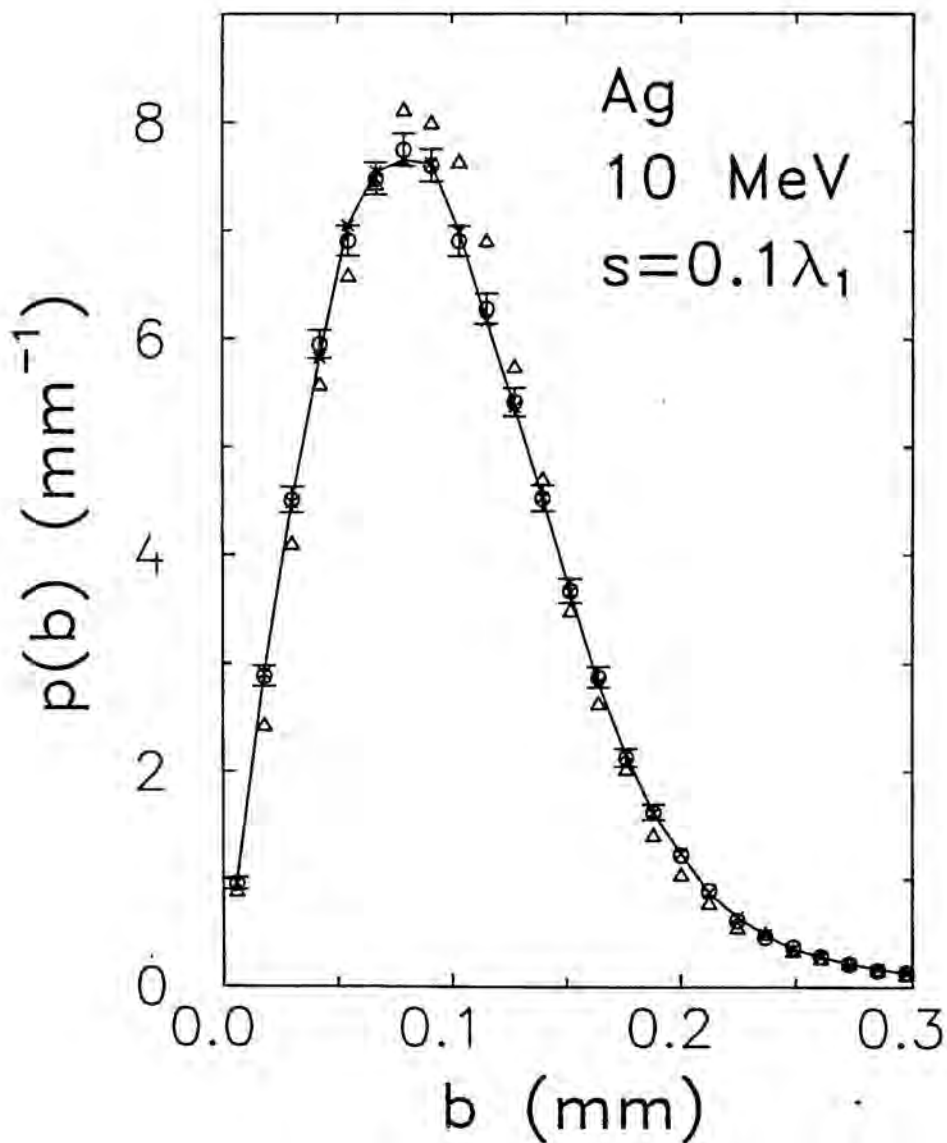


Figure 2.8. Distributions of lateral displacements, $b = (x^2 + y^2)^{1/2}$, of 10 MeV electrons after a path length $s = 0.1\lambda_1$ in Ag simulated with the W2 model. Triangles, circles and crosses represent results of Monte Carlo simulations with $n = 5, 20$ and 40 hard collisions per track. Crosses are joined by linear segments for visual aid.

2.5 Conclusions

We have considered some aspects of multiple scattering theories that are relevant for Monte Carlo simulation of electron transport. Our derivation of Molière's theory clarifies the physical assumptions and reliability of this theory. In particular, the original Molière theory has been shown to yield multiple scattering distributions that differ appreciably from the exact Goudsmit-Saunderson distribution for an accurate PWA-DCS. The differences arise mainly from the incorrect assumption that the DCS has a Rutherford-like behaviour for large scattering angles. We have also shown that the W2 model, with the proper values of the first and second transport mean free paths, yields multiple scattering distributions that are more accurate than those obtained from the WM model (i.e. from the Wentzel model adopted in the original Molière theory), at least for not too small path lengths.

The simulation algorithm described in section 2.3 effectively overcomes most of the difficulties of condensed simulation schemes. It can be applied to any single scattering law and requires much less numerical work than algorithms based on the Goudsmit-Saunderson distribution, since the tedious calculation of multiple scattering coefficients and the summation of Legendre series are effectively avoided. The algorithm is completely specified by the first and second transport mean free paths and by the DCS for scattering angles larger than χ_S . Therefore, details other than λ_1 and λ_2 of the DCS for scattering angles less than χ_S are irrelevant for multiple scattering simulation. Our algorithm leads also to accurate spatial distributions and ensures the proper simulation of electron tracks in the vicinity of interfaces.

When applied to the W2 model (or to the WM model), the present algorithm leads to a very simple simulation scheme that is more consistent than the current algorithms based on the Molière theory (e.g. the PRESTA algorithm [BR86]). The information needed to perform simulations with this simplified scheme reduces to the first and second transport mean free paths, which can be obtained from PWA calculations or from high-energy formulas such as those described in ref. [FM92]. Notice, however, that additional information is not required when the WM model is adopted. Actual simulations with the W2 model show that our algorithm is very stable under variations of the parameter C_s , provided C_s is less than ~ 0.05 and the mean number of hard collisions per track is larger than ~ 20 . Of course, this conclusion applies also to more realistic DCSs.

Chapter 3

Optical-data models

3.1 Introduction

During the last decade, a number of “optical-data” models to compute inelastic scattering of electrons in solids from knowledge of the optical oscillator strength (OOS) have been proposed. The common characteristic of these models is the use of an OOS obtained either from experimental optical data or from available calculations, which is extended into the non-zero momentum transfer region by means of a convenient and physically motivated recipe—the extension algorithm—thus obtaining a model of the generalized oscillator strength (GOS). The most appealing feature of the optical-data models lies in the fact that the differential cross section (DCS) for the most probable excitations (i.e. those involving low momentum transfers, which correspond to small scattering angles) turns out to be almost completely determined by the OOS. Thus an optical-data model incorporating an accurately measured OOS should yield a fairly accurate description of these excitations.

The origin of recent optical-data calculations is the “statistical” model of Tung et al. [TA79] which combines the OOS derived from the Local Plasma Approximation (LPA) [JI83] with the Lindhard theory of the free-electron gas (FEG) [Li54]. The LPA is based on the assumption that the electrons in each volume element of the target respond as if they were in a FEG of the same density and, thus, it allows the calculation of the OOS from only the knowledge of the local electron density. However, the LPA is not well motivated from a physical point of view and somewhat ambiguous in its application [MF91].

Ashley [As82,As88] proposed a optical-data model that incorporates experimental OOSs, thus avoiding the major limitation of the statistical model, and accounts for exchange effects in an heuristic way. To facilitate the calculations, Ashley used an extension algorithm of the “one-mode” or “plasmon-pole” type, which is attractive primarily since it is simple and, moreover, convenient to use in Monte Carlo simulation. This extension algorithm gives nearly the same dispersion relation as the Lindhard theory of the FEG. A more consistent approach, which combines “experimental” OOSs and the exact Lindhard theory for the FEG, has been proposed by Penn [Pe87]. Penn’s model has been extensively used by Tanuma, Powell and Penn [TP87,TP88,TP91a,TP91b] to compute inelastic mean free paths for electrons in solids. These theoretical mean free paths are currently considered as the most reliable for quantitative analysis with Auger electron spectroscopy and X-ray photoelectron spectroscopy.

Salvat and Mayol [SM90] have shown that optical-data models based on the FEG theory are not adequate to describe inner-shell ionization since they are not able to reproduce the ionization thresholds. They have also shown that a simple extension algorithm, which was first used by Liljequist [Li83], is well suited to describe inner-shell ionization.

It turns out that the relativistic optical-data model proposed by Salvat and Mayol has strong similarities with the Weizsäcker-Williams method of virtual quanta [Ja75], which is known to yield fairly accurate cross sections for inner-shell ionization [Ko67, SB82]. The Weizsäcker-Williams method exploits the fact that the electromagnetic field produced by a fast electron at the position of the target atom is equivalent to the superposition of two pulses of plane polarized radiation which impinge on the target in directions parallel and perpendicular to the direction of incidence of the projectile. Each Fourier component of these pulses is interpreted as a flux of virtual photons which can ionize the atom by the photoelectric effect. In the interaction, the projectile loses an energy equal to that of the absorbed photons. The cross section for distant inelastic collisions of a charged particle is thus determined from the photoelectric cross section. As the photoelectric cross section is proportional to the OOS (see below), the method of virtual quanta, which was developed some sixty years ago, can be qualified as the oldest optical-data model.

In this chapter we consider optical-data models suited for describing the inelastic interactions of electrons with matter. We limit our considerations to kinetic energies from ~ 10 eV to ~ 10 keV, for which relativistic effects are negligible. For higher en-

ergies, the approach described in chapter 4 is accurate enough for practical purposes. In this energy region, the computation of inelastic electron scattering is far from trivial if one wants to reach an accuracy better than, say, 5–10% in inelastic mean free path and stopping power. Usually, the validity of a model is analyzed by comparing these quantities with experimentally measured values. Such a comparison is not completely conclusive since the experimental values are usually determined by the overlayer method which yields attenuation lengths (i.e. including elastic scattering effects) rather than inelastic mean free paths (see e.g. ref. [JT90]). It may also be noted that there seem to be few experimental data on stopping power in the energy region referred to above. This has left open the possibility of some doubt as regards the choice of “best” model. Hence, it is of interest to study in which respect and up to what extent the results are sensitive to the adopted OOS and extension algorithm [FM92].

We describe a new optical-data model for calculating inelastic DCSs for electrons in solids. These DCSs permit the straightforward evaluation of important quantities such as the inelastic mean free path and the stopping power and can be adopted as the basis of Monte Carlo simulations of electron transport. Excitations of weakly bound electrons are described by using the FEG theory as extension algorithm, but bound-shell ionizations are described by means of the extension algorithm used in ref. [MS90]. Exchange effects between the projectile and the electrons in the medium have a non-negligible influence in the scattering process [As88] which is evident, for instance, in the stopping power even for high-energy projectiles. These effects are introduced through a modified Ochkur approximation [Oc64,Br83] which leads to the non-relativistic Møller DCS for binary electron collisions. Calculated inelastic mean free paths and stopping powers for five single element materials, for which OOS data are available from the literature, are presented. Analytical formulas for these quantities in terms of a few adjustable parameters are also given.

3.2 Born approximation

Inelastic interactions of electrons with kinetic energy E and isolated atoms or molecules can be described, to the first-order Born approximation, by means of the atomic DCS [In71]

$$\frac{d^2\sigma}{dQdW} = \frac{\pi e^4}{E} \frac{1}{WQ} \frac{df(Q,W)}{dW}, \quad (3.1)$$

where e is the electron charge, W is the energy transfer and Q is defined as (see appendix B)

$$Q = \frac{q^2}{2m}, \quad (3.2)$$

where q is the momentum transfer and m the electron mass. We may briefly refer to Q as the “recoil energy”, but it should be noted that it is equal to the recoil energy of the target only in the case where the target is a free electron at rest. The quantity $df(Q, W)/dW$ is the GOS, which completely characterizes the target (within the Born approximation). It may be heuristically interpreted as the “effective number of atomic electrons” that participate in an inelastic interaction with given values of the energy and momentum transfer. The GOS satisfies the Bethe sum rule [In71,MM65]

$$\int_0^\infty \frac{df(Q, W)}{dW} dW = Z, \quad (3.3)$$

where Z is the number of electrons per atom or molecule.

The GOS can be represented as a surface over the plane (Q, W) that is known as the Bethe surface [In71]. One may, at least roughly, infer the gross features of this surface from simple physical arguments. It is well known [In71] that for large values of W , the GOS vanishes except for $Q \simeq W$ and the Bethe surface reduces to a ridge, the Bethe ridge, which peaks around the line $Q = W$. Indeed, in the high- W limit, binding energies are negligible compared to the energy transfer W and the GOS may be evaluated by assuming the target electrons free and at rest (i.e. the collision can be considered as binary). This gives

$$\frac{df(Q, W)}{dW} \simeq Z\delta(W - Q). \quad (3.4)$$

Actually, the Bethe ridge has a finite width which arises from the momentum distribution of the atomic electrons. In the optical limit $Q = 0$, the GOS coincides with the OOS,

$$\frac{df(Q, W)}{dW} \simeq \frac{df(W)}{dW}, \quad (3.5)$$

and the Bethe sum rule eq. (3.3) reduces to the Thomas-Reiche-Kuhn sum rule (see e.g. ref. [BJ83]). In the limited range of Q values where this relation holds, the DCS eq. (3.1) decreases rapidly with Q . It follows that the key quantity to determine the DCS for low- Q excitations is the OOS.

Alternatively, for condensed media, one may work with the dielectric energy-loss function $\text{Im}[-1/\epsilon(Q, W)]$. The (complex) dielectric function $\epsilon(Q, W)$ of the stopping

material can be related to the GOS, so that the GOS—which originally is an atomic concept—can be applied to the solid state and to the homogeneous electron gas. In the latter case, it is convenient to refer to the GOS *per electron* rather than per atom, i.e. the Bethe sum rule eq. (3.3) for the electron gas GOS adds up to unity rather than to the atomic number Z . The GOS and the dielectric function describing the response of any isotropic medium to a small electromagnetic disturbance are related by [In71,Fa56]

$$\frac{df(Q, W)}{dW} = \frac{2W}{\pi\Omega_p^2} Z \cdot \text{Im} \left[\frac{-1}{\epsilon(Q, W)} \right]. \quad (3.6)$$

Ω_p is given by

$$\Omega_p = (4\pi\hbar^2 e^2 N Z / m)^{1/2}, \quad (3.7)$$

where N is the number of atoms or molecules per unit volume. Ω_p coincides with the plasmon energy of an homogeneous electron gas with a density equal to the average electron density of the stopping material.

The inelastic mean free path λ and the stopping power S for electrons in a certain medium are given by

$$\lambda^{-1} = N\sigma_0, \quad S = N\sigma_1, \quad (3.8)$$

where σ_0 and σ_1 are the total inelastic cross section and the stopping cross section respectively, which are defined by

$$\sigma_n \equiv \int_0^{W_{\max}} dW \int_{Q_-}^{Q_+} dQ W^n \frac{d^2\sigma}{dQdW}. \quad (3.9)$$

The maximum energy loss is $W_{\max}=E$ and, for a given W , the allowed recoil energies lie in the interval $Q_- \leq Q \leq Q_+$ given by (see appendix B)

$$Q_{\pm} = \left[E^{1/2} \pm (E - W)^{1/2} \right]^2. \quad (3.10)$$

The GOS is known analytically for only the simplest atomic target, namely the hydrogen atom (see e.g. ref. [In71]). The complex dielectric function of the FEG, derived from the Random Phase Approximation, has been given in analytical form by Lindhard [Li54]. GOSs for atoms and ions have been computed numerically by a number of authors [Ma71,Mc71] using independent electron models. Ashley et al. [AT79] have calculated electron inelastic mean free paths and stopping powers in solid aluminum using an electron gas theory, which includes plasmon damping, to describe excitations of the valence electrons and Manson's atomic GOSs [Ma71] for inner-shell ionization. In practice, it is very difficult to compute the GOS of solids from first principles, so that one must rely on approximate GOS models.

3.3 Free-electron gas

The FEG theory plays a central role in most of the optical-data models proposed to date. For our purposes, it is convenient to characterize the FEG by the plasmon energy \mathcal{E}_p , which is related to the electron gas density ρ through

$$\mathcal{E}_p(\rho) = (4\pi\hbar^2 e^2 \rho / m)^{1/2}. \quad (3.11)$$

The “one-electron” GOS for a FEG with plasmon energy \mathcal{E}_p is given by

$$F_L(\mathcal{E}_p; Q, W) = \frac{2W}{\pi \mathcal{E}_p^2} \cdot \text{Im} \left[\frac{-1}{\epsilon_L(\mathcal{E}_p; Q, W)} \right], \quad (3.12)$$

where $\epsilon_L(\mathcal{E}_p; Q, W)$ is the Lindhard dielectric function [Li54,Ri57]. It is worth noting that the OOS of the FEG (neglecting plasmon damping) reduces to the delta function

$$F_L(\mathcal{E}_p; 0, W) = \delta(W - \mathcal{E}_p). \quad (3.13)$$

The evaluation of one-electron cross sections (3.9) for a FEG with the GOS given by eq. (3.12) has to be performed numerically and is quite lengthy. To simplify the calculations, we will use the following two-modes (T) approximation for the one-electron GOS of the FEG

$$F_T(\mathcal{E}_p; Q, W) \equiv [1 - g(Q)] \delta(W - W_r(Q)) + g(Q) \delta(W - Q), \quad (3.14)$$

where

$$W_r(Q) = \mathcal{E}_p + BQ, \quad g(Q) = \min \left\{ 1, A \frac{Q^3}{\mathcal{E}_p^2(\mathcal{E}_p + Q)} \right\}. \quad (3.15)$$

The particular form of these functions and the values of the parameters A and B have been determined by requiring the resulting one-electron cross sections to agree closely with those computed from the Lindhard dielectric function (see below). The adopted values of the parameters are

$$A(\mathcal{E}_p) = \left(\frac{\chi^2}{3} \right)^{1/2} \left[\frac{1}{1 + 2\chi^2/3} + \frac{1}{\chi(1 - \chi^2/3)^{1/2}} \tan^{-1} \left(\frac{(1 - \chi^2/3)^{1/2}}{\chi} \right) \right] \quad (3.16)$$

and

$$B(\mathcal{E}_p) = \left(1 + \frac{\chi}{2} \right) \frac{6}{5} \frac{\mathcal{E}_F}{\mathcal{E}_p}, \quad (3.17)$$

where

$$\mathcal{E}_F \equiv \frac{\hbar^2}{2m} (3\pi^2 \rho)^{2/3} = \frac{1}{2} \left(\frac{9\pi^2}{16} \frac{\hbar}{me^4} \right)^{1/3} \mathcal{E}_p^{4/3} \quad (3.18)$$

is the Fermi energy of the FEG and

$$\chi^2 \equiv \frac{3}{16} \left(\frac{\mathcal{E}_p}{\mathcal{E}_F} \right)^2. \quad (3.19)$$

Evidently, we have

$$\int_0^\infty F_T(\mathcal{E}_p; Q, W) dW = 1. \quad (3.20)$$

Within a limited region of small Q , two excitation modes coexist. One mode or branch, with strength $1 - g(Q)$, corresponds to plasmon excitation; the other, with strength $g(Q)$, represents electron-hole excitation. For large Q , $g(Q) = 1$, i.e. the plasmon branch disappears, and the electron-hole excitation branch continues into the Bethe ridge. For small Q , $g(Q)$ decreases to zero roughly as Q^3 ; thus the strength of the plasmon branch is unity for $Q = 0$. In this way, the T model reflects the two major and related aspects of the collective behaviour of the FEG, namely the screening of the Coulomb interaction and the occurrence of plasma oscillations.

The mean free path and the stopping power of electrons moving in a FEG are given by $\lambda^{-1} = \rho\sigma_0$ and $S = \rho\sigma_1$, where σ_n are the one-electron cross sections (3.9). Here, however, the maximum energy loss is $W_{\max} = E - \mathcal{E}_F$ since larger energy losses would set the incident electron into a state below the Fermi level which is already occupied. It is worth to notice that the one-electron cross sections (3.9) with the GOS (3.14) can be evaluated analytically.

The expression (3.16) for the parameter A has been determined so as to exactly reproduce the mean free path and the stopping power obtained from Lindhard's theory in the low-energy limit (i.e. for electrons with kinetic energy much less than the plasmon energy). In this limit, the Lindhard theory allows the analytical evaluation of both λ and S (see refs. [Ri57] and [LW64]) and the resulting expressions coincide with those obtained from the T model. The parameter B determines the plasmon dispersion relation, i.e. the dependence of the plasmon energy with the recoil energy. According to the Lindhard theory, the plasmon line is given by $W_r(Q) = \mathcal{E}_p + 6\mathcal{E}_F Q / (5\mathcal{E}_p) + \mathcal{O}(Q^2)$. The slope of the plasmon line in the T model, given by eq. (3.17), has been determined empirically to improve the agreement of the computed mean free paths and stopping powers with the results of Lindhard's theory.

Inverse mean free paths and stopping powers of electrons in electron gases of different plasmon energies, computed from Lindhard's GOS, eq. (3.12), and from our T model, eq. (3.14), are compared in fig. 3.1. It is seen that the T model yields results which agree closely with those from the Lindhard theory. The maximum differences

between both calculations are of the order of a few percent and concentrate in the vicinity of the plasmon excitation threshold. In the following we shall use the T GOS model instead of the Lindhard GOS.

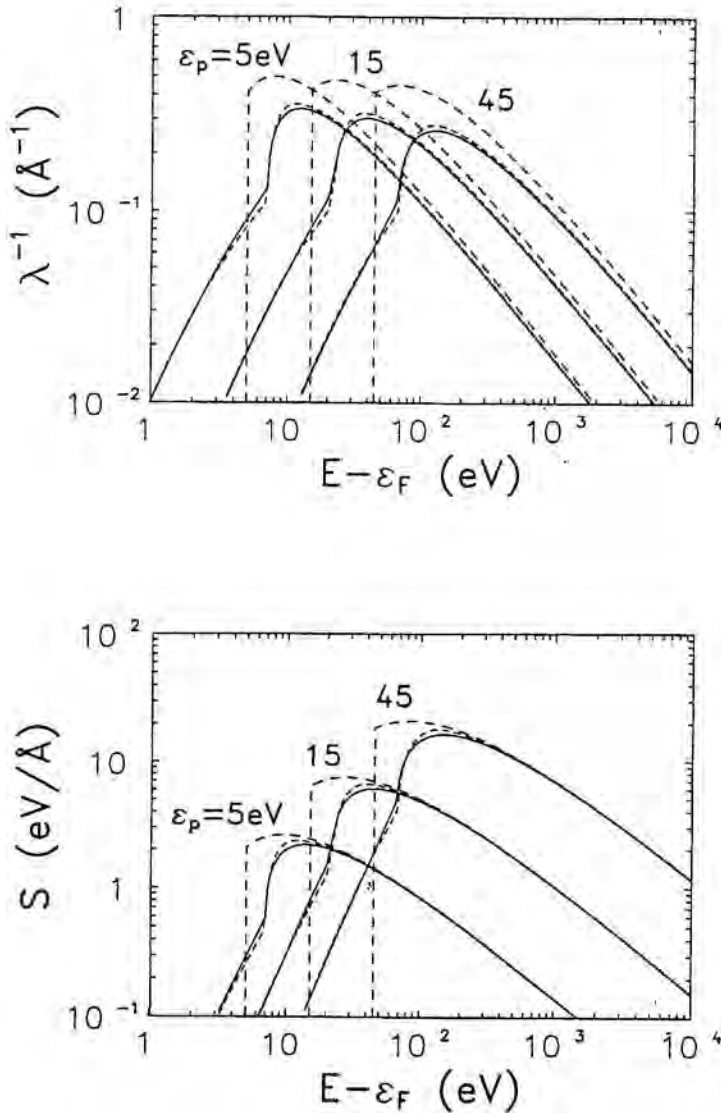


Figure 3.1. Inelastic inverse mean free path (a) and stopping power (b) for electrons in free electron gases with plasmon energies of 5, 15 and 45 eV. Full curves represent the results from Lindhard's theory; short-dashed broken curves have been obtained from the two-modes model given by eq. (3.14). The long-dashed broken curves are obtained by using the δ -oscillator, eq. (3.35).

3.4 Optical oscillator strength

As mentioned before, the basic ingredients of an optical-data model are the OOS and the extension algorithm. The calculation of inelastic mean free paths and stopping powers with the optical-data models requires the knowledge of the OOS for photon energies from ~ 1 eV up to an energy much larger than the binding energy of the K-shell of the target atoms. Experimental information on the low-energy part of the OOS is presently available for many materials, mainly from synchrotron radiation studies.

The “experimental” OOSs adopted in the present calculations have been obtained from available optical data either in the form of the refractive index n and the extinction coefficient κ [Pa85,HG74] or as the photoelectric cross section σ_{ph} [HL82,CC89]. In the first case, the OOS is evaluated by using the equation

$$\frac{df(W)}{dW} = \frac{2W}{\pi\Omega_p^2} Z \cdot \text{Im} \left[\frac{-1}{\epsilon(W)} \right], \quad (3.21)$$

where

$$\epsilon(W) \equiv \epsilon(Q = 0, W) = (n + i\kappa)^2, \quad (3.22)$$

is the complex dielectric constant. In the second case, the OOS is obtained by means of the relation [FC68]

$$\frac{df(W)}{dW} = \frac{mc}{2\pi^2 e^2 \hbar} \sigma_{\text{ph}}. \quad (3.23)$$

Unfortunately, for most materials, experimental optical data currently available extend over limited energy-loss ranges so that the complete OOS can only be obtained approximately by combining a variety of measured data (usually from different authors, obtained with various instruments and techniques and on different samples) with theoretical photoelectric cross sections. For the materials considered in the present calculations, we have constructed the “experimental” OOSs by combining

1. optical data (i.e. refractive index and extinction coefficient) from ref. [Pa85] for $W < 30.5$ eV,
2. X-ray photoabsorption cross-sections compiled and fitted by Henke et al. [HL82] for $30.5 \text{ eV} < W < W_{\text{ae}}$, and
3. theoretical photoelectric cross-sections of Cullen et al. [CC89] for $W > W_{\text{ae}}$. Here, W_{ae} stands for the energy of the absorption edge closer to and above 1 keV.

However, in the case of Al we have directly used the complex dielectric constant given by Smith et al. [SS85] which was obtained from experimental data, and carefully checked by Kramers-Kronig analysis [SS80]. All these OOSs are given in tabular form; in the numerical evaluation of integrals involving the OOS we have used the continuous function obtained by linear interpolation in a log-log representation of the tabulated values. The experimental OOSs for aluminium and copper are shown in fig. 3.2.

The self-consistency of the adopted OOSs can be checked by means of various sum-rules. Here we use the Thomas-Reiche-Kuhn sum rule (or f -sum) [BJ83,Pa85]

$$\frac{1}{Z} \int_0^\infty \frac{df(W)}{dW} dW = 1, \quad (3.24)$$

and the perfect-screening sum rule [PN89,Ma83] (or ps -sum) which, when written in terms of the OOS, takes the form

$$\frac{\Omega_p^2}{Z} \int_0^\infty \frac{1}{W^2} \frac{df(W)}{dW} dW = 1. \quad (3.25)$$

The main contributions to the ps -sum arise from the region of small energy losses and, therefore, this sum rule provides a check for the low energy-loss behaviour of the OOS. The f -sum is more sensitive to medium and large energy losses and, thus, it gives a global measure of the quality of the OOS in this region. The values of the sums (3.24) and (3.25), for the OOSs described above are given in table 3.1. The reliability of the OOS for Al [SS85] is supported by the values of the ps - and f -sums.

Table 3.1. Values of sum rules eqs. (3.24) and (3.25), the mean ionization energy and M_{tot}^2 for different materials.

Material	Z	f -sum	ps -sum	I (eV)	I_{BS} (eV)	M_{tot}^2
Al	13	0.993	0.977	165	166±2	3.08
Si	14	0.999	0.866	169	173±3	3.34
Cu	29	0.927	0.964	341	322±10	3.26
Ag	47	1.003	1.093	443	470±10	5.54
Au	79	0.962	1.080	781	790±30	6.20

The mean ionization energy I , which is the basic parameter in the high-energy Bethe stopping power formula, can be obtained from the OOS as

$$\ln I = \left[\int_0^\infty \frac{df(W)}{dW} dW \right]^{-1} \int_0^\infty \ln W \frac{df(W)}{dW} dW. \quad (3.26)$$

The mean excitation energies obtained from our experimental OOSs are compared with the values recommended by Berger and Seltzer [BS82] in table 3.1. Following Penn [Pe87], one may expect that an experimentally well determined OOS should be the most reliable to be found. It may however not always be available, so one should also look for other methods to obtain an estimate of the OOS. Also, it turns out that the OOS does not, in practice, need to be specified in very great detail, or with high accuracy in every detail to obtain good estimated of the mean free path and the stopping power. As compared to extensive tabulations, a simpler representation of the GOS in terms of a few parameters might be possible and sometimes even more convenient. This kind of approach [Li83,FM92] is outlined in chapter 4.

3.4.1 The Local Plasma Approximation

In the statistical model of Tung et al. [TA79], the OOS is obtained from the LPA. These authors considered a single-element scattering medium whose atoms have a locally varying atomic electron density $\rho(r)$. The LPA OOS is obtained by assuming that the response of the electrons in a volume element dv at r is the same as if they were in a FEG of density $\rho(r)$. Neglecting plasmon damping, the one-electron OOS for a FEG of density ρ reduces to the delta function (cf. eq. (3.13))

$$\left[\frac{df(W)}{dW} \right]_{\text{FEG}} = \delta[W - \mathcal{E}_p(\rho)]. \quad (3.27)$$

In the calculations reported here, we have used atomic electron densities obtained from Dirac-Hartree-Slater calculations with Wigner-Seitz boundary conditions. The LPA then leads to the following OOS

$$\left[\frac{df(W)}{dW} \right]_{\text{LPA}} = \int_0^{r_{\text{WS}}} \rho(r) \delta[W - \tau \mathcal{E}_p(\rho(r))] 4\pi r^2 dr, \quad (3.28)$$

where r_{WS} is the Wigner-Seitz radius, $\mathcal{E}_p(r)$ is the *local* plasmon energy

$$\mathcal{E}_p(\rho(r)) = (4\pi\hbar^2 e^2 \rho(r)/m)^{1/2}, \quad (3.29)$$

and τ is a constant which Tung et al. set at unity.

The parameter τ is introduced in order to obtain the correct mean ionization energy I computed from accurate experimental optical data. By using the value of τ given by

$$\ln \tau = \ln I - \frac{1}{Z} \int_0^{r_{ws}} \rho(r) \ln [\mathcal{E}_p(\rho(r))] 4\pi r^2 dr, \quad (3.30)$$

we make sure that the high-energy stopping power derived from the OOS eq. (3.28) will agree with the high-energy stopping power given by the Bethe formula (using the same I value).

In fig. 3.2, the experimental OOSs for Al and Cu are compared with the OOSs obtained from the LPA. The value of τ , as given by eq. (3.30), is 1.31 for Al and 1.26 for Cu. The LPA OOSs, with this value of τ , have been calculated from the Dirac-Hartree-Slater atomic densities. The LPA OOSs drop to zero at some maximum energy loss which is determined by the value of the electron density at the nucleus. For free-electron-like materials, such as Al, the LPA OOS roughly reproduces the plasmon line (which is located at the lower end of the excitation spectrum) since the density at the Wigner-Seitz radius nearly coincides with the valence electron density (bound electrons do not move so far from the nuclei). For other materials, as exemplified by Cu, the LPA leads to an unrealistic plasmon-like peak due to the non-vanishing value of ρ at the Wigner-Seitz radius. This behaviour is different from what is found for gases [JI83], where the LPA gives an OOS spectrum that starts from $W = 0$ (since then the density decreases smoothly when r goes to infinity). Although the LPA OOS tries to roughly reproduce even the absorption edges, it differs in shape from the experimental OOS. In the case of Al, there is a clear excess of the LPA OOS between the plasmon line and the L absorption edge. The fact that τ deviates appreciably from unity also points to the *ad hoc* and somewhat unsatisfying nature of the LPA.

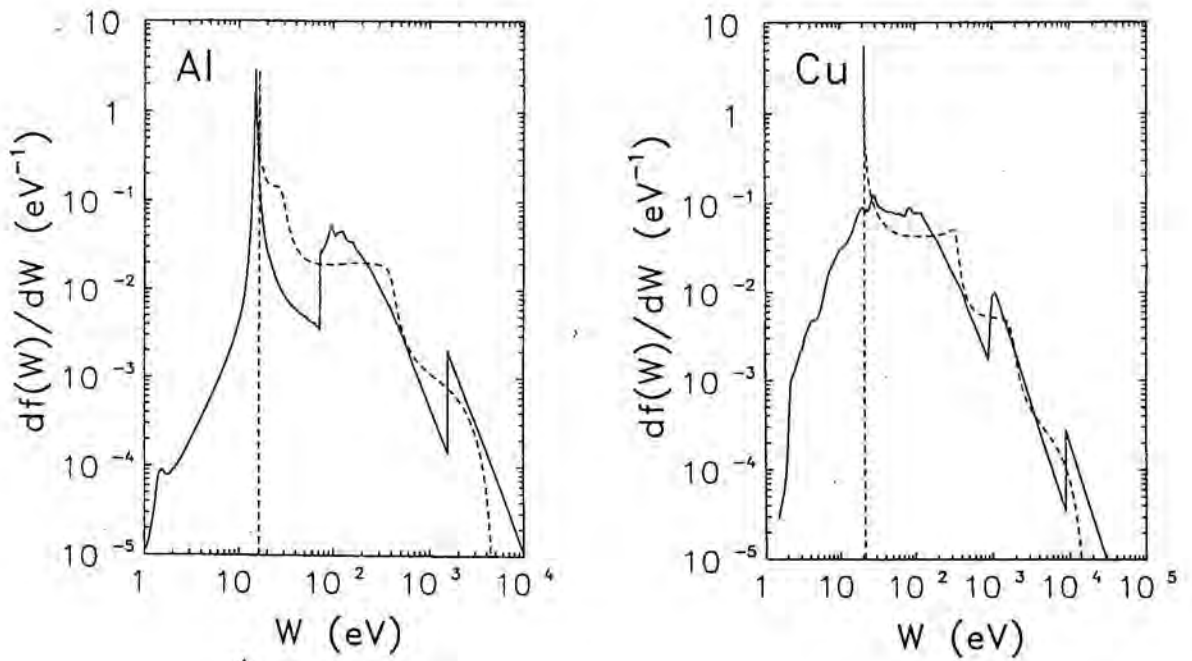


Figure 3.2. OOSs obtained as explained in the text (full curves) and computed from the LPA (eq. (3.28)) with Dirac-Hartree-Slater atomic densities (dashed curves) for Al (a) and Cu (b).

3.5 Optical-data models

In this section we briefly review different optical-data models proposed to date and compare the resulting mean free paths and stopping powers.

3.5.1 The statistical model

The statistical model of Tung et al. is equivalent to using the following GOS

$$\left[\frac{df(Q, W)}{dW} \right]_{\text{Tung}} = \int_0^\infty \left[\frac{df(W')}{dW'} \right]_{\text{LPA}} F_L(W'; Q, W) dW', \quad (3.31)$$

obtained extending the LPA OOS into the non-zero momentum transfer region with the Lindhard theory as extension algorithm. $F_L(W'; Q, W)$ is the one-electron GOS for a FEG whose plasmon energy is W' , as defined in eq. (3.12).

3.5.2 Ashley's model

Ashley [As82,As88,As89] uses a similar model which incorporates experimental OOSs, thus avoiding the major limitation of the statistical model. To facilitate further calculations, he introduced the following one-mode approximation for the one-electron GOS

$$F_P(\mathcal{E}_p; Q, W) \equiv \delta(W - W_r(Q)), \quad W_r(Q) \equiv \mathcal{E}_p + Q \quad (3.32)$$

As pointed out by Ashley, this one-mode or plasmon-pole (P) approximation gives nearly the same dispersion relation as Lindhard's theory in the low- Q limit and leads to the proper high- Q limit, $W \simeq Q$. The GOS obtained with Ashley's model is

$$\left[\frac{df(Q, W)}{dW} \right]_{\text{Ashley}} = \int_0^\infty \left[\frac{df(W')}{dW'} \right]_{\text{exp}} F_P(W'; Q, W) dW'. \quad (3.33)$$

Evidently, this GOS reduces to the experimental OOS in the limit $Q=0$. Moreover, the Bethe sum rule (3.3) is satisfied as long as the adopted OOS fulfils the Thomas-Reiche-Kuhn sum rule.

The extension algorithm eq. (3.32), or its more accurate version using the exact low- Q plasmon dispersion relation [Pe87], is so far the most extensively used in the literature. However, for inner-shell ionization, this extension algorithm shifts the ionization threshold from U_i , the actual ionization energy of the considered shell, to $2U_i$ [MS90].

3.5.3 Penn's model

The model proposed by Penn [Pe87] combines the advantages of the two previous models, since it incorporates experimental OOSs and it uses the Lindhard GOS per electron as extension algorithm. The GOS obtained from Penn's model may be expressed as

$$\left[\frac{df(Q, W)}{dW} \right]_{\text{Penn}} = \int_0^\infty \left[\frac{df(W')}{dW'} \right]_{\text{exp}} F_L(W'; Q, W) dW', \quad (3.34)$$

where $F_L(W'; Q, W)$ is the one-electron GOS of a FEG with plasmon energy W' as defined in eq. (3.12). Owing to the result given in eq. (3.13), the GOS eq. (3.34) reduces to the experimental OOS in the limit $Q=0$. Furthermore, the Bethe sum rule (3.3) is automatically satisfied, provided the adopted OOS fulfils the Thomas-Reiche-Kuhn sum rule. However, this model is not adequate for inner-shell ionization for it permits energy losses less than the resonance energy W' , i.e. it permits ionizations with energy transfer less than the actual ionization threshold U_i .

3.5.4 Shell model

Mayol and Salvat [MS90] have proposed an optical-data model that is more suited for describing inner-shell ionization. They used the following extension algorithm

$$F_\delta(W'; Q, W) \equiv \delta(W - W') \theta(W' - Q) + \delta(W - Q) \theta(Q - W'). \quad (3.35)$$

This one-electron GOS was first used by Liljequist [Li83] and is known as a δ -oscillator. The physical picture here is that the interaction typically has either "resonance" character or "free" (binary) character, corresponding to distant and close collisions, respectively [Bo48]. The GOS obtained from the shell model is

$$\left[\frac{df(Q, W)}{dW} \right]_{\text{MS}} = \int_0^\infty \left[\frac{df(W')}{dW'} \right]_{\text{exp}} F_\delta(W'; Q, W) dW'. \quad (3.36)$$

When the experimental OOS satisfies the f -sum rule, the GOS eq. (3.36) satisfies the Bethe sum rule. Moreover, it yields the proper thresholds for inner-shell ionization.

3.5.5 A comparison of optical-data models

Differences between the mean free paths and stopping powers computed from these optical-data models are the combined effect of the differences between the adopted

OOSs and extension algorithms.

The δ -oscillator can be considered as a rough approximation to the one-electron GOS for a FEG with plasmon energy equal to the resonance energy W' . The mean free paths and stopping powers for electrons in FEGs of different plasmon energies, calculated from the δ -oscillator approximation, are shown in fig. 3.1 for comparison purposes. It is seen that this approximation fails for incident electron energies about and below the plasmon excitation threshold, a fault shared to some extent with Ashley's P model. From the results plotted in fig. 3.1 we can get an idea of the magnitude of the differences between inelastic mean free paths and stopping powers computed from optical-data models that are based on the same OOS but use different extension algorithms.

The statistical model and Penn's optical-data model differ only in the adopted OOS. By comparing the mean free paths and stopping powers computed from these two approaches, we can elucidate the dependence of these quantities on the adopted OOS.

Inverse mean free paths and stopping powers for Al and Cu computed from the statistical model, eq. (3.31), with the adjusted value of τ (see eq. (3.30)) and with $\tau = 1$ and from Penn's model, eq. (3.34), are given in figs. 3.3 and 3.4 as functions of the electron energy. Expressions (3.31) and (3.34) have been evaluated using the T model eq. (3.14). For low energies, the LPA results lie below the results of Penn's model. This fact indicates that the LPA tends to concentrate the OOS at too high energy losses.

As a matter of fact, the LPA OOS, eq. (3.28), with the value of τ determined from eq. (3.30) fulfills the Bethe sum rule and, when used in eq. (3.26), it yields the accepted value of I . These two properties altogether determine the high-energy stopping power (Bethe formula). Therefore, the good agreement between the stopping powers computed from Penn's model and from the LPA, with the adjusted τ value, found for energies above 1 keV was to be anticipated. This is not the case for other quantities, e.g. the mean free path, which follow high-energy formulas determined by other moments of the OOS which are more or less distorted by the LPA [J183] (see below). From the present results it is quite evident that the LPA with $\tau = 1$ gives mean free paths more accurate than those obtained with the adjusted τ value. Hence, the use of the LPA with the adjusted τ value should be restricted to stopping power

calculations (and to energies above 100 eV). For the evaluation of inelastic mean free paths within the LPA it is preferable to use $\tau = 1$ (as it was done by Tung et al. [TA79]).

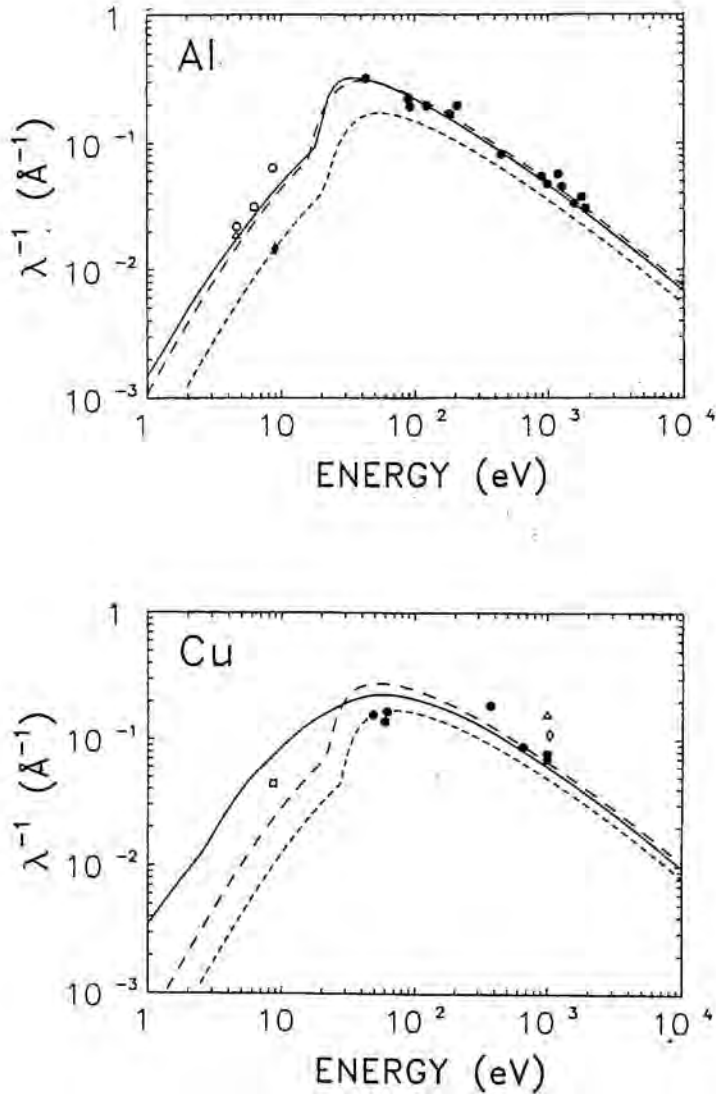


Figure 3.3. Inverse mean free path in Al (a) and Cu (b) as a function of the electron energy above Fermi level. The continuous curves are the results from Penn's model using the OOS given in fig. 3.2. The short-dashed curves are the LPA results obtained from the LPA OOS with $\tau=1.31$ for Al and 1.26 for Cu. LPA mean free paths calculated with $\tau=1$ are also given (long-dashed curves). Experimental data from ref. [TA79].

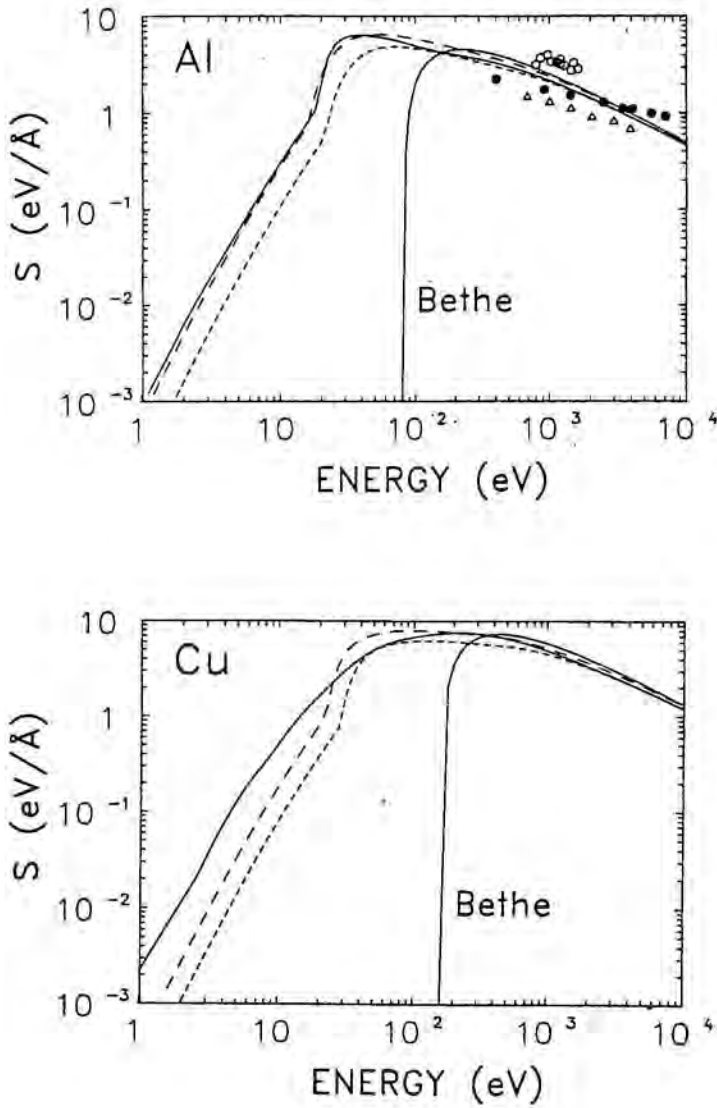


Figure 3.4. Stopping power for electrons in Al (a) and Cu (b). The curve labelled “Bethe” is the stopping power computed from the non-relativistic Bethe formula. Other details are the same as in fig. 3.3.

3.6 A new optical-data model

Fernández-Varea et al. [FM92] have compared different optical-data GOS models and suggested that a combination of Penn's model, eq. (3.34), (for valence electron excitations) and the model given by eq. (3.36) (for core electron excitations) could be a more convenient approach. To a first approximation, it is plausible to apply the T extension algorithm, eq. (3.14), for resonance energies W' which appear to be mainly of plasmon (collective) character, and to apply the δ -oscillator extension algorithm, eq. (3.35), to the rest of resonance energies. Accordingly, we shall adopt the following recipe to compute the GOS

$$\frac{df(Q, W)}{dW} = \int_0^\infty \left[\frac{df(W')}{dW'} \right]_{\text{exp}} F(W'; Q, W) dW' \quad (3.37)$$

with

$$F(W'; Q, W) = \begin{cases} F_T(W'; Q, W) & \text{if } W' < W_c, \\ F_\delta(W'; Q, W) & \text{if } W' > W_c. \end{cases} \quad (3.38)$$

The cutoff energy W_c separates the region of low resonance energies W' , where the excitations in the low- Q limit have a collective character, from the high resonance energy region where inner-shell ionization is dominant. In reality, there is an intermediate range of resonance energies where this distinction is difficult to make since, due to plasmon broadening, collective excitations may extend up to considerably high resonance energies.

The DCS given by eq. (3.1) can now be written as

$$\frac{d^2\sigma}{dQdW} = \int_0^\infty \left[\frac{df(W')}{dW'} \right]_{\text{exp}} \frac{d^2\sigma_1(W')}{dQdW} dW', \quad (3.39)$$

where

$$\frac{d^2\sigma_1(W')}{dQdW} = \frac{\pi e^4}{E} \frac{1}{WQ} F(W'; Q, W) \quad (3.40)$$

is the DCS per electron with resonance energy W' .

3.6.1 Exchange correction

When the swift particle is an electron, exchange between the projectile and the electrons in the medium must be taken into account. To our knowledge, exchange effects in optical-data model calculations have only been considered by Ashley [As88,As89], who

used an heuristic approach. A more conventional tool for dealing with exchange effects is provided by the Ochkur approximation [Oc64]. The Born-Ochkur DCS is given by

$$\frac{d^2\sigma}{dQdW} = \frac{\pi e^4}{E} \frac{1}{WQ} \left[1 - \frac{Q}{E} + \left(\frac{Q}{E} \right)^2 \right] \frac{df(Q, W)}{dW} \quad (3.41)$$

and is obtained by considering that the exchange scattering amplitude is approximately given by the leading term of an expansion of the Born-Oppenheimer amplitude in inverse powers of E [Br83]. Therefore, the Born-Ochkur approximation is essentially a high-energy approximation. For energies near the ionization thresholds, where optically allowed excitations (i.e. excitations with $Q \ll W$) dominate, the Born-Ochkur approximation gives a satisfactory description of exchange effects [Hi90]. On the other hand, collisions with energy loss W much larger than the energies of the electrons in the target can be described as binary collisions with free electrons at rest. The DCS for binary collisions may be calculated exactly [MM65] and, for projectiles with kinetic energy much larger than the Rydberg energy, it simplifies to the non-relativistic Møller DCS

$$\frac{d\sigma}{dW} = \frac{\pi e^4}{E} \frac{1}{W^2} \left[1 - \frac{W}{E - W} + \left(\frac{W}{E - W} \right)^2 \right]. \quad (3.42)$$

Clearly, this result differs from the limiting behaviour of the Ochkur exchange correction for large W .

We shall introduce exchange effects by using the following one-electron DCS

$$\frac{d^2\sigma_1(W')}{dQdW} = \frac{\pi e^4}{E} \frac{1}{WQ} \left[1 - \frac{Q}{E + W' - W} + \left(\frac{Q}{E + W' - W} \right)^2 \right] F(W'; Q, W). \quad (3.43)$$

The modification introduced here, which is permissible owing to the asymptotic nature of the Born-Ochkur approximation, agrees with the usual correction given in eq. (3.41) when $W = W'$ and has the desirable effect of leading to the non-relativistic Møller DCS, eq. (3.42), when $W \gg W'$ (since then $Q \simeq W$). Due to the indistinguishability of the “primary” and “struck” electrons, we can consider the primary as the most energetic after the collision. Owing to this convention, in collisions with free electrons at rest the energy loss of the primary electron cannot exceed the value $W_{\max} = E/2$. In the case of inner-shell ionization, the primary and secondary electrons have the same kinetic energy when $W = W_{\max} = (E + E_b)/2$, where E_b is the ionization energy of the considered shell. Notice that, by using this value for W_{\max} , the Ochkur correction keeps the ionization threshold unaltered.

The value of the maximum energy loss is also limited by the exclusion principle, which forbids energy losses larger than $E - E_F$ that would lead the projectile into an occupied state below the Fermi level E_F of the medium. E_F has been determined from the total number N_v of valence electrons per atom (see table 3.2).

Table 3.2. Number of valence electrons per atom N_v and Fermi energy E_F for different materials.

Material	N_v	E_F (eV)	W_c (eV)
Al	3	11.7	70
Si	4	12.5	90
Cu	11	34.8	50
Ag	11	27.2	50
Au	11	27.3	50

3.6.2 One-electron cross sections

The exchange corrected one-electron DCSs for $W' > W_c$ —i.e. when the extension algorithm is the δ -oscillator given by eq. (3.35)—are computed as

$$\begin{aligned} \frac{d^2\sigma_1(W')}{dQdW} &= \frac{\pi e^4}{E} \frac{1}{WQ} \left[1 - \frac{Q}{E} + \left(\frac{Q}{E} \right)^2 \right] \delta(W - W') \\ &+ \frac{\pi e^4}{E} \frac{1}{WQ} \left[1 - \frac{W}{E + W' - W} + \left(\frac{W}{E + W' - W} \right)^2 \right] \\ &\times \theta(W - W'). \end{aligned} \quad (3.44)$$

The first term in this expression corresponds to distant (“resonance”) collisions; the Ochkur correction factor has the usual form given by eq. (3.41). The second term accounts for close (“binary”) collisions; when $W' \ll E - W$, it reduces to the non-relativistic Møller DCS, eq. (3.42).

In order to get a general recipe which keeps the ionization thresholds unaltered, the maximum energy loss is taken to be $W_{\max}(W') = \min\{E - E_F, (E + W')/2\}$. This is equivalent to considering W' as the “binding energy” of the target electron. This assumption was also adopted by Ashley [As88] and it is justified by the fact that most inner-shell excitations occur for W' not much larger than the ionization threshold.

Electrons that participate in excitations with $W' < W_c$ are treated as if they were in a FEG with plasmon energy W' and described by using the two-modes GOS model given by eq. (3.14). Since the Ochkur exchange correction is based on the assumption of single-electron excitations, it is not justified for plasmon (i.e. collective) excitations of an electron gas. Therefore, the one-electron DCSs for $W' < W_c$ are splitted into contributions from electron-hole and plasmon-like excitations:

$$\frac{d^2\sigma_1(W')}{dQdW} = \frac{d^2\sigma_1^{(eh)}(W')}{dQdW} + \frac{d^2\sigma_1^{(pl)}(W')}{dQdW}. \quad (3.45)$$

The contribution from electron-hole excitations, including Ochkur's exchange correction, is given by (see eqs. (3.14) and (3.43))

$$\frac{d^2\sigma_1^{(eh)}(W')}{dQdW} = \frac{\pi e^4}{E} \frac{1}{WQ} \left[1 - \frac{Q}{E-W} + \left(\frac{Q}{E-W} \right)^2 \right] g(Q) \delta(W-Q). \quad (3.46)$$

Here the maximum energy loss is taken to be $W_{\max}(W') = \min\{E - E_F, E/2\}$, i.e. the "binding energy" is set equal to zero. The one-electron DCS for plasmon-like excitations is computed directly from eq. (3.40), i.e.

$$\frac{d^2\sigma_1^{(pl)}(W')}{dQdW} = \frac{\pi e^4}{E} \frac{1}{WQ} [1 - g(Q)] \delta(W - W_r(Q)) \quad (3.47)$$

and the maximum energy loss is $W_{\max}(W') = E - E_F$.

Finally, to obtain the inelastic mean free path λ and the stopping power S we have to compute the integrals

$$\sigma_n \equiv \int_0^\infty dW' \left[\frac{df(W')}{dW'} \right]_{\text{exp}} \sigma_n(W'), \quad (3.48)$$

where

$$\sigma_n(W') = \int_0^{W_{\max}(W')} dW \int_{Q_-}^{Q_+} dQ W^n \frac{d^2\sigma_1(W')}{dQdW} \quad (3.49)$$

are the one-electron total cross sections which, by using eqs. (3.44)–(3.47), can be evaluated analytically. The resulting expressions are a bit lengthy, but it is very simple to code them in a computer program. Thus, the numerical evaluation of λ and S reduces to a single quadrature.

3.6.3 Analytical formulas for λ and S

For practical purposes, it may be useful to have simple analytical formulas for the inelastic mean free path and the stopping power. We can use the asymptotic formulas

due to Bethe [In71] as a guide to obtain analytical expressions with a wider range of validity. The Bethe formula for the mean free path reads

$$\lambda^{-1} = N \frac{\pi e^4}{ER} \left[M_{\text{tot}}^2 \ln \left(\frac{4c_{\text{tot}} E}{R} \right) + \gamma_{\text{tot}}(R/E) + \mathcal{O}[(R/E)^2] \right], \quad (3.50)$$

where $R=13.6$ eV is the Rydberg energy, and

$$M_{\text{tot}}^2 \equiv \int_0^\infty \left(\frac{R}{W} \right) \frac{df(W)}{dW} dW \quad (3.51)$$

is determined by the OOS. The quantities c_{tot} and γ_{tot} are integral properties of the GOS, which cannot be computed from only the OOS.

The Bethe formula for the stopping power can be written as

$$S = N \frac{2\pi e^4}{E} Z \left[\ln \left(\frac{E}{I} \right) + \frac{1}{2}(1 - \ln 2) + \mathcal{O}(R/E) \right], \quad (3.52)$$

where I is the mean excitation energy defined by eq. (3.26). The second term in the right-hand side of eq. (3.52) originates from exchange effects; the computed stopping power for high-energy electrons would not agree with the Bethe formula if exchange were neglected.

From the Bethe formulas (3.50) and (3.52) we can expect that, for not too low energies, the calculated mean free paths and stopping powers may be closely reproduced by the following expressions

$$\lambda^{-1} = N \frac{\pi e^4}{ER} \left[M_{\text{tot}}^2 \ln \left(\frac{4a_1 E}{R} \right) + a_2(R/E) + a_3(R/E)^2 \right], \quad (3.53)$$

$$S = N \frac{2\pi e^4}{E} Z \left[\ln \left(\frac{E}{I} \right) + \frac{1}{2}(1 - \ln 2) + a_4(R/E) + a_5(R/E)^2 \right], \quad (3.54)$$

where the dimensionless quantities a_1, \dots, a_5 are considered as adjustable parameters to be determined by fitting the mean free paths and stopping powers obtained from our optical-data model calculations.

3.7 Calculation results

The evaluation of mean free paths and stopping powers is performed by following the theory described in section 3.6. The only free parameter in this theory is the cutoff energy W_c , which determines the extension algorithm to be used for each resonance energy—see eq. (3.38). As indicated before, there is some arbitrariness in this value,

but it is clear that extension algorithms based on the FEG theory should not be used for resonance energies W' larger than the binding energy of the outer bound-shell. In the present calculations, W_c is taken to be either the lowest absorption edge observed in the experimental OOS or 50 eV, whichever is smaller (see table 3.2). This prescription unambiguously determines W_c for free-electron-like materials, such as Al and Si, which have OOSs with a well-defined plasmon peak. On the contrary, transition and noble metals have OOSs much less structured and this makes the selection of W_c more uncertain. The effect of this parameter on λ and S is indicated in fig. 3.8 below, where we compare results obtained with $W_c = 25, 50$ and 75 eV for Ag. The stopping power is seen to be quite insensitive to the adopted value of W_c , except when the kinetic energy E of the swift electron is near the maximum of the curve $S(E)$. Mean free paths are more strongly dependent on this parameter. This dependence on W_c can be easily understood from the results plotted in fig. 3.1 and from the global analysis of ref. [FM92].

Computed inelastic mean free paths and stopping powers for Al, Si, Cu, Ag and Au are shown in figs. 3.5–3.9 as functions of electron kinetic energy. Kinetic energies are referred to the Fermi level E_F . For comparison purposes, we also give the results from the optical-data model calculations of Ashley [As88,As89] and of Tanuma et al. [TP91a]. These authors, however, used OOSs and extension algorithms which are different from the ones adopted here. Moreover, Ashley used a different approach to introduce exchange effects, which are neglected in the calculations on mean free paths by Tanuma et al. The magnitude of the exchange corrections on calculated λ and S is indicated in figs. 3.7a and 3.6b. Exchange effects have a stronger influence on the stopping power than on the mean free path (since S is more sensitive to the high energy loss part of the inelastic DCS).

Except for small kinetic energies, our calculation results can be closely approximated by the simple expressions (3.53) and (3.54). The parameters a_1, \dots, a_5 in these expressions have been determined by numerical fitting of the calculated λ and S for kinetic energies larger than 250 eV for λ and larger than $Z \times 10$ eV for S . The parameters so obtained are given in table 3.3. It is not convenient to extend the fit to lower energies, since λ and S have there some structure which cannot be reproduced by the simple expressions (3.53) and (3.54).

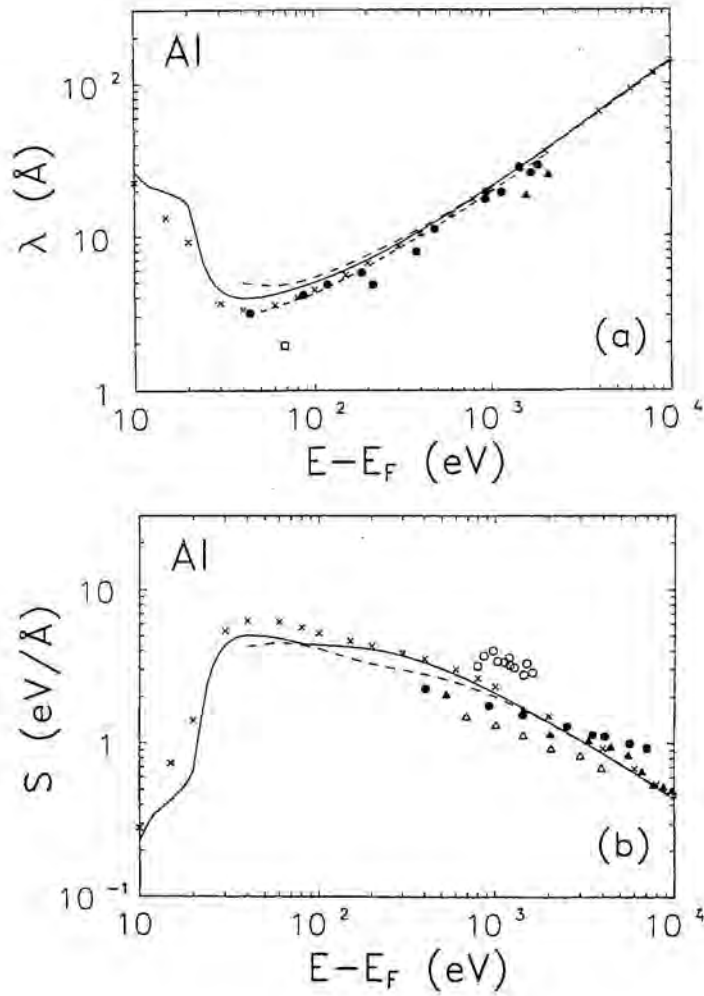


Figure 3.5. Inelastic mean free path (a) and stopping power (b) for Al. Results from the present optical-data model are represented as full curves. Short-dashed and long-dashed broken curves represent optical-data model calculations of Tanuma et al. [TP91a] and of Ashley [As89] respectively. Crosses are theoretical results from Ashley et al. [AT79]. Experimental data from different authors are taken from ref. [DS89].

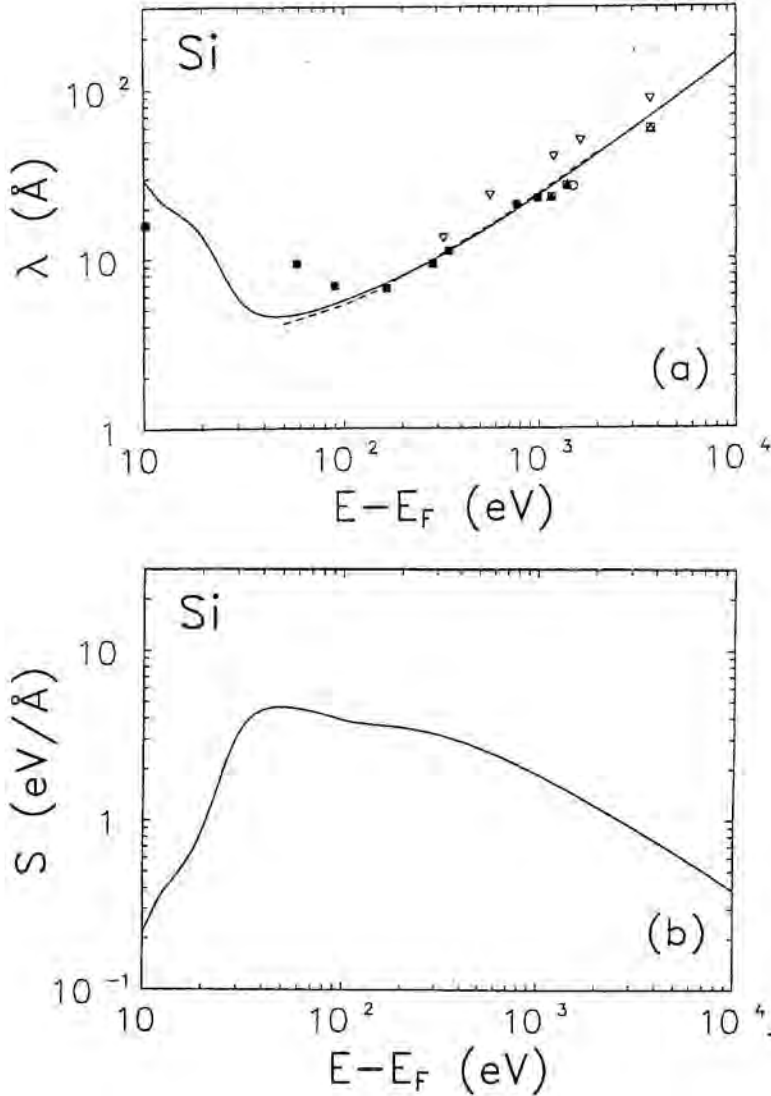


Figure 3.6. Inelastic mean free path (a) and stopping power (b) for Si. Results from the present optical-data model are represented as full curves. Results obtained by excluding the Ochkur exchange correction are represented as long-dashed broken curves. The short dashed curve represents the mean free path calculated by Tanuma et al. [TP91a]. Experimental data from different authors are taken from ref. [DS89].

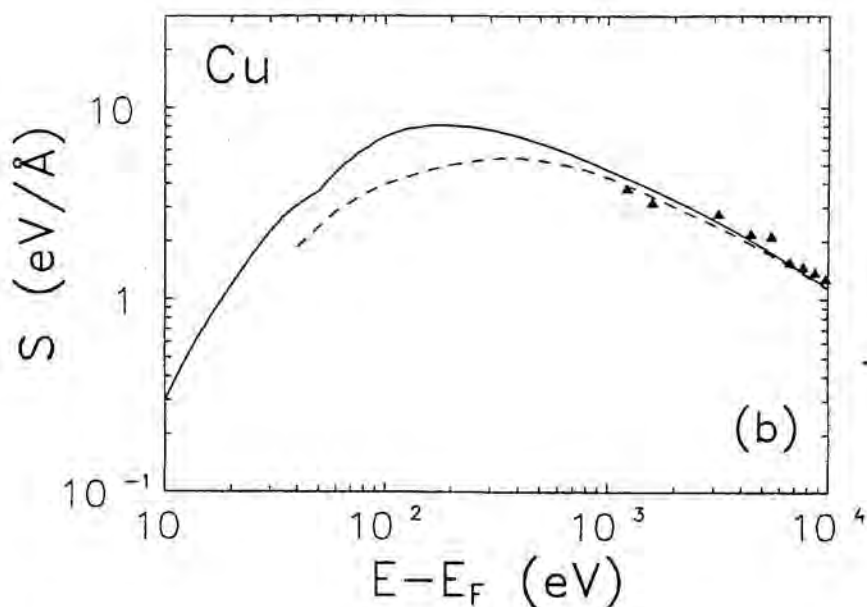
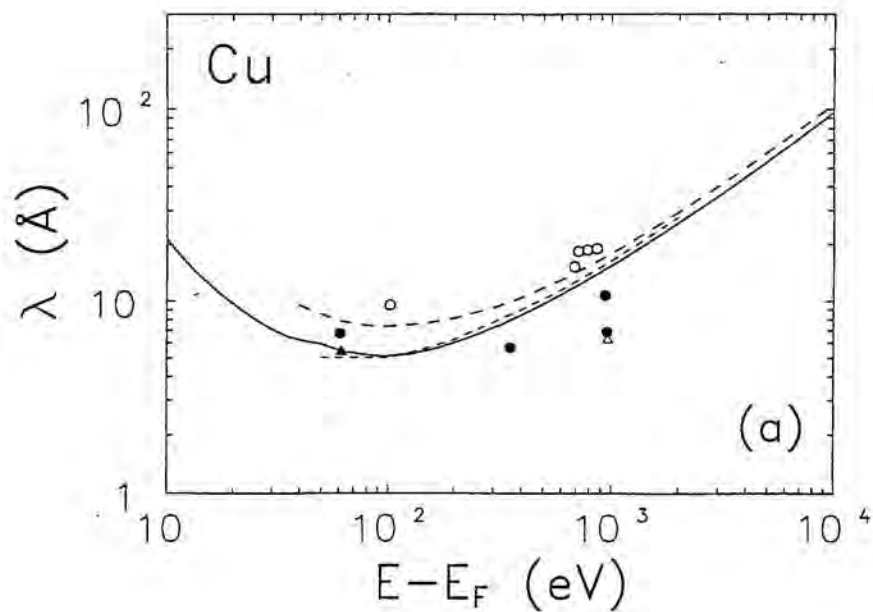


Figure 3.7. Inelastic mean free path (a) and stopping power (b) for Cu. Results from the present optical-data model are represented as full curves. Short-dashed and long-dashed broken curves represent optical-data model calculations of Tanuma et al. [TP91a] and of Ashley [As89] respectively. Experimental data from different authors are taken from ref.

[DS89].

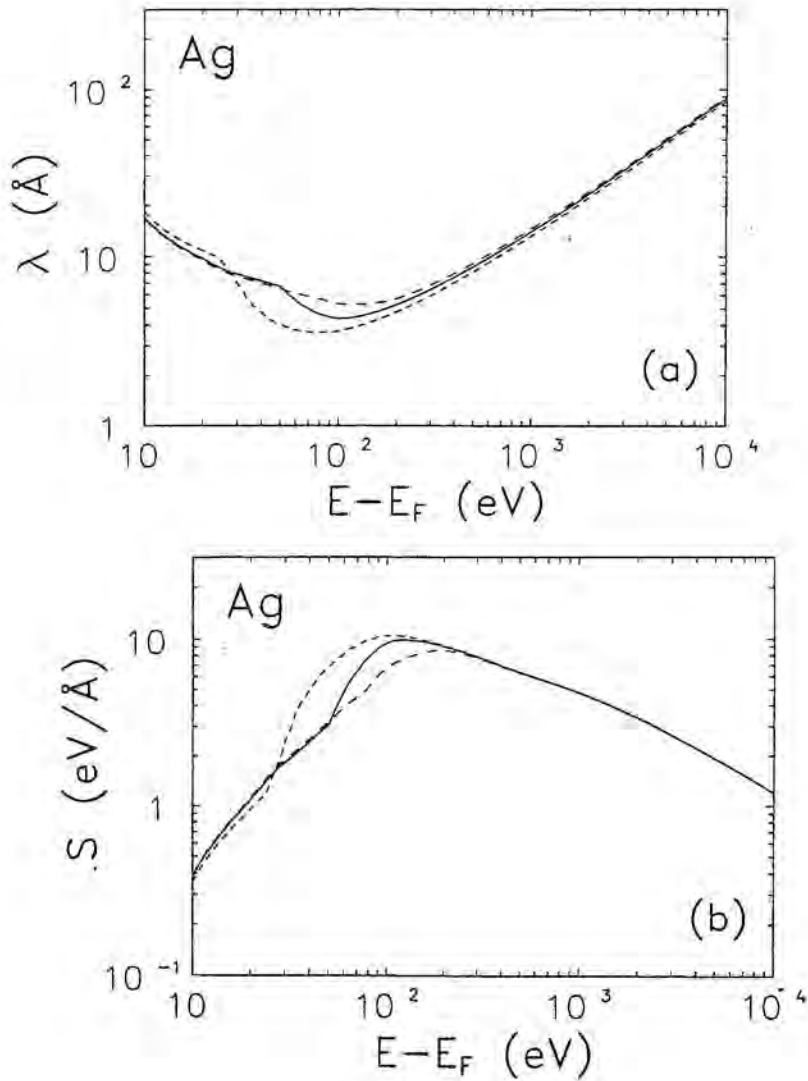


Figure 3.8. Inelastic mean free path (a) and stopping power (b) for Ag. Results obtained from the present optical-data model with a cutoff energy W_c equal to 25, 50 and 75 eV are represented as short-dashed, full and long-dashed curves respectively. Experimental data from different authors are taken from ref. [DS89].

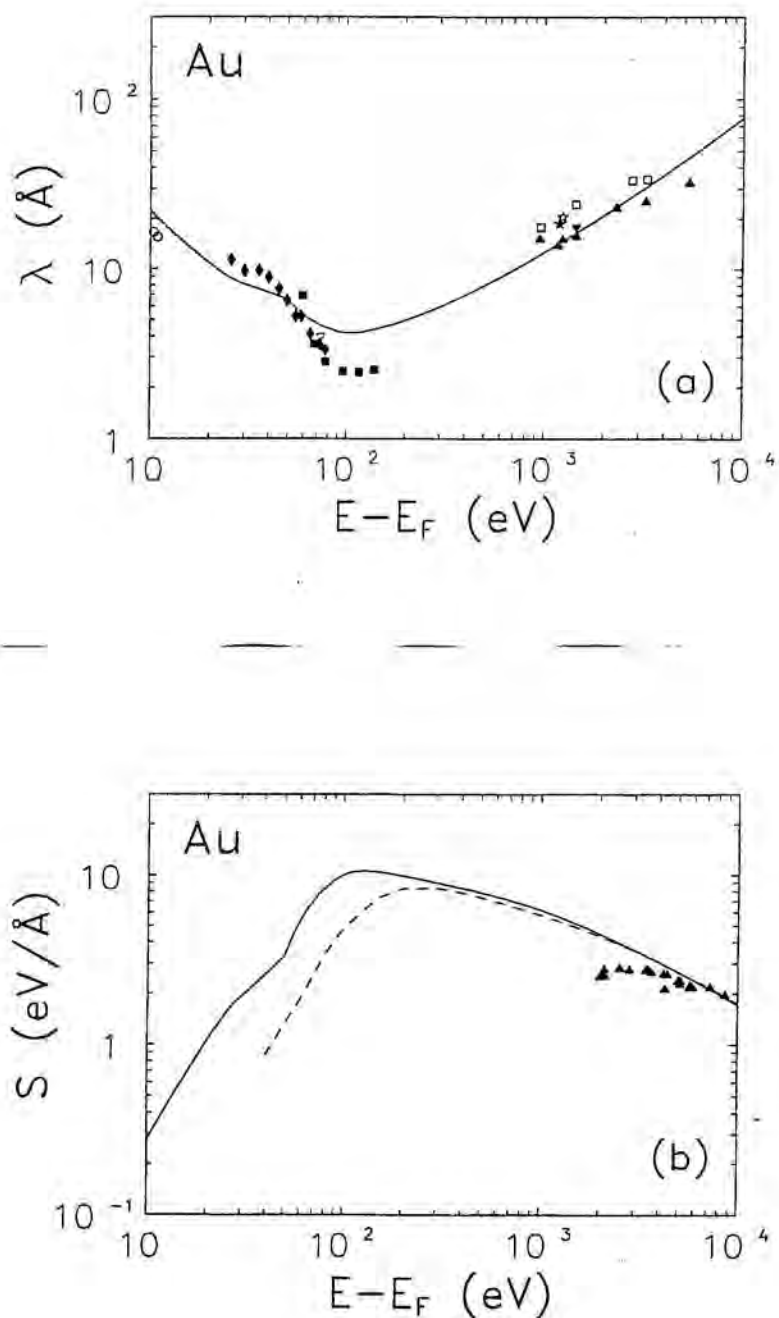


Figure 3.9. Inelastic mean free path (a) and stopping power (b) for Au. Results from the present optical-data model are represented as full curves. Short-dashed and long-dashed broken curves represent optical-data model calculations of Tanuma et al. [TP91a] and of Ashley [As89] respectively. Experimental data from different authors are taken from ref.

[DS89].

Table 3.3. Parameters of the fit for eqs. (3.53) and (3.54).

Material	a_1	a_2	a_3	a_4	a_5
Al	0.8993	-69.16	650.8	8.286	-22.27
Si	0.8321	-70.02	630.1	8.394	-24.12
Cu	0.8901	-184.7	2211.9	20.48	-115.8
Ag	0.4869	-178.4	1913.4	31.84	-361.2
Au	0.5462	-288.7	3443.4	64.53	-1361

3.8 Conclusions

We have described an optical-data model which provides a consistent picture of inelastic scattering of electrons in solids. The basic ingredient is the OOS, ideally to be obtained from experiments. Excitations of collective character and inner-shell ionization are described separately by means of simple extension algorithms. Exchange effects between the projectile and the electrons in the medium are taken into account by using a modified Ochkur approximation. The calculation results reproduce the general trends of experimental data in a satisfactory way, and may be accurately fitted by simple analytical formulas. However, owing to the considerable experimental uncertainties and to the scattering of the data measured by different authors, it is not possible to extract more definite conclusions about the reliability of the calculations from a comparison with experimental data.

Chapter 4

Energy loss of fast electrons

4.1 Introduction

An important aspect of Monte Carlo transport algorithms is the description of the energy loss events which determine the slowing down of energetic electrons and positrons. The energy released by these particles is directly transferred to the medium or emitted as electromagnetic radiation. It is customary to speak of collision losses and radiative losses. Collision energy losses are understood to include losses due to ionization and excitation of the atoms, plasmon excitation in metals and emission of Cerenkov radiation. Radiative losses refer exclusively to bremsstrahlung emission.

The details of the energy loss simulation in the existing Monte Carlo codes depend mainly on the energy range of interest. Detailed simulations, where all the scattering events suffered by the particle are described in chronological succession, are only feasible at low energies [IS81,Li85,MM90]. At high energies, the number of events along each particle track is very large and detailed simulation is impracticable. A quite usual practice in high-energy simulations is to combine the detailed simulation of hard events, involving energy losses larger than a given threshold W_c (“catastrophic” events in the terminology of Berger [Be63]), with a continuous slowing down approximation for soft events with energy losses less than W_c (thus neglecting energy straggling due to these events). In schemes of this type (see e.g. refs. [Be63,BB86,NH85,IL86]), the restricted stopping power due to soft events is usually derived from the high-energy Bethe formula [BS84,Fa63]. Moreover, hard collisions are frequently described as binary collisions with free electrons at rest (through the Møller [Mo32] and Bhabha [Bh36]

DCSs). As the binding energies of the target electrons are neglected, this procedure overestimates the initial energy of delta rays (secondary electrons). These features limit the validity of this kind of simulation to primary particles and delta rays with energies much higher than the ionization energies of the target atoms. Other high-energy approaches [Be63,BB86] have recourse to multiple scattering theories such as those due to Landau [La44], Blunck and Leisegang [BL50] and Vavilov [Va57], which give the energy loss distribution due to inelastic collisions in a given path length. The validity of these multiple scattering theories is also limited to high energies and, moreover, they do not allow the simulation of delta ray generation.

The aim of the present chapter is to describe a set of analytical DCSs for inelastic collisions and bremsstrahlung emission suitable for being used as the basis of Monte Carlo simulation of electron transport in materials of arbitrary composition. The proposed DCSs are based on high-energy approximations complemented with semiempirical ingredients in such a way that they provide an accurate description of energy loss events in a wide energy range. They are characterized by a few readily available parameters and can be easily evaluated with the aid of a short computer code. These DCSs are well suited for detailed Monte Carlo simulations. The random sampling of the energy loss in each event can be performed by using purely analytical methods. Furthermore, when used in high-energy simulations, these DCSs allow easy calculation of the restricted stopping power and energy straggling parameter due to soft events, even when the cutoff energy loss W_c is comparable to the atomic binding energies.

The DCS for collision losses is calculated from a generalized oscillator strength model defined by the electronic configuration, ionization energies of the various electron shells of the target atoms and the mean excitation energy I which enters into the Bethe formula [BS84,Fa63]. Our approach is similar to those used by Sternheimer [St52] and Liljequist [Li83] for more restricted purposes. It leads to an analytical DCS which includes the so-called shell correction and the Fermi density effect correction in an approximate way and also allows the simulation of delta ray production.

Radiative losses are described on the basis of the Bethe-Heitler DCS with exponential screening as carried out previously by Schiff [Sc51] and Tsai [Ts74]. Our DCS includes a high-energy Coulomb correction as well as an empirical correction to compensate for the failure of the Born approximation at low energies. The screening radius is determined from accurate high-energy calculations [SB85,HG80] in a way which ensures that, in the high-energy limit, the radiative stopping power computed from our

DCSs). As the binding energies of the target electrons are neglected, this procedure overestimates the initial energy of delta rays (secondary electrons). These features limit the validity of this kind of simulation to primary particles and delta rays with energies much higher than the ionization energies of the target atoms. Other high-energy approaches [Be63,BB86] have recourse to multiple scattering theories such as those due to Landau [La44], Blunck and Leisegang [BL50] and Vavilov [Va57], which give the energy loss distribution due to inelastic collisions in a given path length. The validity of these multiple scattering theories is also limited to high energies and, moreover, they do not allow the simulation of delta ray generation.

The aim of the present chapter is to describe a set of analytical DCSs for inelastic collisions and bremsstrahlung emission suitable for being used as the basis of Monte Carlo simulation of electron transport in materials of arbitrary composition. The proposed DCSs are based on high-energy approximations complemented with semiempirical ingredients in such a way that they provide an accurate description of energy loss events in a wide energy range. They are characterized by a few readily available parameters and can be easily evaluated with the aid of a short computer code. These DCSs are well suited for detailed Monte Carlo simulations. The random sampling of the energy loss in each event can be performed by using purely analytical methods. Furthermore, when used in high-energy simulations, these DCSs allow easy calculation of the restricted stopping power and energy straggling parameter due to soft events, even when the cutoff energy loss W_c is comparable to the atomic binding energies.

The DCS for collision losses is calculated from a generalized oscillator strength model defined by the electronic configuration, ionization energies of the various electron shells of the target atoms and the mean excitation energy I which enters into the Bethe formula [BS84,Fa63]. Our approach is similar to those used by Sternheimer [St52] and Liljequist [Li83] for more restricted purposes. It leads to an analytical DCS which includes the so-called shell correction and the Fermi density effect correction in an approximate way and also allows the simulation of delta ray production.

Radiative losses are described on the basis of the Bethe-Heitler DCS with exponential screening as carried out previously by Schiff [Sc51] and Tsai [Ts74]. Our DCS includes a high-energy Coulomb correction as well as an empirical correction to compensate for the failure of the Born approximation at low energies. The screening radius is determined from accurate high-energy calculations [SB85,HG80] in a way which ensures that, in the high-energy limit, the radiative stopping power computed from our

DCS agrees with the most reliable values available to date [BS84,SB85].

For the sake of simplicity, we consider a single-element medium of atomic number Z and mass density ρ . The number of atoms per unit volume is given by

$$N = \frac{N_A \rho}{A}, \quad (4.1)$$

where N_A is Avogadro's number and A is the atomic weight of the material.

4.2 Collision losses

The quantum theory of the energy loss of fast charged particles due to their inelastic collisions with atoms was initiated by Bethe (see e.g. ref. [In71]). The Bethe theory applies to separate atoms or molecules, i.e. to gases. The quantum stopping theory for condensed media was worked out by Fano [Fa63]. The main result of the Bethe theory is the well-known analytical formula for the collision stopping power S_c , i.e. the average energy loss per unit path length, of high-energy charged particles. For electrons and positrons with kinetic energy E , the Bethe stopping power formula reads [BS84,Bi58,RC54]

$$S_c^{(\pm)}(E) = NZ \frac{2\pi e^4}{mv^2} \left\{ \ln \left[\frac{E^2}{I^2} \frac{\gamma + 1}{2} \right] + f^{(\pm)}(\gamma) - 2\frac{C}{Z} - \delta \right\} \quad (4.2)$$

(hereafter, the quantities referring to electrons and positrons will be denoted by superscripts “-” and “+” respectively). The quantity I is the mean excitation energy, which has been determined empirically for a large number of materials [BS84], and

$$f^{(-)}(\gamma) = \frac{1}{\gamma^2} - \frac{2\gamma - 1}{\gamma^2} \ln 2 + \frac{1}{8} \left(\frac{\gamma - 1}{\gamma} \right)^2 \quad (4.3)$$

for electrons and

$$f^{(+)}(\gamma) = 2 \ln 2 - \frac{\beta^2}{12} \left[23 + \frac{14}{\gamma + 1} + \frac{10}{(\gamma + 1)^2} + \frac{4}{(\gamma + 1)^3} \right] \quad (4.4)$$

for positrons. The term $2C/Z$ accounts for the so-called shell correction [BS84,Fa63] and δ is the density effect correction [St52,SP71,SB84]. δ is negligibly small for non-relativistic energies (see below), whereas the shell correction tends to vanish at high velocities (i.e. much larger than the orbital velocities of the electrons in the target). The shell correction is usually disregarded in high-energy Monte Carlo codes, whereas the density effect correction is evaluated by using the formulas due to Sternheimer and Peierls [SP71], which give the reduction of the stopping power due to this effect quite accurately.

4.2.1 Schematic Bethe surface

The Bethe formula (4.2) only gives the mean energy loss per unit path length. What we seek is a more complete description of collision energy losses, preferably allowing the simulation of delta ray emission, at least in an approximate way. With reference to high-energy Monte Carlo simulations, it would also be useful to have a simple procedure to compute the restricted stopping power, i.e. the average energy loss per unit path length due to soft excitations with energy transfers less than a given value of W_c .

Let us first consider the inelastic interactions of electrons or positrons with an isolated atom (or molecule) containing Z electrons in its ground state. We start from the non-relativistic theory and, for electrons, we disregard exchange effects between the electrons in the target atom and the incident electron; relativistic corrections (including the density effect for condensed media) and the effect of exchange will be introduced later. The DCS for inelastic collisions with energy loss W and recoil energy Q (see the appendix), as derived from the non-relativistic first Born approximation, can be written in the form

$$\frac{d^2\sigma}{dWdQ} = \frac{2\pi e^4}{mv^2} \frac{1}{WQ} \frac{df(Q, W)}{dW}. \quad (4.5)$$

The function $df(Q, W)/dW$ is the generalized oscillator strength (GOS), which is described in detail by Inokuti [In71]. The GOS can be represented as a surface over the plane (Q, W) , which is known as the Bethe surface. This surface contains all the relevant information to describe the inelastic collisions of charged particles with the target system under consideration (within the first Born approximation). Unfortunately, the Bethe surface is known in analytical form for only relatively simple systems, namely, the hydrogen atom [In71] and the free-electron gas [Li54,LW64] and, even in these cases, it is too complicated for simulation purposes.

In the limit of very high recoil energies, the binding of the target electrons and their momentum distribution have a negligible effect on the interaction. Hence in the high- Q region, the target electrons behave as if they were both essentially free and at rest and the GOS vanishes except for $W \simeq Q$. The Bethe surface in this region reduces to a ridge along the line $W = Q$, named the Bethe ridge by Inokuti [In71]. For low recoil energies, the details of the Bethe surface are characteristic of the considered target. The GOS for $Q = 0$ reduces to the optical oscillator strength (OOS). Experimental information on the OOS is provided by measurements of either photoelectric cross sections or dielectric functions [Fa63,CH78].

The GOS satisfies the Bethe sum rule [In71]

$$\int_0^\infty \frac{df(Q, W)}{dW} dW = Z, \quad (4.6)$$

irrespective of the value of Q . The mean excitation energy I , which plays the central role in the Bethe stopping power formula (4.2), is given by [Fa63, In71]

$$Z \ln I = \int_0^\infty \ln W \frac{df(Q=0, W)}{dW} dW. \quad (4.7)$$

Except for the shell correction, the non-relativistic Bethe stopping power formula is determined by the integral properties of the GOS expressed by eqs. (4.6) and (4.7). In order to obtain analytical expressions for the collision DCS, it is sensible to consider schematic Bethe surface models which satisfy relations (4.6) and (4.7) in the low- Q region and reduce to $Z\delta(W - Q)$ for large Q values. In the present calculations we adopt a simple GOS model proposed by Liljequist [Li83]. In this model, the response of the target to inelastic collisions is represented by a limited number M of excitations (or oscillators) characterized by excitation energies W_i and oscillator strengths f_i . The Liljequist GOS can be written as

$$\frac{df(Q, W)}{dW} = \sum_{i=1}^M f_i F(W_i; Q, W). \quad (4.8)$$

The excitation spectrum $F(W_i; Q, W)$ of the i th oscillator is assumed to be

$$F(W_i; Q, W) = \delta(W - W_i)\theta(W - Q) + \delta(W - Q)\theta(Q - W), \quad (4.9)$$

where $\delta(x)$ is the Dirac delta function and $\theta(x)$ is the Heaviside step function ($\theta(x) = 0$ if $x < 0$ and $= 1$ if $x \geq 0$). The corresponding OOS reduces to

$$\frac{df(Q=0, W)}{dW} = \sum_{i=1}^M f_i \delta(W - W_i), \quad (4.10)$$

which has the same analytical form as the OOS underlying Sternheimer's calculations of the density effect correction [St52, SP71, SB84].

In order to reproduce the high-energy stopping power given by the Bethe formula (4.2), the excitation energies and oscillator strengths must satisfy the Bethe sum rule (4.6) and lead, through eq. (4.7), to the accepted value of the mean excitation energy I , i.e.

$$\sum f_i = Z, \quad \sum f_i \ln W_i = Z \ln I. \quad (4.11)$$

Liljequist [Li83], and Sternheimer [St52], associated a single oscillator to each atomic shell and set

$$f_i = Z_i \quad \text{and} \quad W_i = aU_i, \quad (4.12)$$

where Z_i is the number of electrons in the i th shell and U_i is their ionization energy. In the case of conductors, the excitations of the conduction band are described through a single oscillator with oscillator strength f_{cb} , equal to the effective number of conduction electrons per atom, and excitation energy W_{cb} . If optical functions or electron energy loss spectra of the material are known and they show a well-defined plasmon line, W_{cb} should be set equal to the plasmon energy. Otherwise, we can simply take f_{cb} as the number of electrons in the target atom that have binding energies less than a few tens of eV and set $W_{cb} = b\Omega_p(f_{cb}/Z)^{1/2}$, where b is a parameter of the order of unity [Li83] and Ω_p is the plasma energy corresponding to the total electron density in the material:

$$\Omega_p^2 = 4\pi\hbar^2 NZe^2/m. \quad (4.13)$$

The semiempirical adjustment factor a in eq. (4.12) was introduced by Sternheimer to obtain agreement with the adopted mean excitation energy and is given by

$$\ln a = (Z - f_{cb})^{-1} \left[Z \ln I - f_{cb} \ln W_{cb} - \sum f_i \ln U_i \right]. \quad (4.14)$$

From simple arguments based on the $\sim W^{-3}$ dependence of the photoelectric cross section it is concluded that a should be of the order of $e^{1/2} = 1.65$ [SB84]. In practical cases a ranges in the interval 1.5–3. The value of the parameter b has no influence on the high-energy stopping power, which is accurately given by the Bethe formula (4.2), but other quantities (such as the mean free path and the low-energy stopping power) are more sensitive to the value of this parameter. Liljequist [Li83, Li85] has suggested the use of additional experimental information to determine the optimal value of b . If such information is not available, we may simply adopt a value of b which leads, through eq. (4.14), to a value of the Sternheimer factor a in the interval 1.5–3. This will usually be a good enough approximation for simulation purposes.

This kind of approach is well suited for the simulation of delta ray emission since the GOS is already split into contributions from the different shells. In reality, there is a transfer of oscillator strength from inner to outer shells so that f_i (i.e. the effective number of electrons in the i th shell) should be smaller (larger) than Z_i for inner (outer) shells (see e.g. ref. [SS80]). Owing to the lack of more accurate estimates for most materials, we shall usually take $f_i = Z_i$.

Excitations with $Q = W$, i.e. those located on the Bethe ridge, nearly correspond to free (binary) collisions and will be referred to as close collisions, in contrast with excitations with $Q < W$ which have a resonance-like character and will be referred to as distant collisions [Bo48]. The energy loss DCS is defined as the integral of the DCS, eq. (4.5), over the kinematically allowed recoil energies. It can be split into contributions from close and distant excitations:

$$\frac{d\sigma}{dW} \equiv \int_{Q_-}^{Q_+} \frac{2\pi e^4}{mv^2} \frac{1}{WQ} \frac{df(Q, W)}{dW} dQ = \frac{d\sigma_c}{dW} + \frac{d\sigma_d}{dW}, \quad (4.15)$$

where Q_{\pm} are given by eq. (A.7). Introducing the GOS, eq. (4.8), the contribution due to close collisions reduces to

$$\frac{d\sigma_c}{dW} = \sum_{i=1}^M f_i \frac{d\sigma_R}{dW} \theta(W - W_i), \quad (4.16)$$

where

$$\frac{d\sigma_R}{dW} \equiv \frac{2\pi e^4}{mv^2} \frac{1}{W^2} \quad (4.17)$$

is the Rutherford cross section for collisions with free electrons at rest. The contribution to the energy loss DCS due to distant collisions is found to be

$$\frac{d\sigma_d}{dW} = \frac{2\pi e^4}{mv^2} \sum_{i=1}^M \frac{f_i}{W_i} \ln \left(\frac{W_i}{Q_-} \right) \delta(W - W_i). \quad (4.18)$$

Relativistic corrections can now be introduced in the theory. To this end we closely follow the treatment of Fano [Fa63]. The relativistic DCS for close collisions is given by eq. (4.16) with the Rutherford DCS replaced by the Born relativistic DCSs for binary collisions with free electrons at rest [RC54]. These latter cross sections are different for electrons and positrons and are given by the Møller [Mo32] and Bhabha [Bh36] formulas respectively. The relativistic DCS for close collisions can then be written in the form

$$\frac{d\sigma_c}{dW} \equiv \frac{2\pi e^4}{mv^2} \sum_{i=1}^M \frac{f_i}{W_i^2} F^{(\pm)}(E, W) \theta(W - W_i) \theta(W_{\max} - W). \quad (4.19)$$

The functions $F^{(\pm)}(E, W)$ are the ratios of the Møller and Bhabha DCSs to the Rutherford DCS and are given by

$$F^{(-)}(E, W) \equiv 1 + \left(\frac{\kappa}{1 - \kappa} \right)^2 - \frac{\kappa}{1 - \kappa} + \left(\frac{\gamma - 1}{\gamma} \right)^2 \left(\kappa^2 + \frac{\kappa}{1 - \kappa} \right) \quad (4.20)$$

for electrons and

$$F^{(+)}(E, W) \equiv 1 - \left(\frac{\gamma - 1}{\gamma}\right)^2 \left\{ \frac{2(\gamma + 1)^2 - 1}{\gamma^2 - 1} \kappa - \frac{\kappa^2}{(\gamma + 1)^2} \right. \\ \left. \times \left[3(\gamma + 1)^2 + 1 - 2\gamma(\gamma - 1)\kappa + (\gamma - 1)^2 \kappa^2 \right] \right\} \quad (4.21)$$

for positrons. Here we have introduced the reduced energy loss κ defined by

$$\kappa \equiv W/E. \quad (4.22)$$

The maximum energy loss is $W_{\max} = E$ ($\kappa_{\max} = 1$) for positrons. In the case of electrons, the projectile (primary electron) and the target are indistinguishable; we consider that the primary is the most energetic electron after the collision and hence the energy loss W cannot exceed half the initial energy E , i.e. $W_{\max} = E/2$ ($\kappa_{\max} = 1/2$).

The relativistic DCS for distant collisions (see eq. (16) in ref. [Fa63]) may be split into a “longitudinal” term, which accounts for the interaction through the static unretarded Coulomb field, and a “transverse” term which arises from the interaction through emission and reabsorption of virtual photons. The longitudinal term is still given approximately by eq. (4.18), but now the proper relativistic expression (A.5) of the minimum recoil energy must be used (together with a small correction introduced into the arguments of the logarithms, cf. eq. (4.31) below). The transverse term, which vanishes in the non-relativistic limit, is strongly influenced by the dielectric properties of the medium where the fast electron moves. In particular, the atomic DCSs for media of the same material but different densities will differ.

4.2.2 Density effect

The usual treatment of the density effect is based on the classical dielectric approach, which leads to results equivalent to those of the Born approximation for low-density materials. The complex dielectric function $\epsilon(W)$ and the OOS are related by [Fa63]

$$\text{Im} \left[\frac{-1}{\epsilon(W)} \right] = \frac{\pi}{2} \frac{\Omega_p^2}{ZW} \frac{df(Q=0, W)}{dW}. \quad (4.23)$$

The energy loss DCS for distant transverse interactions is given by

$$\frac{d\sigma_t}{dW} = \frac{2\pi e^4}{mv^2} \frac{1}{W} \frac{df(Q=0, W)}{dW} \left[\ln \left(\frac{1}{1 - \beta^2} \right) - \beta^2 - \Delta(W) \right]. \quad (4.24)$$

An explicit expression for the quantity $\Delta(W)$ may be derived from eq. (47) in Fano's review with the aid of eq. (4.23). Such an expression is not well suited for numerical evaluation with a discrete OOS model such as eq. (4.10). To avoid this difficulty we simply assume that the density effect reduces the DCS of all the oscillators in the same proportion and accordingly set $\Delta(W)$ equal to δ (the density effect correction to the stopping power, as given by eq. (4.28) below). This approximation will introduce an error in the distant transverse DCSs of the different oscillators (only at high energies) but these errors cancel to give the correct stopping power.

Fano [Fa63] has shown that the density effect correction to the stopping power can be computed as

$$\delta \equiv \frac{1}{Z} \int_0^\infty \frac{df(Q=0, W)}{dW} \ln \left(1 + \frac{L^2}{W^2} \right) dW, \quad (4.25)$$

where L is a real valued function of β^2 defined as the positive root of the following equation (see eq. (9) in Inokuti and Smith's paper [IS82]):

$$1 - \beta^2 \equiv \frac{1}{Z} \Omega_p^2 \int_0^\infty \frac{1}{W^2 + L^2} \frac{df(Q=0, W)}{dW} dW \equiv \mathcal{F}(L). \quad (4.26)$$

The function $\mathcal{F}(L)$ decreases monotonically with L , and hence, the root $L(\beta^2)$ exists only when $1 - \beta^2 < \mathcal{F}(0)$; otherwise it is $\delta = 0$. Therefore, the function $L(\beta^2)$ starts with zero at $\beta^2 = 1 - \mathcal{F}(0)$ and grows monotonically with increasing β^2 . With the OOS, eq. (4.10), we have

$$\mathcal{F}(L) = \frac{1}{Z} \Omega_p^2 \sum_{i=1}^M \frac{f_i}{W_i^2 + L^2} \quad (4.27)$$

and

$$\delta \equiv \frac{1}{Z} \sum_{i=1}^M f_i \ln \left(1 + \frac{L^2}{W_i^2} \right) - \frac{L^2}{\Omega_p^2} (1 - \beta^2). \quad (4.28)$$

The DCS for collisions in dense media can then be calculated as

$$\frac{d\sigma}{dW} \equiv \sum_{i=1}^M f_i \left(\frac{d\sigma_{ci}}{dW} + \frac{d\sigma_{di}}{dW} \right). \quad (4.29)$$

The partial DCS per unit oscillator strength for close collisions with the i th oscillator is given by (see eq. (4.19))

$$\frac{d\sigma_{ci}}{dW} = \frac{2\pi e^4}{mv^2} \frac{1}{W^2} F^{(\pm)}(E, W) \theta(W - W_i) \theta(W_{\max} - W) \quad (4.30)$$

and the corresponding DCS for distant (longitudinal and transverse) interactions is

$$\frac{d\sigma_{di}}{dW} = \frac{2\pi e^4}{mv^2} \frac{1}{W_i} \left[\ln \left(\frac{W_i Q_- + 2mc^2}{Q_- W_i + 2mc^2} \right) + \ln \left(\frac{1}{1 - \beta^2} \right) - \beta^2 - \delta \right] \delta(W - W_i), \quad (4.31)$$

where Q_- is given by eq. (A.5) with $W = W_i$. The argument of the first logarithm differs from the one in eq. (4.18) due to the relativistic correction for the longitudinal term (cf. our eq. (4.5) and eq. (16) in ref. [Fa63]).

Expressions (4.30) and (4.31) allow the random sampling of the energy loss by using purely analytical methods which are described in section 4.4. To specify the event completely, we must also determine the recoil energy Q . The probability distribution function of Q in collisions with a given W is proportional to the corresponding DCS, $d^2\sigma/(dQdW)$, which is considered in detail in ref. [Fa63]. For distant interactions, longitudinal collisions are more probable than transverse ones and the (unnormalized) distribution function of Q is approximately given by (see eqs. (16), (22) and (23) in ref. [Fa63])

$$P_d(Q) = \begin{cases} \frac{1}{Q(1+Q/2mc^2)} & \text{if } Q_- < Q < W, \\ 0 & \text{otherwise.} \end{cases} \quad (4.32)$$

For close collisions, $Q = W$. Once the energy loss and recoil energy have been sampled, the scattering angle can be determined from eq. (A.4).

According to our GOS model, each oscillator W_i corresponds to a shell with f_i electrons and ionization energy U_i . It is then reasonable to assume that in a collision where energy W is transferred to the i th oscillator, a secondary electron or delta ray is emitted with energy $W - U_i$ (W for excitations of the conduction band) in the direction of the momentum transfer \mathbf{q} . We thus have a simple, but still fairly realistic, model for delta ray production.

The mean free path between inelastic collisions is

$$\lambda_c^{-1}(E) \equiv N \int_0^E \frac{d\sigma}{dW} dW. \quad (4.33)$$

Let us consider that an electron, or positron, with initial energy E_0 has travelled a path length s through the medium and has suffered an energy loss $\Delta E = E_0 - E$ ($\ll E$) due to inelastic collisions. We assume that $s \gg \lambda_c(E_0)$ so that the electron has experienced a large number of inelastic collisions along its trajectory. Both the number of collisions and the energy loss in each collision are subjected to statistical fluctuations and hence, the global energy loss ΔE can be considered as a random variable which follows a certain probability distribution function $P(\Delta E)$. The average value $\langle \Delta E \rangle$ and the variance $\text{Var}(\Delta E)$ of this distribution increase with path length. The collision stopping power $S_c(E)$ and energy straggling parameter $\Omega_c^2(E)$ are defined by (see e.g. ref. [FM91])

$$S_c(E) \equiv \frac{d\langle\Delta E\rangle}{ds} = N \int_0^E W \frac{d\sigma}{dW} dW, \quad (4.34)$$

$$\Omega_c^2(E) \equiv \frac{d\text{Var}(\Delta E)}{ds} = N \int_0^E W^2 \frac{d\sigma}{dW} dW. \quad (4.35)$$

It is worth noticing that, with the present model, the mean free path, the stopping power and the straggling parameter can be calculated analytically. The resulting expressions are a bit lengthy but it is very simple to code them in a computer program. In the limit of high kinetic energies, we recover the Bethe formula (4.2) including the density effect correction. The value of this correction practically coincides with the values tabulated by Sternheimer et al. [St52,SP71,SB84], who used a similar oscillator model (with slightly different oscillator strengths and excitation energies). At low energies, our stopping power also accounts approximately for the shell correction.

The results presented here refer to electrons and positrons in aluminium, silver and gold which are representative of low, medium and high atomic number elements. The parameters adopted in the calculations are given in table 4.1. The mean excitation energies I are the ones recommended by Berger and Seltzer [BS84], which are considered to be the most reliable to date. The excitation energy of the conduction band, W_{cb} , has been set approximately equal to the position of the maximum of the OOS determined from the optical dielectric data reported in ref. [Pa85], and the oscillator strength f_{cb} has been obtained as the number of electrons in the outer shells of the atom with binding energies less than or comparable to W_{cb} . For the inner shells we have set $f_i = Z_i$ and adopted the ionization energies given by Bearden and Burr [BB67]. In the case of aluminium, we use the effective numbers of electrons in each shell obtained by Shiles et al. [SS80] from their analysis of experimental dielectric data. These numbers are given in table 4.2 where the transfer of oscillator strength from inner to outer shells is seen.

Table 4.1. Generalized oscillator strength parameters for aluminium, silver and gold. For silver and gold, the adopted values of the oscillator strengths f_i of bound shells are the occupation numbers Z_i . Those of aluminium are given in table 4.2. The ionization energies of bound shells used in the calculations are those given by Bearden and Burr [BB67]. The last column gives the values of Sternheimer's adjustment factor a obtained from eq. (4.14).

Element	Z	I (eV)	f_{cb}	W_{cb} (eV)	Ω_p (eV)	a
Al	13	166	3.1	15.0	32.9	2.62
Ag	47	470	11	30.0	61.6	1.86
Au	79	790	11	40.0	80.2	1.83

Table 4.2. Oscillator strengths and bound shell ionization energies for aluminium. The oscillator strengths f_i are the effective numbers of electrons obtained by Shiles et al. [SS80] from optical data. Bound shell ionization energies are taken from Bearden and Burr [BB67].

Shell	Z_i	f_i	U_i (eV)
1s _{1/2}	2	1.65	1559
2s _{1/2}	2	2.05	117.7
2p _{1/2}	6	6.2	73.2
c.b.	3	3.1	

Collision stopping powers for electrons in aluminium, silver and gold obtained from the present DCSs are compared with sample values from the stopping power tables of Berger and Seltzer [BS84] for $E \geq 10$ keV in fig. 4.1. At these energies, our results practically coincide with the values in the tables of reference, as could be expected from the physical assumptions underlying the present model. Inelastic mean free paths and stopping powers for low-energy electrons ($E = 100$ eV to 100 keV) in aluminium obtained from the present model are compared with experimental data from several authors in fig. 4.2.

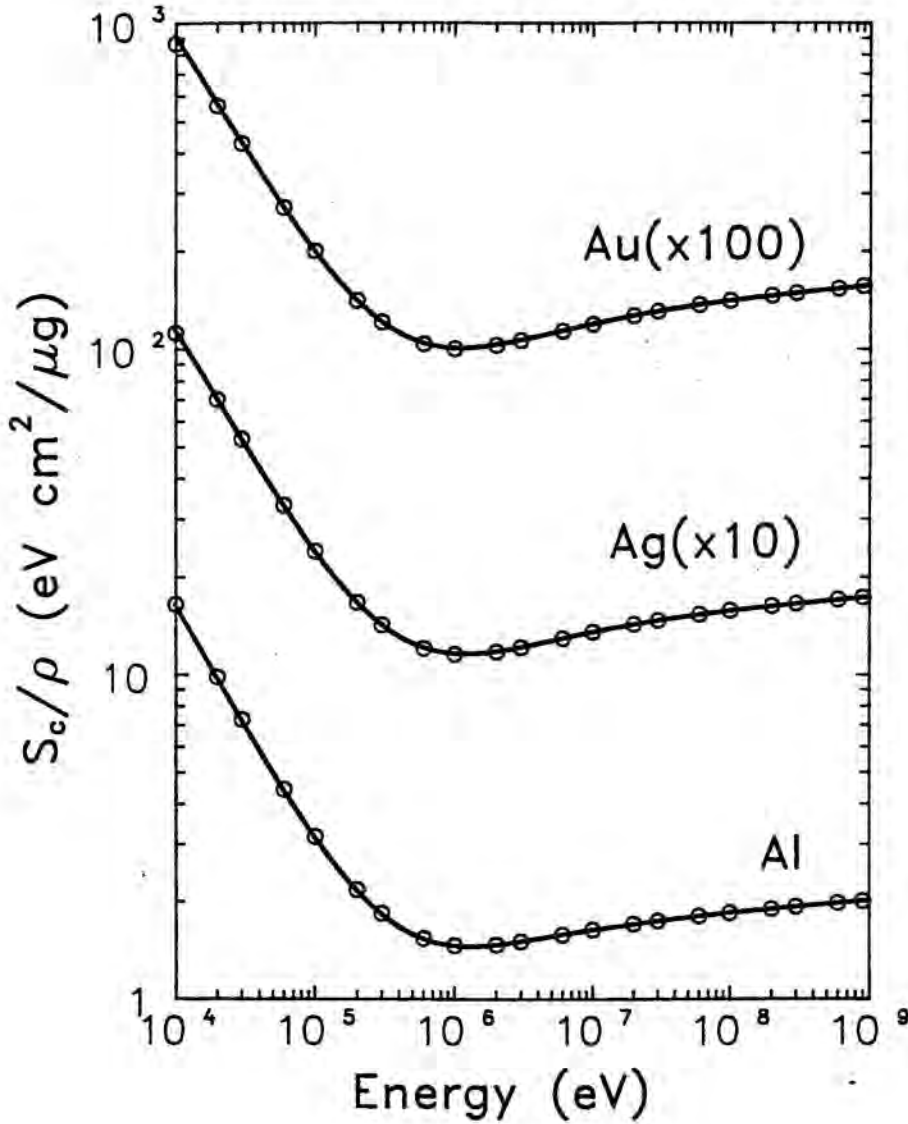


Figure 4.1. Collision stopping power, S_c/ρ (in $\text{eV}/(\mu\text{g}/\text{cm}^2)$), for electrons in aluminium, silver ($\times 10$) and gold ($\times 10^2$) as a function of the kinetic energy. The curves are results from the present model. Circles are values from Berger and Seltzer's tables [BS84].

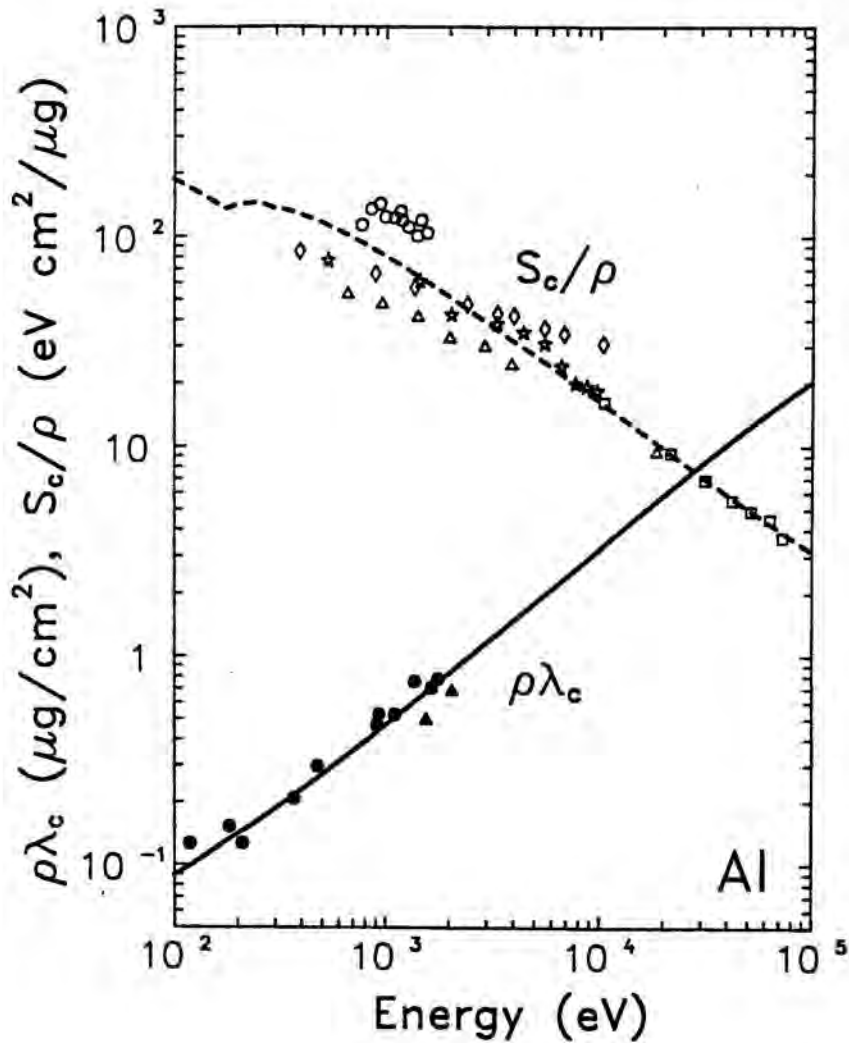


Figure 4.2. Collision mean free path and stopping power for low-energy electrons in aluminium. The plotted curves are $\rho\lambda_c$ (in $\mu\text{g}/\text{cm}^2$, continuous) and S_c/ρ (in $\text{eV}/(\mu\text{g}/\text{cm}^2)$, dashed). Special symbols are experimental data from the following sources (closed symbols for mean free paths and open symbols for stopping powers): (\bullet), ref. [Tr74]; (\blacktriangle), ref. [Ka70]; (\circ), ref. [GH69]; (\square), ref. [Yo56]; (\triangle), ref. [Fi74]; (\square), ref. [KS59]; (\square), ref. [AW83].

Stopping powers of aluminium and silver for positrons obtained from our approach are compared with values from the Berger and Seltzer tables [BS84] in fig. 4.3. For comparison purposes, we have also plotted the stopping powers for electrons computed from the present model. As is well known [RC54], the relative differences between the stopping powers for electrons and positrons are quite small (of the order of a few per cent) for energies above 1 MeV. For kinetic energies below 100 keV, electron stopping powers are smaller and, in the energy range covered in fig. 4.3, the relative differences increase with decreasing energy.

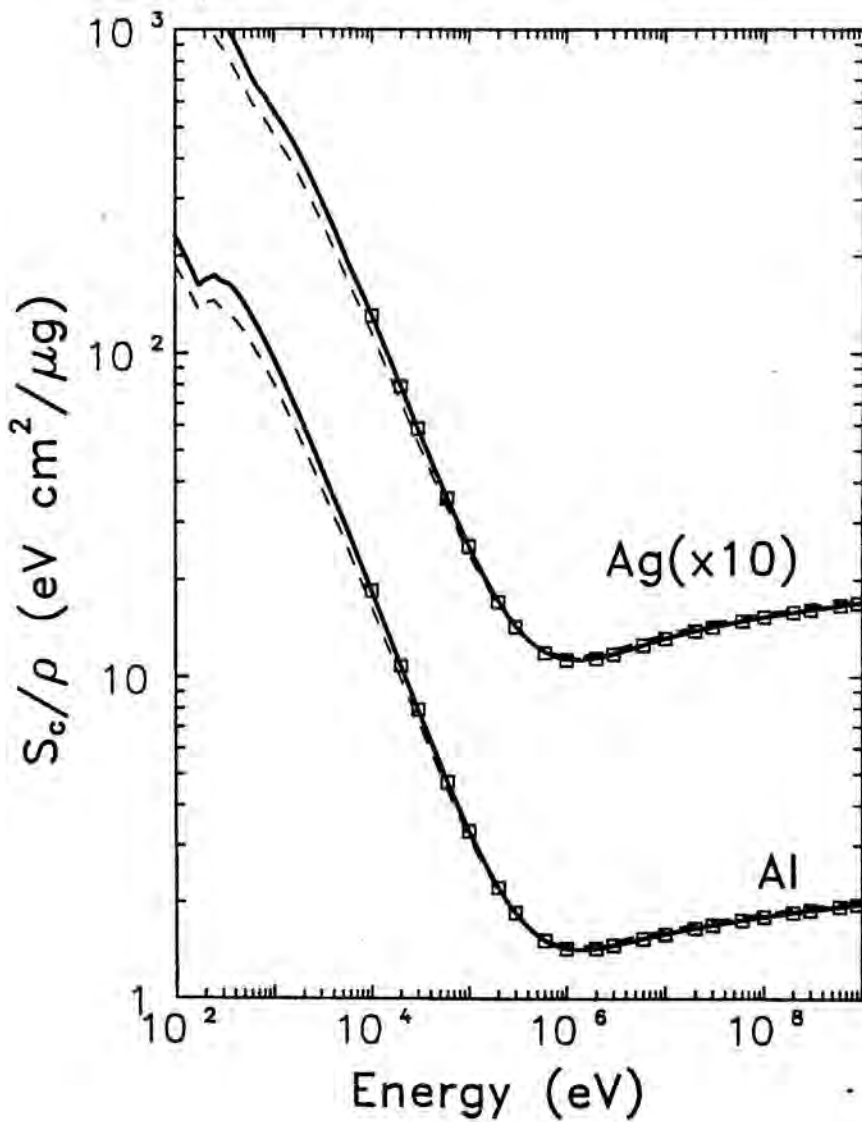


Figure 4.3. Collision stopping power for positrons in aluminium and silver ($\times 10$) as a function of the kinetic energy. The continuous and dashed curves are the results from the present model for positrons and electrons respectively. Squares are values from Berger and Seltzer's tables [BS84] for positrons.

The essential ingredient of our model is the replacement of the actual OOS by a set of oscillators yielding the same stopping power at high energies, which is determined by the integrals of the OOS in eqs. (4.6) and (4.7). The inverse mean free path, eq. (4.33), and the straggling parameter, eq. (4.35), for high-energy electrons are determined by other integral properties of the actual OOS [In71] which are not exactly reproduced by the OOS model and, hence, our estimates of these quantities are less accurate than our stopping powers. To partially overcome this problem, Liljequist [Li85] has suggested the use of several oscillators for each shell so as to mimic the real OOS and Martínez et al. [MM90,SM85] have proposed approximate OOS which are continuous functions of W . Such sophistications may be necessary only under extreme conditions, e.g. to simulate energy loss spectra with very high resolutions such as those used in electron energy loss spectroscopy. In practice, we will usually deal with moderate energy resolutions so that the deficiencies of our model will be washed out when convoluting the simulated spectra with a realistic spectrometer profile.

4.3 Radiative losses

Many theories of the bremsstrahlung process have been developed, each with its own approximations and range of applicability (see e.g. refs. [Ts74,SB85,MO64]). As we are mainly interested in the simulation of electron and positron transport, it is not necessary to account for the angular distribution of the emitted photons; this aspect of the bremsstrahlung process is considered in refs. [BB86,NH85]. In addition, the angular deflections of the electron trajectory due to radiative processes are small and can be neglected. Hence, we disregard any angular dependence of the DCS and concentrate on the simpler problem of determining the dependence of the DCS on only the photon energy.

4.3.1 Bethe-Heitler DCS

Our starting point is the high-energy atomic DCS for arbitrary screening, which was derived by Bethe and Heitler from the Born approximation [BH34]. This DCS is valid whenever the kinetic energy of the electron before and after photon emission is much larger than its rest energy mc^2 . It is convenient to consider the DCS in terms of the

reduced energy ϵ of the emitted photon defined such that

$$\epsilon \equiv \frac{W}{E + mc^2}, \quad (4.36)$$

where, as before, $W = E - E'$ is the energy lost by the electron (i.e. the energy of the emitted bremsstrahlung photon). The maximum reduced energy of the emitted photons is $\epsilon_{\max} \equiv E/(E + mc^2)$. The Bethe-Heitler DCS for electrons can be written in the form (see formula 3CS(b) in ref. [MO64])

$$\frac{d\sigma_{\text{BH}}^{(-)}}{d\epsilon} = a_0^2 \alpha^5 Z [Z + \eta] \frac{1}{\epsilon} \left[(1 + (1 - \epsilon)^2) (\Phi_1 - 4f_C) - \frac{2}{3}(1 - \epsilon)(\Phi_2 - 4f_C) \right], \quad (4.37)$$

where $a_0 = 5.292 \times 10^{-9}$ cm is the Bohr radius and $\alpha \approx 1/137$ is the fine-structure constant. The screening functions Φ_1 and Φ_2 are defined as

$$\Phi_1 \equiv 4 \int_{q_0}^{mc} (q - q_0)^2 [1 - F(q)]^2 \frac{dq}{q^3} + 4, \quad (4.38)$$

$$\Phi_2 \equiv 4 \int_{q_0}^{mc} \left[q^3 - 6qq_0^2 \ln \left(\frac{q}{q_0} \right) + 3qq_0^2 - 4q_0^3 \right] [1 - F(q)]^2 \frac{dq}{q^4} + \frac{10}{3}, \quad (4.39)$$

where q_0 is the minimum momentum transfer which, in the high-energy limit, is given by

$$q_0 = \frac{mc}{2\gamma} \frac{\epsilon}{1 - \epsilon} \quad (4.40)$$

and $F(q)$ is the atomic form factor.

The function f_C is the high-energy Coulomb correction derived by Davies, Bethe and Maximon [DB54]

$$f_C(Z) = a \sum_{n=1}^{\infty} [n(n^2 + a)]^{-1}, \quad a \equiv (\alpha Z)^2. \quad (4.41)$$

This correction is valid only at high energies and, moreover, it has the wrong sign near the tip of the spectrum. From the analysis given by Seltzer and Berger [SB85], it follows that the Coulomb correction should not be used when $E - W$ is less than $\sim 5mc^2$ (see fig. 5 in ref. [SB85]). Consequently we will set $f_C(Z) = 0$ when $W > E - 5mc^2$, i.e. when

$$\epsilon > \epsilon_a \equiv \frac{E - 5mc^2}{E + mc^2}. \quad (4.42)$$

This condition “turns off” the Coulomb correction for $E < 2.5$ MeV and near the tip, where it is no longer applicable. For convenience in computation, expression (4.41) may be rewritten as [DB54]

$$f_C(Z) = a \left[(1 + a)^{-1} + 0.202059 - 0.03693a + 0.00835a^2 - 0.00201a^3 + 0.00049a^4 - 0.00012a^5 + 0.00003a^6 - \dots \right]. \quad (4.43)$$

The quantity η in eq. (4.37) accounts for the production of bremsstrahlung in the field of the atomic electrons and it is considered in detail by Seltzer and Berger [SB85]. For the sake of simplicity, we assume that the dependence of the electron-electron bremsstrahlung DCS on the photon energy is the same as for the screened nuclear DCS, but let η vary with the electron energy. Nelson et al. [NH85] and Brun et al. [BB86] used the same approximation but set η equal to the high-energy limit obtained by Tsai [Ts74] and thus disregarded any variation with energy. Seltzer and Berger [SB85] reported electron-electron bremsstrahlung cross sections for six different elements. By numerical fit of their data we have found that the variation of η with E , averaged over these six elements, may be approximated as

$$\eta(Z, E) \simeq \frac{(E/mc^2)^{0.8}}{(E/mc^2)^{0.8} + 2.43} \eta_\infty(Z), \quad (4.44)$$

where η_∞ is the high-energy limit (see fig. 4.5 below).

To proceed with the derivation of an analytical DCS we must select a suitable approximation for the atomic form factor appearing in eqs. (4.38) and (4.39). Conveniently simple expressions are obtained by using a form factor of the type

$$F(q) = \frac{1}{1 + (Rq/\hbar)^2}, \quad (4.45)$$

which corresponds to exponential screening and is known as the Wentzel form factor [We27]. The screening radius R could be estimated, for instance, from the Thomas-Fermi model of the atom. This procedure was adopted by Schiff [Sc51] (see also ref. [Ts74]). However, it is more expedient to keep R as an adjustable parameter to be determined later from available high-energy data. Integrals (4.38) and (4.39) with the Wentzel form factor of eq. (4.45) can be evaluated analytically and yield the following expressions for the screening functions in the high-energy limit [Ts74]:

$$\Phi_1 = 2 - 2\ln(1 + b^2) - 4b \tan^{-1}(b^{-1}) + 4\ln(Rmc/\hbar), \quad (4.46)$$

$$\begin{aligned} \Phi_2 = & \frac{4}{3} - 2\ln(1 + b^2) + 2b^2 \left[4 - 4b \tan^{-1}(b^{-1}) - 3\ln(1 + b^{-2}) \right] \\ & + 4\ln(Rmc/\hbar), \end{aligned} \quad (4.47)$$

where

$$b \equiv \frac{Rq_0}{\hbar} = \frac{Rmc}{\hbar} \frac{1}{2\gamma^2} \frac{\epsilon}{1 - \epsilon}. \quad (4.48)$$

Bremsstrahlung emission is closely related to electron-positron pair creation (at least within the Born approximation). In particular (see e.g. ref. [NH85]), the high-energy

Bethe-Heitler DCS for a photon of energy E_γ to produce an electron-positron pair in which the electron has a kinetic energy $E = \epsilon E_\gamma - mc^2$ can be written in the form

$$\frac{d\sigma_{\text{BH}}^{(\text{pc})}}{d\epsilon} = a_0^2 \alpha^5 Z[Z + \eta_\infty] \left[(\epsilon^2 + (1 - \epsilon)^2) (\Phi_1 - 4f_C) + \frac{2}{3} \epsilon(1 - \epsilon)(\Phi_2 - 4f_C) \right]. \quad (4.49)$$

For exponential screening, the functions Φ_1 and Φ_2 are given by expressions (4.46) and (4.47) with

$$b \equiv \frac{Rq_0}{\hbar} = \frac{Rmc}{\hbar} \frac{mc^2}{2E_\gamma} \frac{1}{\epsilon(1 - \epsilon)}. \quad (4.50)$$

Extensive tables of pair-production total cross sections, evaluated from accurate atomic form factors, have been published by Hubbell et al. [HG80]. These tables give the separate contributions from pair creation in the field of the nucleus and in that of the atomic electrons for $Z=1$ to $Z=100$ and for photon energies from threshold up to 10^5 MeV. In the present work, we have taken advantage of these tables and have determined the screening radius R and the electron contribution parameter η_∞ so that the pair-production cross sections of Hubbell et al. [HG80] for 10^5 MeV photons (after exclusion of radiative corrections, which only amount to about 1% of the pair-production cross section) are exactly reproduced by eq. (4.49). The values of R and η_∞ so obtained are given in graphical form in figs. 4.4 and 4.5. The screening radii in fig. 4.4 may be compared with the value $R = 0.81 Z^{-1/3} a_0$ derived by Schiff [Sc51] from high-energy DCSs with Thomas-Fermi screening.

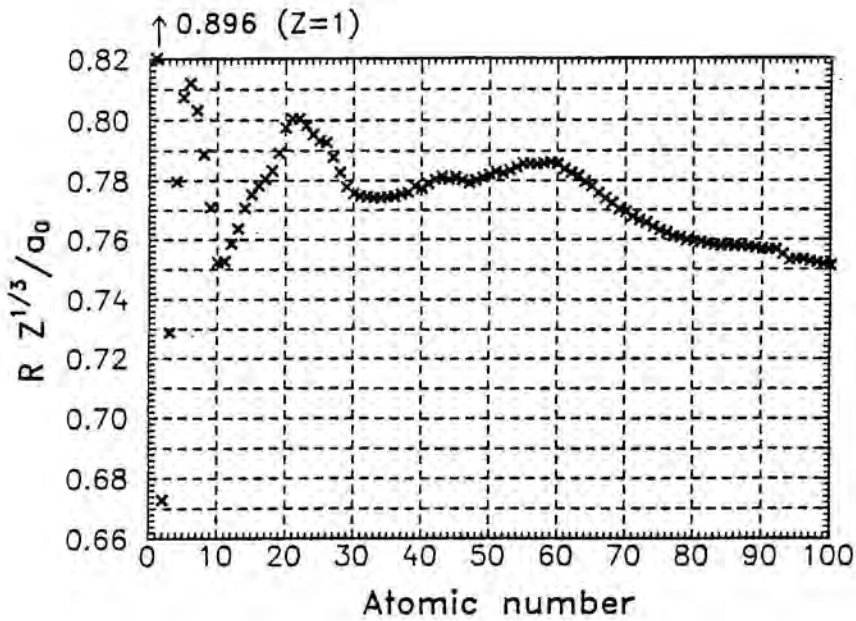


Figure 4.4. Screening radius (in units of $Z^{-1/3}a_0$) for bremsstrahlung emission as a function of the atomic number.

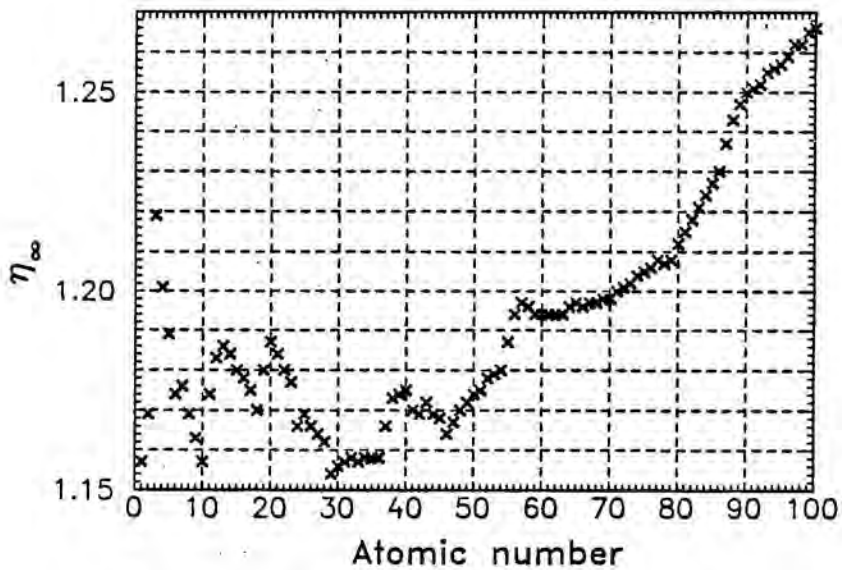


Figure 4.5. High-energy contribution of electron-electron bremsstrahlung to the Bethe-Heitler DCS determined as explained in the text.

To facilitate the random sampling of the energy loss W , the Bethe-Heitler DCS, eq. (4.37), with the Wentzel form factor and including a low-energy correction described below, is written in the form

$$\frac{d\sigma_{\text{BHW}}^{(-)}}{d\epsilon} = a_0^2 \alpha^5 Z[Z + \eta] \left(\varphi_1(\epsilon)\epsilon + \varphi_2(\epsilon)\frac{1}{\epsilon} \right), \quad (4.51)$$

where

$$\begin{aligned} \varphi_1(\epsilon) &= f_1(b) + f_0(\epsilon), \\ \varphi_2(\epsilon) &= \frac{4}{3}(1 - \epsilon) [f_2(b) + f_0(\epsilon)], \end{aligned} \quad (4.52)$$

with

$$f_0(\epsilon) \equiv 4 \ln(Rmc/\hbar) + F_2(Z, E) - 4f_C \theta(\epsilon_d - \epsilon), \quad (4.53)$$

$$f_1(b) \equiv \Phi_1 - 4 \ln(Rmc/\hbar) = 2 - 2 \ln(1 + b^2) - 4b \tan^{-1}(b^{-1}), \quad (4.54)$$

$$\begin{aligned} f_2(b) &\equiv \frac{1}{2}(3\Phi_1 - \Phi_2) - 4 \ln(Rmc/\hbar) \\ &= \frac{7}{3} - 2 \ln(1 + b^2) - 6b \tan^{-1}(b^{-1}) \\ &\quad - b^2 [4 - 4b \tan^{-1}(b^{-1}) - 3 \ln(1 + b^{-2})]. \end{aligned} \quad (4.55)$$

ϵ_d , the cutoff energy loss for the Coulomb correction, is defined by eq. (4.42) and $F_2(Z, E)$ is the aforesaid low-energy correction.

The Born approximation fails at low energies, where it systematically underestimates the DCS. The term $F_2(Z, E)$ in eq. (4.53) has been introduced to compensate for this fact. Al-Beteri and Raeside [AR89] have proposed a semiempirical formula, obtained through a fit of experimental DCS data, which contains a term with the same role. Such a term serves to eliminate another undesirable feature of the DCS, eq. (4.51), namely, that it becomes negative for some values of ϵ . In the present work we use the following correction term:

$$F_2(Z, E) = (2.04 + 9.09\alpha Z) \left(\frac{m^2 c^4}{E(E + mc^2)} \right)^{(1.26 - 0.93\alpha Z)}, \quad (4.56)$$

where the numerical parameters have been determined by fitting the radiative stopping power data of Berger and Seltzer [BS84, SB85] for $E > 50$ keV.

The total cross section for bremsstrahlung emission is infinite due to the divergence of the DCS for small reduced photon energies. Nevertheless, the cross section for

emission of photons with reduced energy larger than a given cutoff value W_c is finite. The corresponding mean free path is

$$\lambda_r^{-1}(E; W_c) \equiv N \int_{\epsilon_c}^{\epsilon_{\max}} \frac{d\sigma_{\text{BHW}}^{(-)}}{d\epsilon} d\epsilon, \quad (4.57)$$

where $\epsilon_c = W_c/(E + mc^2)$. The radiative stopping power and the energy straggling parameter,

$$S_r(E) \equiv N(E + mc^2) \int_0^{\epsilon_{\max}} \epsilon \frac{d\sigma_{\text{BHW}}^{(-)}}{d\epsilon} d\epsilon, \quad (4.58)$$

$$\Omega_r^2(E) \equiv N(E + mc^2)^2 \int_0^{\epsilon_{\max}} \epsilon^2 \frac{d\sigma_{\text{BHW}}^{(-)}}{d\epsilon} d\epsilon, \quad (4.59)$$

are both finite. The numerical evaluation of these quantities solely requires a single quadrature. The results presented below have been calculated by using the 20-point Gauss method, complemented with a bipartition procedure to allow for error control, with a relative accuracy of 10^{-4} .

The “scaled” Bethe-Heitler-Wentzel DCSs, $(\beta/Z)^2 W d\sigma_{\text{BHW}}^{(-)}/dW$, for aluminium and uranium and electrons with $E = 1, 10$ and 100 MeV are compared with the values given by Seltzer and Berger [SB85] in figs. 4.6 and 4.7. The effect of the Coulomb correction is clearly shown by the discontinuity in the DCS for 10 and 100 MeV electrons in uranium. In the vicinity of this discontinuity, the Bethe-Heitler-Wentzel DCS still provides a fairly good approximation. The modification introduced by the low-energy correction $F_2(Z, E)$ is indicated in fig. 4.7 for 1 and 10 MeV electrons. The effect of this correction is a global shift of the scaled DCS to higher values, which clearly improves the DCS. Differences between the present DCSs and those of Seltzer and Berger are significant only for energies near and below 1 MeV.

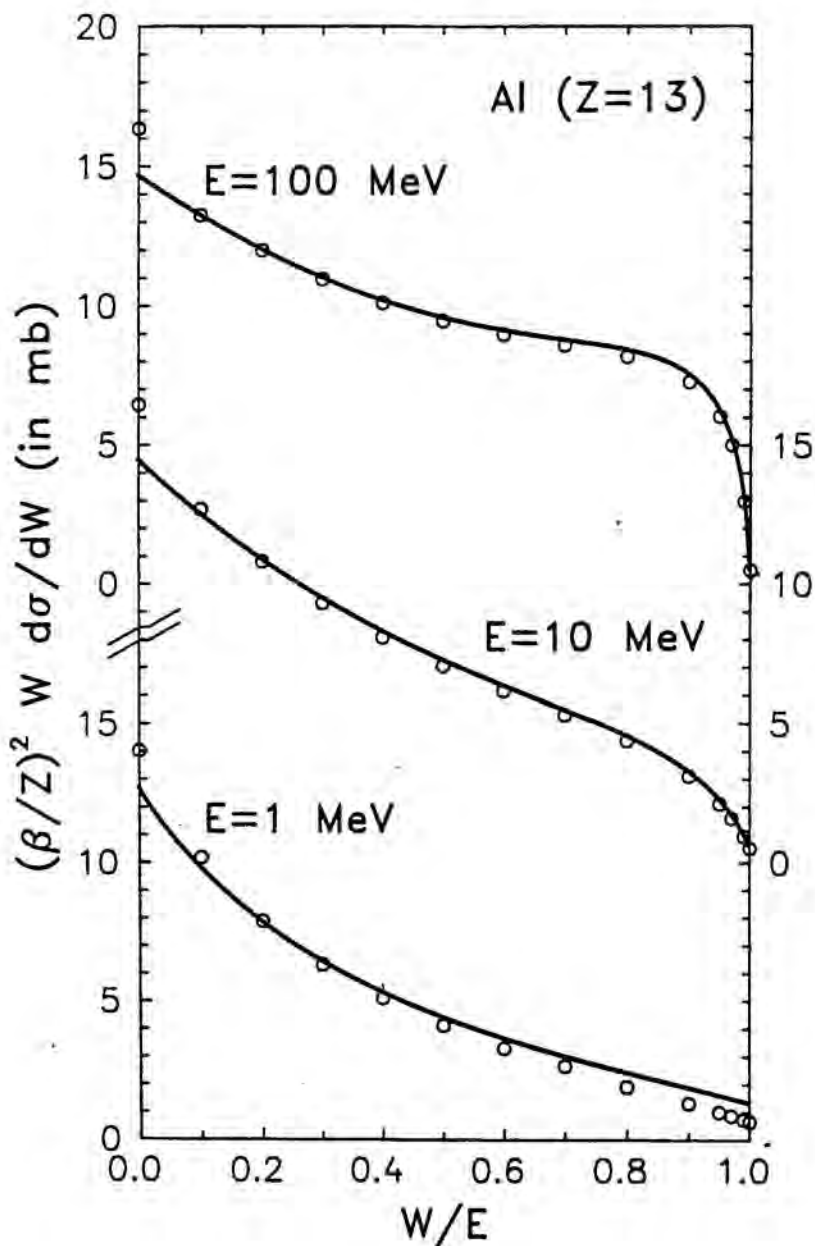


Figure 4.6. Scaled bremsstrahlung DCSs, $(\beta/Z)^2 W d\sigma_{\text{BHW}}^{(-)}/dW$ (in millibarn = 10^{-27} cm²), for aluminium and electrons with $E = 1, 10$ and 100 MeV. The continuous curves are the Bethe-Heitler-Wentzel DCSs, eq. (4.51). Circles are data from Seltzer and Berger's tables [SB85]. Notice that the scale for each curve is the closest to its lettering.

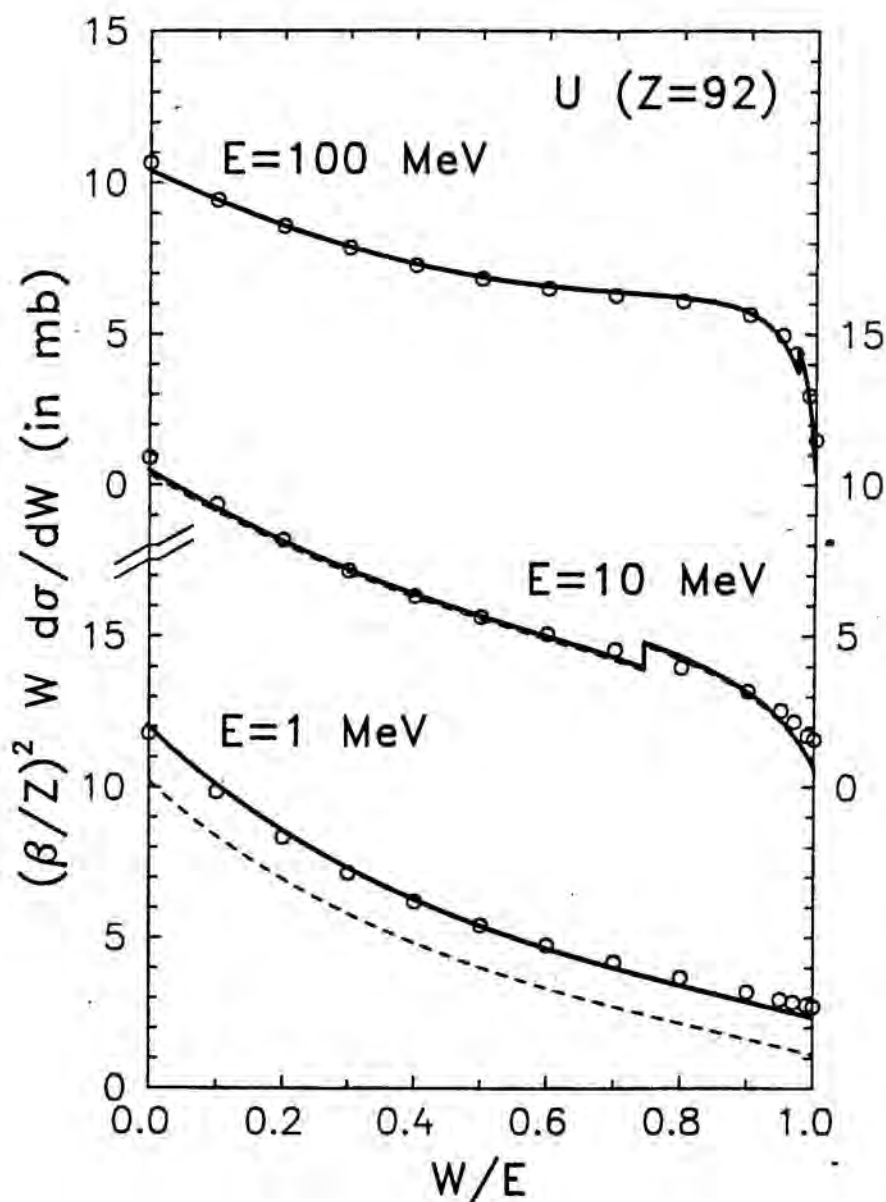


Figure 4.7. Scaled bremsstrahlung DCSs for uranium and electrons with $E = 1, 10$ and 100 MeV. Details are the same as in fig. 4.6. The dashed curves for $E = 1$ and 10 MeV are the Bethe-Heitler-Wentzel DCSs, eq. (4.51), without the low-energy correction, i.e. with $F_2(Z, E) = 0$. The discontinuity of the DCS originates from the Coulomb correction.

Radiative stopping powers of aluminium, silver and gold for electrons are shown as functions of the kinetic energy in fig. 4.8, which also includes the values given in the tables of Berger and Seltzer [BS84]. It is seen that stopping powers computed from the Bethe-Heitler-Wentzel DCS, eq. (4.51), are in good agreement with the Berger and Seltzer values for energies above 50 keV. For energies of the order of 100 MeV and larger, the relative differences between our stopping powers and those of ref. [BS84] are smaller than 1%.

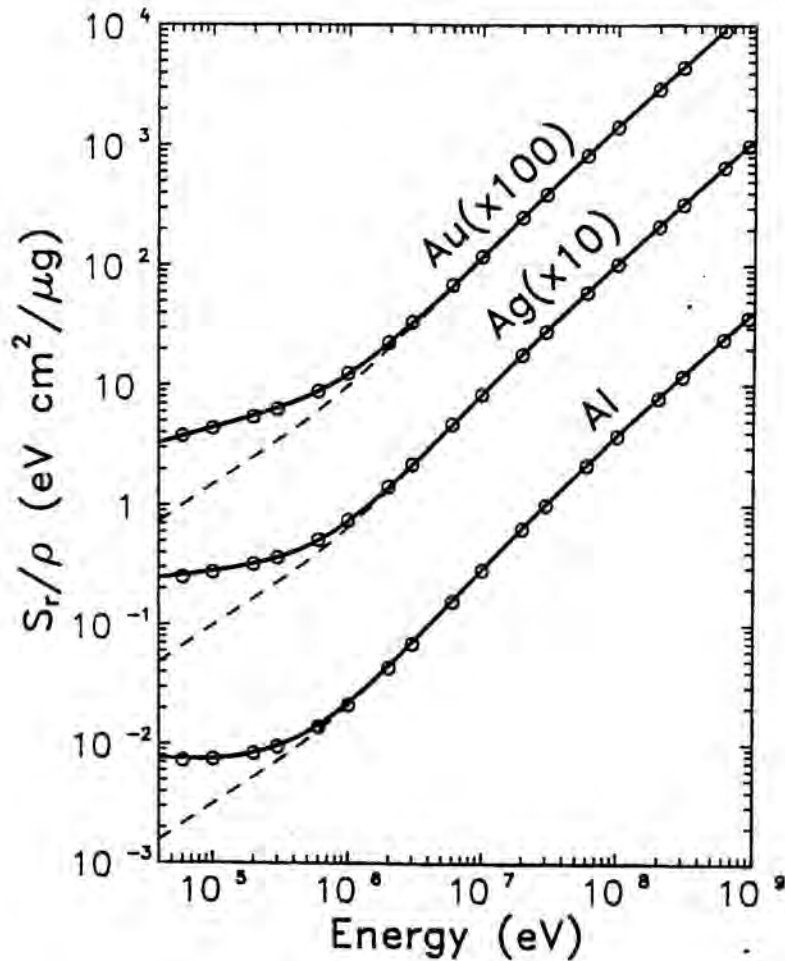


Figure 4.8. Radiative stopping power, S_r/ρ (in $\text{eV}/(\mu\text{g}/\text{cm}^2)$), for electrons in aluminium, silver ($\times 10$) and gold ($\times 10^2$) as a function of the kinetic energy. The continuous and dashed curves are results from the present model, with and without the low-energy correction $F_2(Z, E)$ respectively. Circles are values from Berger and Seltzer's tables [BS84].

For energies below ~ 1 MeV, the present DCSs are not very accurate. However, they are still useful for simulation purposes since, for these energies, the radiative stopping power becomes much smaller than the collision contribution (cf. figs. 4.1 and 4.8). When more reliable values of the radiative stopping power are available (e.g. from ref. [BS84]), the accuracy of our model could be somewhat improved by simply renormalizing the Bethe-Heitler-Wentzel DCS to reproduce these stopping powers.

The DCS for positrons reduces to that of electrons in the high-energy limit, but it is smaller for intermediate and low energies. According to Kim et al. [KP86], the DCS for positrons can be obtained by introducing a simple correction factor in the Bethe-Heitler-Wentzel DCS (for electrons):

$$\frac{d\sigma_{\text{BHW}}^{(+)}}{d\epsilon} = F_p(Z, E) \frac{d\sigma_{\text{BHW}}^{(-)}}{d\epsilon}. \quad (4.60)$$

The function $F_p(Z, E)$ can be estimated by interpolation from the table of values given in ref. [KP86]. In the calculations we use the following approximation:

$$F_p(Z, E) = 1 - \exp(-0.0993t + 0.0144t^2 - 0.00316t^3), \quad (4.61)$$

where

$$t = \ln \left(1 + \frac{10^6 E}{Z^2 mc^2} \right), \quad (4.62)$$

which reproduces the values of the table to an accuracy of about 1%. Radiative stopping powers of aluminium and silver for electrons and positrons are plotted in fig. 4.9, together with values from Berger and Seltzer's tables [BS84].

The usual practice in Monte Carlo simulations is to consider an energy loss threshold W_c for hard bremsstrahlung emission of the order of a few keV or smaller. The photons emitted in soft events are then assumed to be locally absorbed and only the emission of photons with energy higher than W_c is simulated in a detailed way. Soft events can then be treated with the continuous slowing down approximation, preferably modified to include an approximate description of the corresponding energy straggling. The random sampling of the energy of hard bremsstrahlung photons can be performed analytically (see below), and the restricted stopping power and straggling parameter due to soft photon emission ($\epsilon < \epsilon_c$) can also be computed easily.

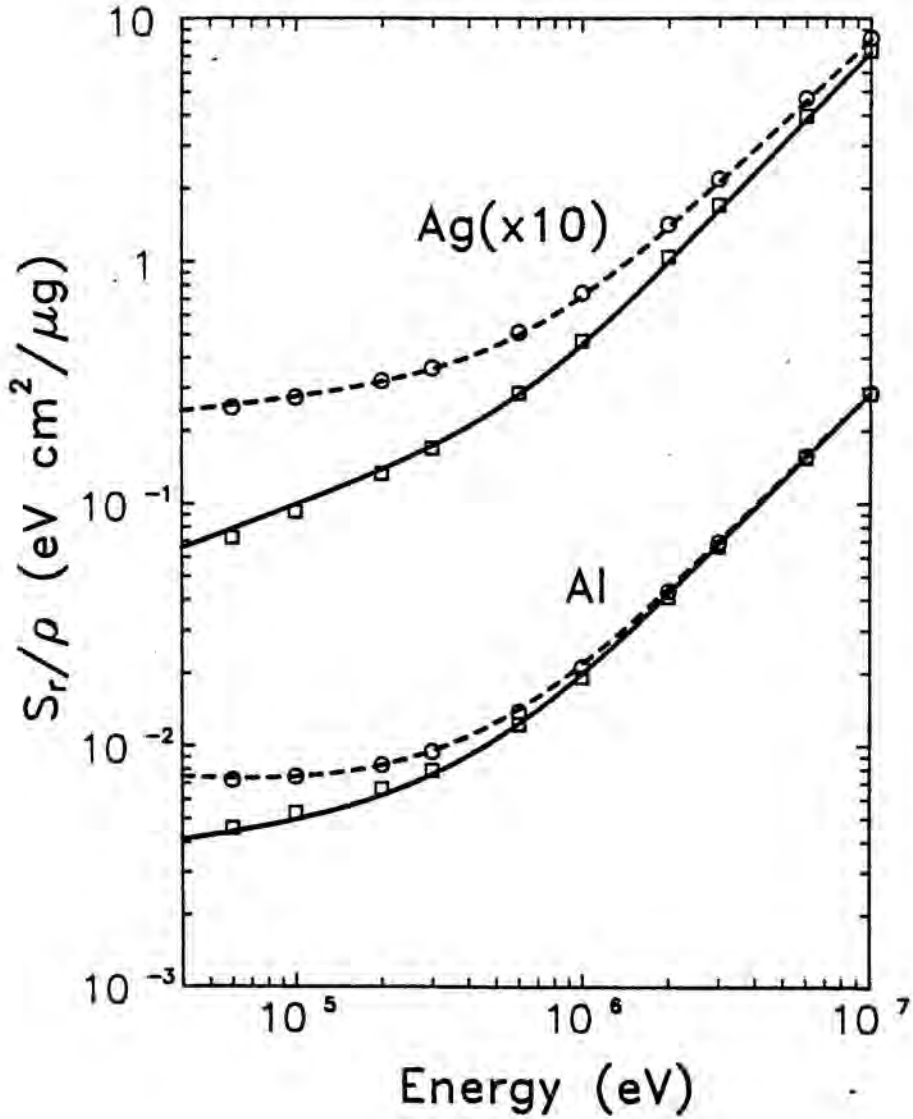


Figure 4.9. Radiative stopping power for positrons and electrons in aluminium and silver ($\times 10$) as a function of the kinetic energy. The continuous and dashed curves are the results from the present model for positrons and electrons respectively. Circles and squares are values from Berger and Seltzer's tables [BS84].

4.4 Random sampling algorithms

One important advantage of the present DCSs is that they permit the random sampling of the energy loss W in hard events ($W > W_c$) by using purely analytical methods. This feature is of great value in reducing both memory requirements and numerical uncertainties in the Monte Carlo simulations. The sampling algorithms described here are based on the composition and acceptance-rejection methods [Ru81,KW86]. Similar procedures, for simpler or less versatile DCSs, have previously been proposed by several authors [BB86,NH85]. In what follows ξ stands for a pseudorandom number uniformly distributed in the interval (0,1).

4.4.1 Energy loss in electron hard collisions

Let us consider the collisions of electrons with the i th oscillator. Notice that the energy loss in distant collisions is $W = W_i$ (see eq. (4.31)), and hence, we only need to consider close collisions. The probability distribution function (PDF) of the reduced energy loss $\kappa \equiv W/E$ in close collisions is given by (see eqs. (4.30) and (4.20))

$$P_{cc}^{(-)}(\kappa) = \kappa^{-2} F^{(-)}(E, W) \theta(\kappa - \kappa_c) \theta\left(\frac{1}{2} - \kappa\right), \quad (4.63)$$

with $\kappa_c \equiv \max(W_i, W_c)/E$. Here, normalization is irrelevant.

We introduce the distribution

$$\Phi^{(-)}(\kappa) \equiv (\kappa^{-2} + 5a) \theta(\kappa - \kappa_c) \theta\left(\frac{1}{2} - \kappa\right), \quad a \equiv \left(\frac{\gamma - 1}{\gamma}\right)^2. \quad (4.64)$$

It may be shown that $\Phi^{(-)} > P_{cc}^{(-)}$ in the interval $(\kappa_c, \frac{1}{2})$. Therefore, we can sample the reduced energy loss κ from the PDF, eq. (4.63), by using the acceptance-rejection method with trial values sampled from the distribution of eq. (4.64) and acceptance probability $P_{cc}^{(-)}/\Phi^{(-)}$.

Random sampling from the PDF, eq. (4.64), can be performed by using the composition method [Ru81]. We consider the following decomposition of the (normalized) PDF, eq. (4.64):

$$\Phi_{\text{norm}}^{(-)}(\kappa) = \frac{1}{1 + 5a\kappa_c/2} [p_1(\kappa) + (5a\kappa_c/2)p_2(\kappa)], \quad (4.65)$$

where

$$p_1(\kappa) = \frac{\kappa_c}{1 - 2\kappa_c} \kappa^{-2}, \quad p_2(\kappa) = \frac{2}{1 - 2\kappa_c} \quad (4.66)$$

are normalized PDFs in the interval $(\kappa_c, \frac{1}{2})$. Random values of κ from the PDF, eq. (4.65), can be generated by using the following algorithm:

1. Sample ξ .
2. Set $\zeta = (1 + 5a\kappa_c/2)\xi$.
3. If $\zeta < 1$, deliver the value $\kappa = \kappa_c/[1 - \zeta(1 - 2\kappa_c)]$.
4. If $\zeta > 1$, deliver the value $\kappa = \kappa_c + (\zeta - 1)(1 - 2\kappa_c)/(5a\kappa_c)$.

The rejection algorithm for random sampling of κ from the PDF, eq. (4.63), proceeds as follows:

1. Sample κ from eq. (4.65).
2. Generate ξ .
3. If $\xi(1 + 5a\kappa^2) < \kappa^2 P_{cc}(\kappa)$, deliver κ .
4. Go to step 1.

Notice that, in the third step, we accept the κ value with probability $P_{cc}^{(-)}/\Phi^{(-)}$, which approaches unity when κ is small.

The efficiency of this method, i.e. the probability of accepting the value of κ in each trial, depends on the values of the kinetic energy and the cutoff reduced energy loss κ_c , as shown in table 4.3. Notice that, for a given energy and for not too large values of W_c , efficiency increases when W_c decreases.

Table 4.3. Efficiency (%) of the random sampling algorithm of the energy loss in close collisions of electrons and positrons, for different values of the kinetic energy and the cutoff energy loss κ_c .

E (eV)	κ_c				
	0.001	0.01	0.1	0.25	0.4
10^3	99.9	99.9	99.8	99.7	99.6
10^5	99.7	98	87	77	70
10^7	99	93	70	59	59
10^9	99	93	71	62	63

4.4.2 Energy loss in positron hard collisions

To sample the energy loss in positron hard collisions, we use the algorithm described in ref. [BB86] for generating random values from the Bhabha DCS. Here, however, excitations of different shells (oscillators) are treated separately. The PDF of the reduced energy loss $\kappa \equiv W/E$ in close collisions with the i th oscillator is given by (see eqs. (4.30) and (4.21))

$$P_{cc}^{(+)}(\kappa) = \kappa^{-2} F^{(+)}(E, W) \theta(\kappa - \kappa_c) \theta(1 - \kappa), \quad (4.67)$$

with $\kappa_c \equiv \max(W_i, W_c)/E$ as before. Again, normalization is not important.

Consider the distribution

$$\Phi^{(+)}(\kappa) \equiv \kappa^{-2} \theta(\kappa - \kappa_c) \theta(1 - \kappa). \quad (4.68)$$

It is easy to see that $\Phi^{(+)} > P_{cc}^{(+)}$ in the interval $(\kappa_c, 1)$. Therefore, we can sample κ from the PDF, eq. (4.67), by using the acceptance-rejection method with trial values sampled from the distribution of eq. (4.68) and acceptance probability $P_{cc}^{(+)}/\Phi^{(+)}$. Sampling from the PDF $\Phi^{(+)}$ can be easily performed with the inverse transform method [Ru81].

The algorithm for random sampling from the PDF, eq. (4.67), is:

1. Sample κ from the PDF, eq. (4.68), as $\kappa = \kappa_c/[1 - \xi(1 - \kappa_c)]$.
2. Generate a new random number ξ .
3. If $\xi < \kappa^2 P_{cc}^{(+)}(\kappa)$, deliver κ .
4. Go to step 1.

The efficiency of this algorithm, for given values of the kinetic energy and the cutoff reduced energy loss κ_c , practically coincides with that of the algorithm for electron collisions described above, i.e. table 4.3 is also applicable to positrons.

4.4.3 Energy loss in hard photon bremsstrahlung emission

The PDF for the reduced energy loss $\epsilon \equiv W/(E+mc^2)$ in hard bremsstrahlung processes is given by (see eq. (4.51))

$$P_r(\epsilon) = \left[\varphi_1(\epsilon)\epsilon + \varphi_2(\epsilon)\frac{1}{\epsilon} \right] \theta(\epsilon - \epsilon_c) \theta(\epsilon_{\max} - \epsilon), \quad (4.69)$$

where $\epsilon_{\max} \equiv E/(E+mc^2)$. Normalization is again irrelevant. Notice that the functions $\varphi_i(\epsilon)$, ($i=1,2$) attain their maximum values at ϵ_c or ϵ_d (see eq. (4.42)).

The distribution of eq. (4.69) can be rewritten in the form

$$P_r(\epsilon) = a_1 F_1(\epsilon) \pi_1(\epsilon) + a_2 F_2(\epsilon) \pi_2(\epsilon), \quad (4.70)$$

where

$$\begin{aligned} a_1 &= \frac{1}{2} (\epsilon_{\max}^2 - \epsilon_c^2) \varphi_{1,\max}, & a_2 &= \ln(\epsilon_{\max}/\epsilon_c) \varphi_{2,\max}, \\ F_1(\epsilon) &= \varphi_1(\epsilon)/\varphi_{1,\max}, & F_2(\epsilon) &= \varphi_2(\epsilon)/\varphi_{2,\max}, \\ \pi_1(\epsilon) &= \frac{2}{\epsilon_{\max}^2 - \epsilon_c^2} \epsilon, & \pi_2(\epsilon) &= \frac{1}{\ln(\epsilon_{\max}/\epsilon_c)} \frac{1}{\epsilon}, \end{aligned} \quad (4.71)$$

and

$$\varphi_{i,\max} = \begin{cases} \max\{\varphi_i(\epsilon_c), \varphi_i(\epsilon_d)\} & \text{if } \epsilon_d > \epsilon_c, \\ \varphi_i(\epsilon_c) & \text{if } \epsilon_d \leq \epsilon_c. \end{cases} \quad (4.72)$$

The functions $\pi_i(\epsilon)$ are normalized PDFs in the interval $(\epsilon_c, \epsilon_{\max})$. Random values of ϵ can be easily sampled from these distributions by using the inverse transform method. In the interval $(\epsilon_c, \epsilon_{\max})$, the values of the functions $F_i(\epsilon)$ are positive and less than unity, i.e. they are valid rejection functions. The generation of random values of ϵ according to the PDF, eq. (4.70), can then be carried out by combining the composition and rejection methods [BB86,NH85]. The algorithm to sample ϵ proceeds as follows.

1. Sample the value of the integer i ($=1,2$) according to the discrete probabilities $p(1) = a_1/(a_1 + a_2)$ and $p(2) = a_2/(a_1 + a_2)$.
2. Sample ϵ from $\pi_i(\epsilon)$ according to the formulas (inverse transform method):

$$\epsilon = \begin{cases} [\epsilon_c^2 + \xi (\epsilon_{\max}^2 - \epsilon_c^2)]^{1/2} & \text{if } i=1, \\ \epsilon_c (\epsilon_{\max}/\epsilon_c)^\xi & \text{if } i=2. \end{cases} \quad (4.73)$$

3. Generate a new random number ξ .
4. If $\xi < F_i(\epsilon)$, deliver ϵ .
5. Go to step 1.

The efficiency of this algorithm depends on the values of E and ϵ_c and, for a given energy and a value of ϵ_c which is not too large, it increases when ϵ_c decreases (see table 4.4). In practical simulations, efficiencies of about 90% may be obtained by using a value of the cutoff energy W_c of the order of a few keV.

Table 4.4. Efficiency (%) of the random sampling algorithm of the photon energy in hard bremsstrahlung emission for electrons and positrons, in gold for different values of the kinetic energy and the cutoff photon energy ϵ_c .

E (eV)	ϵ_c				
	10^{-6}	10^{-4}	0.01	0.1	0.5
10^5	97	96	92	89	92
10^7	91	87	75	63	58
10^9	93	89	81	72	74

4.5 Soft energy loss events

The scattering model described in the previous sections can be directly used in detailed Monte Carlo simulations of electron transport. However, at high energies, the number of scattering events in a particle track is enormous so that detailed simulation is not feasible. The majority of the high-energy simulation codes currently available use condensed Monte Carlo schemes which take advantage of multiple scattering theories to avoid the detailed simulation of all the scattering events.

For the present purposes, it is convenient to classify the energy loss events into “hard” and “soft” events, according to the magnitude of the energy loss W . To this end we introduce cutoff energies W_{cc} and W_{cr} which delimit the energy loss intervals corresponding to soft and hard events for collision and radiative losses respectively. These cutoff energies can be arbitrarily selected. It is evident that, by using large enough values of W_{cc} and W_{cr} , the number of hard events per particle track can be made small enough to permit their detailed simulation.

The stopping power and the energy straggling parameter due to soft events are given by

$$S_s(E) \equiv N \int_0^{W_{cc}} W \frac{d\sigma_{col}(W)}{dW} dW + N \int_0^{W_{cr}} W \frac{d\sigma_{rad}(W)}{dW} dW \quad (4.74)$$

and

$$\Omega_s^2(E) \equiv N \int_0^{W_{cc}} W^2 \frac{d\sigma_{col}(W)}{dW} dW + N \int_0^{W_{cr}} W^2 \frac{d\sigma_{rad}(W)}{dW} dW, \quad (4.75)$$

where “col” and “rad” stand for collision and bremsstrahlung emission respectively.

In the existing high-energy simulation codes (see e.g. refs. [NH85, BB86, IL86]), soft energy loss processes are described with the continuous slowing down approximation,

i.e. the energy loss due to soft events in a path length s is obtained as $S_s(E)s$ and energy straggling is neglected. This approach is well justified when the energy straggling due to these processes is negligible as it happens when the cutoff energies W_{cc} and W_{cr} are both small so that the fraction of the stopping power due to soft collisions is also small. As a rule of thumb, this method leads to accurate energy distributions only when the average number of hard inelastic events is "statistically sufficient" [NH85], i.e. a few tens along each track in the considered medium. To improve the description of energy straggling one should reduce the cutoff energies, but this enlarges the number of hard inelastic events to be simulated along each track and hence the simulation time increases.

The DCSs described in the previous sections yield analytical expressions for the restricted stopping power and energy straggling parameter due to soft collisions. Knowledge of this latter quantity opens up the possibility of accounting for the energy straggling effect due to soft events, thus going beyond the continuous slowing down approximation in the description of soft processes. This is an important point, since then one could considerably increase the cutoff energies W_{cc} and W_{cr} , and hence reduce the simulation time, without distorting the energy distribution.

Let us consider that an electron or positron travels a length s in a medium where it loses energy only through soft processes. We assume that the average energy loss $S_s(E)s$ is much less than the initial energy E . Let $F(W; s)$ denote the probability distribution function of the energy loss W after the path length s ; this distribution can be approximated as a function of the stopping power $S_s(E)$ and the straggling parameter $\Omega_s^2(E)$ by using the standard method described in the references [La44, BL50]. $F(W; s)$ satisfies the following transport equation [La44]

$$\frac{\partial F(W; s)}{\partial s} = N \int_0^\infty [F(W - W'; s) - F(W; s)] \frac{d\sigma_{\text{soft}}(W')}{dW'} dW' \quad (4.76)$$

with the initial value $F(W; 0) = \delta(W)$. Here, $d\sigma_{\text{soft}}/dW$ stands for the DCS for soft processes (inelastic collisions and bremsstrahlung emission). The solution of this integral equation may be obtained by taking the Fourier transform with respect to W

$$\hat{F}(\omega; s) \equiv \int_{-\infty}^\infty \exp(-i\omega W) F(W; s) dW. \quad (4.77)$$

Eq. (4.76) transforms to

$$\frac{\partial \hat{F}(\omega; s)}{\partial s} = \hat{F}(\omega; s) N \int_0^\infty [\exp(-i\omega W') - 1] \frac{d\sigma_{\text{soft}}(W')}{dW'} dW' \equiv -\hat{F}(\omega; s) g(\omega) \quad (4.78)$$

with $\hat{F}(\omega; 0) = 1$. It follows that

$$\hat{F}(\omega; s) = \exp[-g(\omega)s] \quad (4.79)$$

and, taking the inverse Fourier transform,

$$F(W; s) = \frac{1}{2\pi} \int_{-\infty}^{\infty} \exp[i\omega W - g(\omega)s] d\omega. \quad (4.80)$$

As only comparatively small energy losses are involved in each single event, we may expand the exponential in

$$g(\omega) = N \int_0^{\infty} [1 - \exp(-i\omega W')] \frac{d\sigma_{\text{soft}}(W')}{dW'} dW' \quad (4.81)$$

and write this function in terms of the moments of the DCS $d\sigma_{\text{soft}}/dW$, i.e.

$$g(\omega) = -N \sum_{n=1}^{\infty} \frac{(-i\omega)^n}{n!} \int_0^{\infty} W^n \frac{d\sigma_{\text{soft}}(W)}{dW} dW. \quad (4.82)$$

Now, we proceed as in the Blunck and Leisegang theory [BL50] and neglect the terms in the series eq. (4.82) with $n > 2$. This leads to

$$g(\omega) \simeq N \left(iS_s(E)\omega + \frac{1}{2}\Omega_s^2(E)\omega^2 \right). \quad (4.83)$$

As long as we are only considering low energy loss processes, this approximation is well justified (notice that this is not the case when dealing with soft and hard processes together). Introducing eq. (4.83) in eq. (4.80) and using the convolution theorem, it is easily seen that the resulting $F(W; s)$ distribution is

$$F(W; s) = \delta(W - S_s s) \otimes \mathcal{N}(0, \Omega_s^2 s) = \mathcal{N}(S_s s, \Omega_s^2 s), \quad (4.84)$$

where $\mathcal{N}(\mu, \sigma^2)$ stands for the normal distribution with mean μ and variance σ^2 . It is worth noting that the energy loss distribution in the continuous slowing down approximation is $\delta(W - S_s s)$. When energy straggling is included, the energy loss distribution eq. (4.84) results from the convolution of the continuous slowing down approximation distribution and a normal distribution with mean zero and variance $\Omega_s^2 s$. Thus the straggling parameter Ω_s^2 gives the increase of variance per unit path length due to soft processes.

The energy loss distribution will be accurately given by eq. (4.84) only if: 1) the average energy loss $S_s s$ is small enough for the DCS $d\sigma_{\text{soft}}/dW$ to be nearly constant in the path length s and 2) the approximation eq. (4.83) holds. This last requirement implies

that the cutoff energies W_{cc} and W_{cr} for delta ray production and photon emission have to be relatively small, otherwise, the actual distribution of soft energy losses after a given path length may depart substantially from the gaussian profile. In practice, the distribution eq. (4.84) approaches the actual distribution when its mean value $S_s s$ is much smaller than the initial energy E and its standard deviation $(\Omega_s^2 s)^{1/2}$ is much smaller than $S_s t$ (otherwise there is a finite probability of negative energy losses). Both conditions are satisfied for path lengths s such that

$$\Omega_s^2 / S_s \ll S_s s \ll E. \quad (4.85)$$

4.6 Conclusions

We have presented approximate analytical formulas for the collision and radiative DCSs suitable for use as the basis of Monte Carlo simulation of electron and positron transport. The reliability of these DCSs has been analyzed and algorithms for their implementation have been described.

The range of validity of the collision DCS is much wider than for previous approaches. The collision stopping power is accurate for energies down to a few hundred eV. Mean free paths are also predicted to a reasonable accuracy and the same is expected for other integrals of the DCS (e.g. the energy straggling parameter). The basic parameter in the DCS is the mean excitation energy for which we have used the values given by Berger and Seltzer [BS84]. Of course, if more accurate values of the mean excitation energy become available in the future, the DCS could be updated by simply introducing these values. The main limitation of our collision model lies in the discrete nature of the OOS, which has direct consequences on the fine details of the simulated energy loss spectrum. In particular, our DCSs should not be used to simulate highly resolved energy spectra where the details of the OOS may become prominent.

The Bethe-Heitler-Wentzel DCS, eq. (4.51), provides a reliable description of bremsstrahlung emission for electrons and positrons with kinetic energies above a few MeV. For lower energies, the renormalization procedure based on available stopping powers can be used to improve it. As the contribution of radiative losses to the global stopping power is very small at these energies, the present approach meets all the requirements of a general purpose simulation.

The random sampling algorithms proposed here are purely analytical and, thus, they

are virtually exact. Furthermore, only the parameters which determine the DCS have to be stored during the simulation. The efficiencies of these algorithms increase when the threshold energy W_c decreases (except when W_c takes anomalously large values), and eventually approach unity.

Conclusions

Partial wave DCSs for elastic scattering of electrons and positrons by screened Coulomb fields have been calculated for projectiles with kinetic energies up to ~ 20 MeV and 20 elements. These accurate DCSs have been used to derive a formula that allows the calculation of elastic scattering data needed for Monte Carlo simulation. This formula, which includes finite nuclear size effects, is valid for electrons and positrons with kinetic energies larger than about Z keV.

A new Monte Carlo algorithm to simulate multiple elastic scattering, which overcomes most of the limitations of the currently used algorithms, has been described. This algorithm may be applied to any single scattering law and leads to simulation results that are essentially identical to the exact solution of the transport equation. When combined with a Wentzel DCS, the simulation procedure may be stated in a completely analytical form. Simulation with a Wentzel model yields angular distributions as accurate as those obtained from the theory of Molière, and spatial distributions more accurate than those obtained from existing Monte Carlo codes based on this theory.

Inelastic scattering of low-energy electrons in solids has been considered on the basis of an optical-data model that includes exchange effects through a modified Ochkur approximation. Our calculations reveal a certain dependence of the calculated mean free paths and stopping power on the extrapolation algorithm.

Inelastic collisions of high-energy electrons and positrons are described by using the Born approximation on the basis of a simple generalized oscillator strength model. Our approach also accounts for the so-called shell corrections and Sternheimer's density effect correction. Bremsstrahlung emission has been described by a modified Bethe-Heitler formula which includes screening effects, the Coulomb correction and a low-energy correction. These differential cross sections allow the random sampling of the energy loss and the scattering angle in each inelastic or radiative event in an analytical

way.

Appendix A

Legendre functions of the second kind

The transport coefficients for the Wentzel differential cross section, eq. (2.23), can be expressed in terms of the Legendre functions of the second kind $Q_\ell(x)$ [AS74] as

$$\begin{aligned} G_\ell^{(W)} &= 1 - 2A(1+A) \int_{-1}^1 \frac{P_\ell(\cos \chi)}{(2A+1-\cos \chi)^2} d(\cos \chi) \\ &= 1 - \ell [Q_{\ell-1}(1+2A) - (1+2A)Q_\ell(1+2A)]. \end{aligned} \quad (\text{A.1})$$

This important result follows from eq. (7.228) in ref. [GR80] and from the properties of the Legendre functions.

The simplest method to evaluate the Legendre functions of the second kind is to use their recurrence relation

$$(\ell+1)Q_{\ell+1}(x) - (2\ell+1)xQ_\ell(x) + \ell Q_{\ell-1}(x) = 0. \quad (\text{A.2})$$

For $x < 1$, $Q_\ell(x)$ can be generated starting from

$$Q_0(x) = \frac{1}{2} \ln \left| \frac{x+1}{x-1} \right|, \quad Q_1(x) = x \frac{1}{2} \ln \left| \frac{x+1}{x-1} \right| - 1 \quad (\text{A.3})$$

and applying eq. (A.2) for increasing values of ℓ . However, for $x > 1$, the recurrence relation (A.2) should be used only for decreasing values of ℓ to avoid the loss of significant figures [AS74].

A convenient method to compute all the $Q_\ell(x)$ for $x > 1$ takes advantage of the relation

$$Q_\ell(x) \simeq K_0[\ell \cosh^{-1}(x)] \quad (\text{A.4})$$

which holds asymptotically for large ℓ ; here K_0 stands for the modified Bessel function. Using eq. (A.4) we can estimate the values of $Q_L(x)$ and $Q_{L-1}(x)$ where L is a large enough value for eq. (A.4) to be approximately valid, but not much larger than $80/\cosh^{-1}(x)$ to avoid computer underflows. Approximate values of $Q_\ell(x)$ for $\ell = 0, 1, \dots, L-2$ are then generated by applying eq. (A.2) for decreasing values of ℓ . Let $\bar{Q}_\ell(x)$ denote these quantities. Accurate values of $Q_\ell(x)$ are finally obtained as

$$Q_\ell(x) = \bar{Q}_\ell(x)Q_0(x)/\bar{Q}_0(x). \quad (\text{A.5})$$

Let us set $x = 1 + 2A$ with $A > 0$, and consider the case $A \ll 1$. From the relation [..]

$$Q_\ell(x) = \frac{1}{2}P_\ell(x) \ln \left(\frac{x+1}{x-1} \right) - \sum_{m=1}^{\ell} \frac{1}{m} P_{m-1}(x) P_{\ell-m}(x) \quad (\text{A.6})$$

and the limiting form of the Legendre polynomials [..]

$$P_\ell(1+2A) = 1 + \ell(\ell+1)A + O(\ell^4 A^2) \quad (\text{A.7})$$

it follows that

$$Q_\ell(1+2A) = [1 + \ell(\ell+1)A] \left[\frac{1}{2} \ln \left(\frac{1+A}{A} \right) - \Phi(\ell) \right] + \ell(\ell+1)A + O(\ell^4 A^2), \quad (\text{A.8})$$

where

$$\Phi(\ell) \equiv \sum_{m=1}^{\ell} \frac{1}{m}. \quad (\text{A.9})$$

Introducing the result (A.8), the expression (A.1) simplifies to

$$G_\ell^{(W)} = \ell(\ell+1)A \left[\ln \left(\frac{1+A}{A} \right) - 2\Phi(\ell) + 1 \right] + O(\ell^4 A^2). \quad (\text{A.10})$$

which holds asymptotically for large ℓ ; here K_0 stands for the modified Bessel function. Using eq. (A.4) we can estimate the values of $Q_L(x)$ and $Q_{L-1}(x)$ where L is a large enough value for eq. (A.4) to be approximately valid, but not much larger than $80/\cosh^{-1}(x)$ to avoid computer underflows. Approximate values of $Q_\ell(x)$ for $\ell = 0, 1, \dots, L-2$ are then generated by applying eq. (A.2) for decreasing values of ℓ . Let $\bar{Q}_\ell(x)$ denote these quantities. Accurate values of $Q_\ell(x)$ are finally obtained as

$$Q_\ell(x) = \bar{Q}_\ell(x)Q_0(x)/\bar{Q}_0(x). \quad (\text{A.5})$$

Let us set $x = 1 + 2A$ with $A > 0$, and consider the case $A \ll 1$. From the relation [..]

$$Q_\ell(x) = \frac{1}{2}P_\ell(x) \ln \left(\frac{x+1}{x-1} \right) - \sum_{m=1}^{\ell} \frac{1}{m} P_{m-1}(x) P_{\ell-m}(x) \quad (\text{A.6})$$

and the limiting form of the Legendre polynomials [..]

$$P_\ell(1+2A) = 1 + \ell(\ell+1)A + \mathcal{O}(\ell^4 A^2) \quad (\text{A.7})$$

it follows that

$$Q_\ell(1+2A) = [1 + \ell(\ell+1)A] \left[\frac{1}{2} \ln \left(\frac{1+A}{A} \right) - \Phi(\ell) \right] + \ell(\ell+1)A + \mathcal{O}(\ell^4 A^2), \quad (\text{A.8})$$

where

$$\Phi(\ell) \equiv \sum_{m=1}^{\ell} \frac{1}{m}. \quad (\text{A.9})$$

Introducing the result (A.8), the expression (A.1) simplifies to

$$G_\ell^{(W)} = \ell(\ell+1)A \left[\ln \left(\frac{1+A}{A} \right) - 2\Phi(\ell) + 1 \right] + \mathcal{O}(\ell^4 A^2). \quad (\text{A.10})$$

Appendix B

Random sampling of angular reflections in artificial soft collisions

To simulate the angular deflection in artificial soft collisions we must generate random values of $\mu = (1 - \cos \theta)/2$ in the interval $(0,1)$ from a distribution $p_s(\mu)$ satisfying the conditions given by eqs. (2.90), i.e. the mean $\langle \mu \rangle$ and variance $\text{var}(\mu) = \langle \mu^2 \rangle - \langle \mu \rangle^2$ of this distribution are fixed by the step length and may take quite arbitrary values. Moreover, it is necessary that random values of μ may be generated in a simple and fast way. Standard distributions, such as the beta distribution [AS74], are not adequate since available sampling algorithms are too involved [Ru81]. A distribution that meets our needs was described in a previous work [FM91]; it is given by

$$p_s(\mu) = \begin{cases} \frac{1}{\alpha} \frac{1 - \langle \mu \rangle}{\langle \mu \rangle} \left(\frac{\mu}{\langle \mu \rangle} \right)^{(1-\alpha)/\alpha} & \text{if } \mu \leq \langle \mu \rangle \\ \frac{1}{\alpha} \frac{\langle \mu \rangle}{1 - \langle \mu \rangle} \left(\frac{1 - \mu}{1 - \langle \mu \rangle} \right)^{(1-\alpha)/\alpha} & \text{if } \mu > \langle \mu \rangle \end{cases} \quad (\text{B.1})$$

with $\alpha \geq 0$. This distribution already satisfies the conditions

$$\int_0^1 p_s(\mu) d\mu = 1 \quad \text{and} \quad \int_0^1 \mu p_s(\mu) d\mu = \langle \mu \rangle \quad (\text{B.2})$$

irrespective of the value of the parameter α . This parameter is determined by requiring that

$$\int_0^1 \mu^2 p_s(\mu) d\mu = \langle \mu^2 \rangle. \quad (\text{B.3})$$

From this last condition it follows that

$$\alpha = \frac{3a + [a(a+8)]^{1/2}}{4(1-a)} \quad \text{with} \quad a \equiv \frac{\text{var}(\mu)}{\langle \mu \rangle(1 - \langle \mu \rangle)}. \quad (\text{B.4})$$

Random values of μ distributed according to $p_s(\mu)$ can be easily generated by using the inverse transform method [Ru81], i.e. each new value of μ is obtained as the unique root of the equation

$$\int_0^\mu p_s(\mu') d\mu' = \xi \quad (\text{B.5})$$

where ξ is a pseudo-random number uniformly distributed in the interval (0,1). This equation can be solved analytically and yields the following sampling formula

$$\mu = \begin{cases} \langle \mu \rangle [\xi / (1 - \langle \mu \rangle)]^\alpha & \text{if } \xi < 1 - \langle \mu \rangle \\ 1 - (1 - \langle \mu \rangle) [(1 - \xi) / \langle \mu \rangle]^\alpha & \text{if } \xi \geq 1 - \langle \mu \rangle \end{cases} \quad (\text{B.6})$$

Appendix C

Folding Theorem

Let us assume that a particle moves in a medium where it can undergo elastic collisions of two different types, say a and b , with single-scattering angular distributions $f^{(a)}(\theta)$ and $f^{(b)}(\theta)$ respectively. For instance, these distributions may correspond to scattering by two different kind of atoms or to soft and hard collisions. Now consider that a particle, which initially moves in the direction $\theta = 0$, suffers a collision of type a and a collision of type b . After the two collisions, the probability of finding the particle moving in a direction in the solid angle $d\Omega$ about the direction θ, ϕ is given by

$$f^{(a,b)}(\theta) d\Omega = \int_0^\pi \int_0^{2\pi} f^{(a)}(\theta_1) f^{(b)}(\theta_2) \sin \theta_1 d\theta_1 d\phi_1 d\Omega \quad (\text{C.1})$$

with

$$\cos \theta_2 = \cos \theta \cos \theta_1 + \sin \theta \sin \theta_1 \cos(\phi_1 - \phi) \quad (\text{C.2})$$

The distribution $f^{(a,b)}$ is said to be the result of “folding” the distributions $f^{(a)}$ and $f^{(b)}$. This operation will be denoted by the symbol \otimes ,

$$f^{(a,b)} \equiv f^{(a)} \otimes f^{(b)}. \quad (\text{C.3})$$

Consider that the single-scattering distributions are expanded in the form of Legendre series

$$f^{(a)}(\theta) = (4\pi)^{-1} \sum_{\ell=0}^{\infty} (2\ell + 1) f_\ell^{(a)} P_\ell(\cos \theta) \quad (\text{C.4a})$$

and

$$f^{(b)}(\theta) = (4\pi)^{-1} \sum_{\ell=0}^{\infty} (2\ell + 1) f_\ell^{(b)} P_\ell(\cos \theta) \quad (\text{C.4b})$$

Using the addition theorem for spherical harmonics [Ar70].

$$P_\ell(\cos \theta_2) = P_\ell(\cos \theta)P_\ell(\cos \theta_1) + 2 \sum_{m=1}^{\ell} P_\ell^m(\cos \theta)P_\ell^m(\cos \theta_1) \cos [m(\phi - \phi_1)] \quad (\text{C.5})$$

and the orthogonality of the Legendre functions, the integral in eq. (C.1) is easily evaluated and directly leads to

$$f^{(a,b)}(\theta) = (4\pi)^{-1} \sum_{\ell=0}^{\infty} (2\ell + 1) f_\ell^{(a)} f_\ell^{(b)} P_\ell(\cos \theta) \quad (\text{C.6})$$

i.e. the coefficients of the Legendre expansion of the resulting distribution are related to those of the folded single scattering distributions through

$$f_\ell^{(a,b)} = f_\ell^{(a)} f_\ell^{(b)}. \quad (\text{C.7})$$

This result constitutes the folding theorem, which is the key stone of the Goudsmit-Saunderson multiple scattering theory. From the folding theorem it follows that the order in which the collisions a and b occur is irrelevant, i.e. $f^{(a)} \otimes f^{(b)} = f^{(b)} \otimes f^{(a)}$.

In practical Monte Carlo simulations, the folding of distributions corresponding to successive collisions is performed by successively rotating the direction vector $\hat{\mathbf{d}} \equiv (d_x, d_y, d_z)$, whose coordinates are the direction cosines. The rotation matrix $R(\chi, \phi)$ of each collision is determined by the polar and azimuthal scattering angles, which are randomly sampled from the pertinent distribution. Let θ and φ denote the polar and azimuthal angles of the initial direction

$$\hat{\mathbf{d}} = (\sin \theta \cos \varphi, \sin \theta \sin \varphi, \cos \theta). \quad (\text{C.8})$$

To obtain explicitly the direction vector $\hat{\mathbf{d}}' = R(\chi, \phi)\hat{\mathbf{d}}$ after the collision, we first note that, if the initial direction is along the z -axis, the direction after the collision is

$$\begin{pmatrix} \sin \chi \cos \phi \\ \sin \chi \sin \phi \\ \cos \chi \end{pmatrix} = R_z(\phi)R_y(\chi)\hat{\mathbf{z}} \quad (\text{C.9})$$

where $\hat{\mathbf{z}}=(0,0,1)$ and

$$R_y(\chi) = \begin{pmatrix} \cos \chi & 0 & \sin \chi \\ 0 & 1 & 0 \\ -\sin \chi & 0 & \cos \chi \end{pmatrix} \quad \text{and} \quad R_z(\phi) = \begin{pmatrix} \cos \phi & -\sin \phi & 0 \\ \sin \phi & \cos \phi & 0 \\ 0 & 0 & 1 \end{pmatrix} \quad (\text{C.10})$$

are rotation matrices corresponding to rotations of angles χ and ϕ about the y - and z -axis respectively. On the other hand, the rotation $R_y(-\theta)R_z(-\varphi)$ transforms the vector $\hat{\mathbf{d}}$ into $\hat{\mathbf{z}}$. It is then clear that the final direction vector $\hat{\mathbf{d}}'$ can be obtained by performing the following sequence of rotations of the initial direction vector: 1) $R_y(-\theta)R_z(-\varphi)$, which transforms $\hat{\mathbf{d}}$ into $\hat{\mathbf{z}}$; 2) $R_x(\phi)R_y(\chi)$, which rotates $\hat{\mathbf{z}}$ according to the sampled polar and azimuthal scattering angles; and 3) $R_x(\varphi)R_y(\theta)$, which inverts the rotation of the first step. Hence

$$R(\chi, \phi) = R_x(\varphi)R_y(\theta)R_x(\phi)R_y(\chi)R_y(-\theta)R_z(-\varphi). \quad (\text{C.11})$$

The final direction vector is

$$\hat{\mathbf{d}}' = R(\chi, \phi)\hat{\mathbf{d}} = R_x(\varphi)R_y(\theta) \begin{pmatrix} \sin \chi \cos \phi \\ \sin \chi \sin \phi \\ \cos \chi \end{pmatrix} \quad (\text{C.12})$$

and its direction cosines are

$$d'_x = d_x \cos \chi + \frac{\sin \chi}{\sqrt{1 - d_z^2}} [d_x d_z \cos \phi - d_y \sin \phi], \quad (\text{C.13a})$$

$$d'_y = d_y \cos \chi + \frac{\sin \chi}{\sqrt{1 - d_z^2}} [d_y d_z \cos \phi + d_x \sin \phi], \quad (\text{C.13b})$$

$$d'_z = d_z \cos \chi - \sqrt{1 - d_z^2} \sin \chi \cos \phi \quad (\text{C.13c})$$

These equations are not very stable numerically and the normalization of $\hat{\mathbf{d}}'$ tends to drift from 1 after repeated usage. This must be remedied by periodically renormalizing $\hat{\mathbf{d}}'$. Moreover, eqs. (C.13) become indeterminate when $d_z \simeq 1$, i.e. when the initial direction is nearly parallel to the z -axis. This may be overcome by cyclic permutation of the x , y and z -axis.

Appendix D

Useful kinematic relations

The kinetic energy E and the momentum \mathbf{p} of an electron or positron are related by

$$E = [(cp)^2 + m^2c^4]^{1/2} - mc^2, \quad (\text{D.1})$$

where m is the electron rest mass and c is the speed of light in vacuum. It is convenient to introduce the usual quantities

$$\gamma \equiv 1 + E/mc^2, \quad \beta \equiv (\gamma^2 - 1)^{1/2}/\gamma = v/c, \quad (\text{D.2})$$

where v is the velocity of the particle. We have

$$E = (\gamma - 1)mc^2, \quad p = \gamma m\beta c. \quad (\text{D.3})$$

Inelastic collisions are determined by the scattering angle θ and the energy loss W . Let \mathbf{p} and E be the momentum and the kinetic energy of the electron just before the collision, the corresponding quantities after the collision are denoted by \mathbf{p}' and $E' = E - W$ respectively. Evidently, the maximum energy loss is $W = E$. The momentum transfer in the collision is $\mathbf{q} \equiv \mathbf{p} - \mathbf{p}'$. It is customary to introduce the recoil energy Q defined by [Fa63]

$$Q(Q + 2mc^2) = (cq)^2 = c^2(p^2 + p'^2 - 2pp' \cos \theta), \quad (\text{D.4})$$

which, in the particular case where the collision is with a free electron at rest, coincides with the recoil energy of the target electron after the collision, i.e. $Q = W$ (if the projectile is an electron we consider it as distinguishable from the target electron).

The kinematically allowed recoil energies are those in the interval $Q_- \leq Q \leq Q_+$ with end points given by eq. (D.4) with $\cos \theta = \pm 1$:

$$\begin{aligned} Q_{\pm} &= \left[c^2(p \pm p')^2 + m^2 c^4 \right]^{1/2} - mc^2 \\ &= \left\{ \left[(E(E + 2mc^2))^{1/2} \right. \right. \\ &\quad \left. \left. \pm ((E - W)(E - W + 2mc^2))^{1/2} \right]^2 + m^2 c^4 \right\}^{1/2} - mc^2. \end{aligned} \quad (\text{D.5})$$

Notice that $Q_+ > W$. When $W \ll E$, the expression for Q_- is unsuitable for numerical evaluation since it involves the subtraction of two similar quantities. In this case it is more convenient to use the approximation

$$Q_- \simeq \frac{W^2}{2\beta^2 mc^2}. \quad (\text{D.6})$$

Finally, we quote the non-relativistic limits of these relations:

$$Q \equiv q^2/2m, \quad Q_{\pm} = \left[E^{1/2} \pm (E - W)^{1/2} \right]^2. \quad (\text{D.7})$$

References

- [AG85] A.F. Akkerman and A.L. Gibrekhterman, *Nucl. Instr. and Meth.* **B6** (1985) 496.
- [Ah80] S.P. Ahlen, *Rev. Mod. Phys.* **52** (1980) 121.
- [AM91] M. Abou Mandour and D. Harder, *Nucl. Instr. and Meth.* **A300** (1991) 403.
- [An91] P. Andreo, *Phys. Med. Biol.* **36** (1991) 861.
- [Ar70] G. Arfken, *Mathematical Methods for Physicists* (Academic Press, New York, 1970).
- [AR89] A.A. Al-Beteri and D.E. Raeside, *Nucl. Instr. and Meth.* **B44** (1989) 149.
- [AS74] M. Abramowitz and I. Stegun, *Handbook of Mathematical Functions* (Dover, New York, 1974).
- [As82] J.C. Ashley, *J. Electr. Spectr. Rel. Phen.* **28** (1982) 177.
- [As88] J.C. Ashley, *J. Electr. Spectr. Rel. Phen.* **46** (1988) 199.
- [As89] J.C. Ashley, *Oak Ridge National Laboratory Report CONF-8909210* (1989).
- [As90] J.C. Ashley, *J. Electr. Spectr. Rel. Phen.* **50** (1990) 323.
- [AT79] J.C. Ashley, C.J. Tung and R.H. Ritchie, *Surf. Science* **81** (1979) 409.
- [AW83] K.O. Al-Ahmad and D.E. Watt, *J. Phys. D: Appl. Phys.* **16** (1983) 2257.
- [BB67] J.A. Bearden and A.F. Burr, *Rev. Mod. Phys.* **39** (1967) 125.
- [BB86] R. Brun, F. Bruyant, M. Maire, A.C. McPherson and P. Zanarini, *CERN Report DD/EE/84-1* (Geneva, 1986).

- [Be53] H.A. Bethe, *Phys. Rev.* **89** (1953) 1256.
- [Be63] M.J. Berger, in: *Methods in Computational Physics*, vol. 1, eds. B. Alder, S. Fernbach and M. Rotenberg (Academic Press, New York, 1963) p. 135.
- [BH34] H.A. Bethe and W. Heitler, *Proc. R. Soc. London* **A146** (1934) 83.
- [Bh36] H.J. Bhabha, *Proc. R. Soc. London* **A154** (1936) 195.
- [Bi58] R.D. Birkhoff, in: *Handbuch der Physik*, vol. 34, ed. S. Flugge (Springer, Berlin, 1958) p. 53.
- [BJ83] B.H. Bransden and C.J. Joachain, *The Physics of Atoms and Molecules* (Longman, London, 1983).
- [BL50] O. Blunck and S. Leisegang, *Z. Physik* **128** (1950) 500.
- [Bo48] N. Bohr, *Kgl. Danske Vidensk. Selsk. Mat.-Fys. Medd.* **18**, n8 (1948).
- [Br83] B.H. Bransden, *Atomic Collision Theory* (2nd edition) (Benjamin Cummings, Reading, MA, 1983).
- [BR86] A.F. Bielajew and D.W.O. Rogers, *Nucl. Instrum. and Meth.* **B18** (1987) 165.
- [BS63] R.A. Bonham and T.G. Strand, *J. Chem. Phys.* **39** (1963) 2200.
- [BS84] M.J. Berger and S.M. Seltzer, National Bureau of Standards Report NBSIR 82-2550 (Washington, 1982). Also available as ICRU Report 37 (1984).
- [By56] W.J. Byatt, *Phys. Rev.* **104** (1956) 1298.
- [CC89] D.E. Cullen, M.H. Chen, J.H. Hubbell, S.T. Perkins, E.F. Plechaty, J.A. Rathkopf and J.H. Scofield, *Lawrence Livermore National Laboratory UCRL-50400* vol. 6, rev. 4, parts A and B (1989).
- [CH78] R.J. Celotta and R.H. Huebner, in: *Electron Spectroscopy*, vol. 3, eds. C.R. Brundle and A.D. Baker (Academic Press, London, 1978) p. 41.
- [CR83] International Commission on Radiation Units and Measurements Report ICRU 35 (Bethesda, 1984).
- [DB54] H. Davies, H.A. Bethe and L.C. Maximon, *Phys. Rev.* **93** (1954) 788.

- [DS56] J.A. Doggett and L.V. Spencer, *Phys. Rev.* **103** (1956) 1597.
- [DS89] Z.-J. Ding and R. Shimizu, *Surf. Science* **222** (1989) 313.
- [Fa56] U. Fano, *Phys. Rev.* **103** (1956) 1202.
- [Fa63] U. Fano, *Annual Review of Nuclear Science* **13** (1963) 1.
- [FB92] J.M. Fernández-Varea, J. Baró and F. Salvat, unpublished.
- [FC68] U. Fano and J.W. Cooper, *Rev. Mod. Phys.* **40** (1968) 441.
- [Fi74] H.-J. Fitting, *Phys. Status Solidi* **A26** (1974) 525.
- [FM91] J.M. Fernández-Varea, J.D. Martínez and F. Salvat, *J. Phys. D: Appl. Phys.* **24** (1991) 814.
- [FM92] J.M. Fernández-Varea, R. Mayol, F. Salvat and D. Liljequist, *J. Phys.: Condens. Matter* **4** (1992) 2879.
- [Fr77] Carlta Froese Fischer, *The Hartree-Fock Method for Atoms* (Wiley, New York, 1977).
- [GH69] F.W. Garber, J.A. Harter, R.D. Birkhoff and R.H. Ritchie, Oak Ridge National Laboratory Report ORNL-TM-2406 (February 1969).
- [GR80] I.S. Gradshteyn and I.M. Ryzhik, *Tables of Integrals, Series and Products* (Academic Press, New York, 1980).
- [GS40a] S. Goudsmit and J.L. Saunderson, *Phys. Rev.* **57** (1940) 24.
- [GS40b] S. Goudsmit and J.L. Saunderson, *Phys. Rev.* **58** (1940) 36.
- [GS69] A.E.S. Green, D.L. Sellin and A.S. Zachor, *Phys. Rev.* **184** (1969) 1.
- [He56] R.H. Helm, *Phys. Rev.* **104** (1956) 1466.
- [HG74] H.-J. Hagemann, W. Gudat and C. Kunz, *Deutsches Elektronen-Synchrotron Report SR-74/7* (Hamburg, 1974).
- [HG80] J.H. Hubbell, H.A. Gimm and I. Øverbø, *J. Phys. Chem. Ref. Data* **9** (1980) 1023.
- [Hi90] R. Hippler, *Phys. Lett.* **A144** (1990) 81.

- [HL51] A.O. Hanson, L.H. Lanzl, E.M. Lyman and M.B. Scott, *Phys. Rev.* **84** (1951) 634.
- [HL82] B.L. Henke, P. Lee, T.J. Tanaka, R.L. Shimabukuro and B.K. Fujikawa, *At. Data and Nucl. Data Tables* **27** (1982) 1.
- [HR56] B. Hahn, D.G. Ravenhall and R. Hofstadter, *Phys. Rev.* **101** (1956) 1131.
- [IL86] M. Ismail and D. Liljequist, University of Stockholm, Institute of Physics Report USIP 86-11 (1986).
- [In71] M. Inokuti, *Rev. Mod. Phys.* **43** (1971) 297.
- [IS81] S. Ichimura and R. Shimizu, *Surf. Science* **112** (1981) 386.
- [IS82] M. Inokuti and D.Y. Smith, *Phys. Rev.* **B25** (1982) 61.
- [Ja75] J.D. Jackson, *Classical Electrodynamics* (Wiley, New York, 1975).
- [JI83] P.E. Johnson and M. Inokuti, *Comm. At. and Mol. Phys.* **14** (1983) 19.
- [JT90] A. Jablonski and S. Tougaard, *J. Vac. Sci. Technol.* **A8**(1990) 106.
- [Ka70] H. Kanter, *Phys. Rev.* **B1** (1970) 2357.
- [KP86] L. Kim, R.H. Pratt, S.M. Seltzer and M.J. Berger, *Phys. Rev.* **A33** (1986) 3002.
- [KS59] F. Kalil, W.G. Stone, J.H. Hubbell, Jr. and R.D. Birkhoff, Oak Ridge National Laboratory Report ORNL-2731 (September 1959).
- [KW68] J. Kessler and N. Weichert, *Z. Phys.* **48** (1968) 212.
- [KW86] M.H. Kalos and P.A. Whitlock, *Monte Carlo Methods*, vol. 1 (Wiley, New York, 1986).
- [La44] L. Landau, *J. Phys. U.S.S.R.* **8** (1944) 201.
- [Le50] H.W. Lewis, *Phys. Rev.* **78** (1950) 526.
- [Li54] J. Lindhard, *Kgl. Danske Vidensk. Selsk. Mat.-Fys. Medd.* **28**, n.8 (1954) 1.
- [Li83] D. Liljequist, *J. Phys. D: Appl. Phys.* **16** (1983) 1567.

- [Li85] D. Liljequist, *J. Appl. Phys.* **57** (1985) 657.
- [LI90] D. Liljequist, M. Ismail, F. Salvat, R. Mayol and J.D. Martínez, *J. Appl. Phys.* **68** (1990) 3061.
- [LS53] J. Lindhard and M. Scharff, *Kgl. Danske Vidensk. Selsk. Mat.-Fys. Medd.* **27**, n.15 (1953) 1.
- [LS89] D. Liljequist, F. Salvat, R. Mayol and J.D. Martínez, *J. Appl. Phys.* **65** (1989) 2431, Erratum *J. Appl. Phys.* **66** (1989) 2768.
- [LW64] J. Lindhard and A. Winter, *Kgl. Danske Vidensk. Selsk. Mat.-Fys. Medd.* **34**, n.4 (1964) 1.
- [Ma71] S.T. Manson, *Phys. Rev.* **A3** (1971) 1260.
- [Ma83] G.D. Mahan, *Many-Particle Physics* (Plenum, New York, 1983).
- [Mc71] E.J. McGuire, *Phys. Rev.* **A3** (1971) 267.
- [MF91] R. Mayol, J.M. Fernández-Varea, F. Salvat and D. Liljequist, *Interaction of Charged Particles with Solids and Surfaces*, NATO ASI Series vol. B-271, eds. A. Gras-Martí et al. (Plenum, New York, 1991) p. 585.
- [MM65] N.F. Mott and Q.S.W. Massey, *The Theory of Atomic Collisions* (Oxford University Press, London, 1965).
- [MM90] J.D. Martínez, R. Mayol and F. Salvat, *J. Appl. Phys.* **67** (1990) 2955.
- [Mo32] C. Møller, *Ann. Physik* **14** (1932) 531.
- [Mo47] G. Molière, *Z. Naturf.* **2a** (1947) 133.
- [Mo48] G. Molière, *Z. Naturf.* **3a** (1948) 78.
- [MO64] J.W. Motz, H. Olsen and H.W. Koch, *Rev. Mod. Phys.* **36** (1964) 881.
- [MS90] R. Mayol and F. Salvat, *J. Phys. B: At. Mol. Opt. Phys.* **23** (1990) 2117.
- [NH85] W.R. Nelson, H. Hirayama and D.W.O. Rogers, Stanford Linear Accelerator Center Report SLAC-265 (Stanford, 1985).
- [NS59] B.P. Nigam, M.K. Sundaesan and T.-Y. Wu, *Phys. Rev.* **115** (1959) 491.

- [Oc64] V.I. Ochkur, *Sov. Phys. JETP* **18** (1964) 503.
- [Pa50] G. Parzen, *Phys. Rev.* **80** (1950) 261.
- [Pa85] *Handbook of Optical Constants of Solids*, ed. E.D. Palik (Academic Press, New York, 1985).
- [Pe87] D.R. Penn, *Phys. Rev.* **B35** (1987) 482.
- [PN89] D. Pines and P. Nozières, *The Theory of Quantum Liquids: Normal Fermi Liquids* (Addison-Wesley, Redwood City, CA, 1989).
- [Po74] C.J. Powell, *Surf. Science* **44** (1974) 29.
- [RC54] F. Rohrlich and B.C. Carlson, *Phys. Rev.* **93** (1954) 38.
- [RH77] R.H. Ritchie and A. Howie, *Phil. Mag.* **36** (1977) 463.
- [Ri57] R.H. Ritchie, *Phys. Rev.* **106** (1957) 874.
- [RK76] L. Reimer and E.R. Krefling, *National Bureau of Standards Special Publication 460* (US Government Printing Office, Washington DC, 1976) p. 45.
- [RL84] L. Reimer and B. Lödding, *Scanning* **6** (1984) 128.
- [RM75] M.E. Riley, C.J. MacCallum and F. Biggs, *At. Data Nucl. Data Tables* **15** (1975) 444.
- [Ru81] R.Y. Rubinstein, *Simulation and the Monte Carlo Method* (Wiley, New York, 1981).
- [Sa91] F. Salvat, *Phys. Rev.* **A43** (1991) 578.
- [SB82] R.M. Sternheimer, M.J. Berger and S.M. Seltzer, *Phys. Rev.* **B26** (1982) 6067, and *At. Data and Nucl. Data Tables* **30** (1984) 261.
- [SB82] S.M. Seltzer and M.J. Berger, National Bureau of Standards Report No. NBSIR 82-2572 (1982) (unpublished).
- [SB85] S.M. Seltzer and M.J. Berger, *Nucl. Instr. and Meth.* **B12** (1985) 95.
- [Sc51] L.I. Schiff, *Phys. Rev.* **83** (1951) 252.
- [Sc63] W.T. Scott, *Rev. Mod. Phys.* **35** (1963) 231.

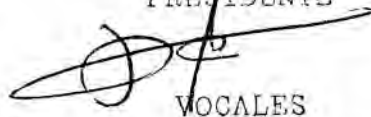
- [Sc68] L.I. Schiff, *Quantum Mechanics* (McGraw-Hill, Tokyo, 1968).
- [SD86] A. Scheidemann and R.M. Dreizler, *Z. Phys.* **D2** (1986) 43.
- [SF92] F. Salvat and J.M. Fernández-Varea, *Nucl. Instr. and Meth.* **B63** (1992) 255.
- [Sh56] N. Sherman, *Phys. Rev.* **103** (1956) 1601.
- [SL81] J. Szajman and R.C.G. Leckey, *J. Electr. Spectr. Rel. Phen.* **23** (1981) 83.
- [SM85a] F. Salvat, J.D. Martínez, R. Mayol and J. Parellada, *J. Phys D: Appl. Phys.* **18** (1985) 299.
- [SM85b] F. Salvat, R. Mayol, E. Molins and J. Parellada, *J. Phys. D: Appl. Phys.* **18** (1985) 1401.
- [SM86] F. Salvat F., J.D. Martínez, R. Mayol and J. Parellada, *Comput. Phys. Commun.* **42** (1986) 93.
- [SM87a] F. Salvat, J.D. Martínez, R. Mayol and J. Parellada, *Phys. Rev.* **A36** (1987) 467.
- [SM87b] F. Salvat, R. Mayol and J.D. Martínez, *J. Phys. B: At. Mol. Phys.* **20** (1987) 6597.
- [SM91] F. Salvat and R. Mayol, *Comput. Phys. Commun.* **62** (1991) 65.
- [SP71] R.M. Sternheimer and R.F. Peierls, *Phys. Rev.* **B3** (1971) 3681.
- [SS80] E. Shiles, T. Sasaki, M. Inokuti and D.Y. Smith, *Phys. Rev.* **B22** (1980) 1612.
- [SS85] D.Y. Smith, E. Shiles and M. Inokuti, in ref. [Pa85] p. 369.
- [St52] R.M. Sternheimer, *Phys. Rev.* **88** (1952) 851.
- [TA79] C.J. Tung, J.C. Ashley and R.H. Ritchie, *Surf. Science* **81** (1979) 427.
- [TP87] S. Tanuma, C.J. Powell and D.R. Penn, *Surf. Science* **192** (1987) L869.
- [TP88] S. Tanuma, C.J. Powell and D.R. Penn, *Surf. Interface Anal.* **11** (1988) 577.
- [TP91a] S. Tanuma, C.J. Powell and D.R. Penn, *Surf. Interface Anal.* **17** (1991) 911.
- [TP91b] S. Tanuma, C.J. Powell and D.R. Penn, *Surf. Interface Anal.* **17** (1991) 927.

- [Tr74] J.C. Tracy, *J. Vacuum Sci. Technol.* **11** (1974) 280.
- [Ts74] Y.S. Tsai, *Rev. Mod. Phys.* **46** (1974) 815.
- [Va57] P.V. Vavilov, *Soviet Physics JETP* **5** (1957) 749.
- [VP74] D.W. Vande Putte, *Nucl. Instr. and Meth.* **115** (1974) 117.
- [Wa71] D.W. Walker, *Adv. Phys.* **20** (1971) 257.
- [We27] G. Wentzel, *Z. Phys.* **40** (1927) 590.
- [Yo56] J.R. Young, *Phys. Rev.* **103** (1956) 292.
- [YR54] D.R. Yennie, D.G. Ravenhall and R.N. Wilson, *Phys. Rev.* **95** (1954) 500.
- [ZO64] E. Zeitler and H. Olsen, *Phys. Rev.* **136** (1964) A1546.
- [ZO67] E. Zeitler and H. Olsen, *Phys. Rev.* **162** (1967) 1439.

UNIVERSIDAD DE BARCELONA

Leida esta Memoria el dia 21 de
Julio de 1982 en la Facultad de
 Fisica, ante el siguiente Tribunal:

PRESIDENTE



VOCALES





fué calificada de APTO CON LAUDE!